

AD-R164 838

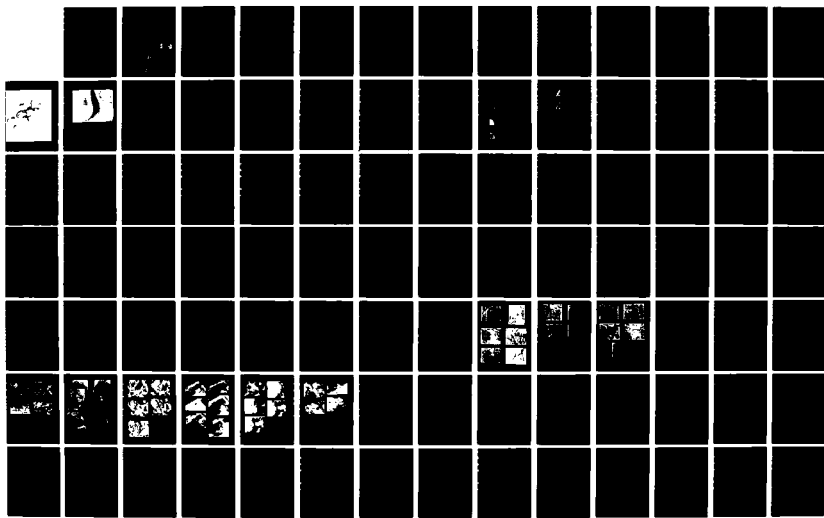
COMPOSITE STRENGTHENING(U) MARYLAND UNIV COLLEGE PARK  
ENGINEERING MATERIALS GROUP R J ARSENAULT 1985  
N88014-85-K-8887

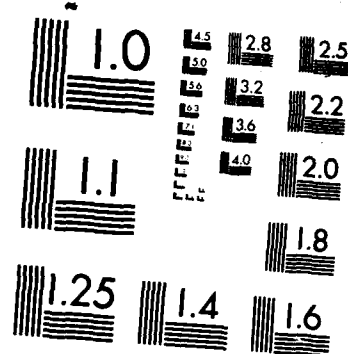
1/2

UNCLASSIFIED

F/G 11/4

NL





MICROCOPY RESOLUTION TEST CHART  
NATIONAL BUREAU OF STANDARDS-1963-A

AD-A164 838

## ANNUAL REPORT

1985

## COMPOSITE STRENGTHENING

OFFICE OF NAVAL RESEARCH  
CONTRACT NO. N00014-85-K-0007

BY

R.J. ARSENAULT  
PROFESSOR AND DIRECTOR  
ENGINEERING MATERIALS GROUP

DTIC  
SELECTED  
MAR 04 1985  
S D

UNIVERSITY OF MARYLAND  
COLLEGE PARK, MD 20742

DISTRIBUTION STATEMENT A  
Approved for public release  
Distribution Unlimited

6 108

ANNUAL REPORT

1985

COMPOSITE STRENGTHENING

OFFICE OF NAVAL RESEARCH  
CONTRACT NO. N00014-85-K-0007

BY

R.J. ARSENAULT  
PROFESSOR AND DIRECTOR  
ENGINEERING MATERIALS GROUP

UNIVERSITY OF MARYLAND  
COLLEGE PARK, MD 20742

## SUMMARY

It has been demonstrated that a strong interfacial bond is required to produce the observed strengthening in discontinuous SiC/Al composites.

Dislocation generation (which is the strengthening mechanism) is dependent upon a good bond existing between the SiC and the Al matrix.

Although it has been shown that the stresses developed in the matrix as a result of the differences in the coefficients of thermal expansion between SiC and Al are greatly reduced by the motion and generation of dislocations, an elastic residual stress can still remain.

An investigation was undertaken and it was determined that in the discontinuous SiC/Al composites a tensile-elastic-residual stress remains in the matrix. This determination is based on results from a theoretical model, tensile and compression testing and X-ray measurements. The results from all the tests and the model are in agreement. The magnitude of the residual stress is small, e.g., with 20 V% whisker aluminum in an annealed 6061 Al alloy matrix, the residual stress is 70 MPa. If the matrix is annealed 1100 Al, then residual stress is still smaller; 43 MPa.

The tensile residual stress produces a Bauschinger Effect (BE) which is highly dependent upon the initial direction of loading. If the initial direction of loading is in tension, the BE is small, if the initial direction of loading is in compression, the BE is very large.

It has been observed that as the strength of the matrix increases, e.g., due to alloying or age hardening, the percentage increase in yield

→ or ultimate tensile strength decreases for a given volume per cent SiC/Al composite. If the matrix is 1100 Al and 20 V% SiC whisker is added, then there is a 420% increase in strength, whereas, if the matrix is annealed 6061 Al alloy, there is a ~ 181% increase in strength. For annealed 7091 matrix the increase is ~ 190%. If the absolute magnitude is considered, the increase is greatest for 1100 Al matrix and decreases with increasing alloy content. The basic reason for this difference in strengthening is due to the change in the magnitude of the dislocation density and of the tensile residual stress. In the case of the 1100 matrix, there is maximum dislocation generation due to differences in coefficients of thermal expansion and a minimum tensile residual stress, because the yield stress of annealed 1100 matrix is less than the yield stress of the annealed 6061 and 7091 matrix.

In the first section is a list of presentations, and the second section includes a list of papers in preparation. The third section is a compilation of the publications which have been produced under this contract.

Accession For	
NTIS CRA&I	<input checked="" type="checkbox"/>
DTIC TAB	<input type="checkbox"/>
Unannounced	<input type="checkbox"/>
Justification	
By <i>Mr. on file</i>	
Distribution /	
Availability Codes	
Dist	Avail a: d / or Special
A-1	



**I PRESENTATIONS:**

1. Seventh Annual Meeting of Metal Matrix Composites 1985  
Strengthening Mechanisms
2. Fifth International Conference on Composite Materials 1985  
Thermal Residual Stresses in Short Fiber Composites.
3. Fall Meeting of AIME 1984  
Anomalous Diffusion at Interfaces in Metal Matrix Composites  
R.J. Arsenault and C.S. Pande
4. Fall Meeting of AIME 1984  
Fracture of SiC/Al Composites
5. Annual Meeting of AIME 1985  
Deformation in SiC/Al Composites Due to Thermal Stresses  
Y. Flom and R.J. Arsenault
6. Annual Meeting of AIME 1985  
Dislocation Distributions in Deformed SiC/Al Composites  
M. Lammers and R.J. Arsenault

**II PAPERS IN PREPARATION:**

1. STRENGTH DIFFERENTIAL AND BAUSCHINGER EFFECT IN  
SiC/Al COMPOSITES  
R.J. Arsenault and B. Wu
2. DISLOCATION GENERATION DUE TO DIFFERENCES IN  
COEFFICIENTS OF THERMAL EXPANSION  
R.J. Arsenault and N. Shi
3. ROLE OF INTERFACES IN METAL-MATRIX COMPOSITES  
R.J. Arsenault and Y. Flom
4. CRYSTAL STRUCTURE OF SiC WHISKERS  
R.J. Arsenault and J. Ahearn  
Submitted for publication.

### III PUBLICATIONS:

1. INTERFACES IN METAL MATRIX COMPOSITES  
R.J. Arsenault and C.S. Pande  
Scripta Met., 18, 1984, 1131.
2. DEFORMATION IN SiC/Al COMPOSITES DUE TO THERMAL STRESS  
Y. Flom and R.J. Arsenault  
Mat. Sci. and Eng., 75, 1985, 151.
3. THE EFFECTS OF DIFFERENCES IN THERMAL COEFFICIENTS OF EXPANSION IN SiC WHISKER 6061 Al COMPOSITES  
Proceedings of the Fifth Internal Conference on Composite Materials, ed. by W.C. Harrigan, Jr., et al., 1985, 21.
4. INTERFACIAL BOND STRENGTH IN A 6061 Al/SiC COMPOSITE  
Y. Flom and R.J. Arsenault  
Mat. Sci. Eng., 77, 1986, 191.
5. AN IN SITU HOT STAGE TEM INVESTIGATION OF SiC-Al COMPOSITES  
M. Vogelsang, R.J. Arsenault and R.M. Fisher  
Accepted for publication in Met. Trans. (to appear in the March 1986 issue.)
6. RESIDUAL STRESSES IN FIBER METAL MATRIX COMPOSITES  
R.J. Arsenault and M. Taya  
Submitted for publication.

These publications follow and each publication is separated by a green insert.

## Interfaces in Metal Matrix Composites\*

R. J. Arsenault  
Engineering Materials Group  
University of Maryland  
College Park, MD 20742

C. S. Pande  
Naval Research Laboratory  
Washington, D.C. 20375

### Introduction

A basic premise in most theories of composite strengthening is that a bond of some type exists between the matrix and the reinforcement. This bond is involved in the mechanism of load transfer between the matrix and the reinforcement. Therefore, in terms of tensile strength a good or sufficient bond is required to obtain the maximum strength from the composite. In the model metal-matrix composite, i.e., the Cu-W composite, the bond strength between W and Cu is very good<sup>(1)</sup>. In the case of SiC-Al composites there have been no direct measurements of the bond strength, but indirect data indicates that the bond strength is quite good<sup>(2,3)</sup>.

It is presumed that the bond strength is related to the nature of the interface between the matrix and the reinforcement. There have been three mechanisms or hypothesis put forward concerning the interface between the SiC and the Al matrix. The first is that there is a  $\text{SiO}_2$  film or layer between the SiC and

\* Research supported in part by the Office of Naval Research  
Under Contract No. N00014-82-K-0493.

the Al matrix, this is an idea put forward by Parratt<sup>(4)</sup>. The second hypothesis is that there is nothing at the interface. This hypothesis is based on the work that has been done on the model metal-matrix composite, i.e., the Cu-W composite<sup>(5)</sup>. In that particular system no interphases were found between the Cu and W. The third hypothesis is that there is a  $\text{Al}_4\text{C}_3$  film between the SiC and the Al matrix, this concept was put forward on a thermodynamics basis. If molten Al exists with a small amount of dissolved Si, then it thermodynamically possible for  $\text{Al}_4\text{C}_3$  to form<sup>(6)</sup>.

The purpose of this investigation was to determine in greater detail the nature of the interface between SiC and Al and W and Cu.

### Results

A scanning Auger microprobe analysis\* was undertaken of fractured SiC-Al samples, in particular fractured whisker samples produced by ARCO SILAG. These samples were fractured in the scanning Auger microprobe and examined shortly thereafter. When the fracture surfaces were examined there were no differences, in signal as a function of position, in other words, a 100% Al signal was obtained from the matrix as well as from all possible areas on the SiC whiskers as shown in Fig. 1. A possible

\* The Auger microprobe analysis were performed at the Center for Research in Surface Science and Submicron Analysis, Montana State University.

explanation of the essentially 100% Al content on the whisker is that the Al could just be mechanically adhering, very similar to the butter knife analogy. (If you stick a butter knife into butter and pull it out you have a coating of butter on the butter knife.) Therefore, a series of etching experiments were conducted in the microprobe and it was only after considerable sputtering, (which is basically an Ar ion milling operation) that the Si and C signals were obtained. The sputter etching was interrupted at intervals and the surfaces of the whiskers examined, there were no indications of  $\text{SiO}_2$ ,  $\text{Al}_2\text{O}_3$ ,  $\text{Al}_4\text{O}_3$ . This result led us to the belief that the Al had diffused into the SiC. In order to determine, whether this is a real effect, and not a sputtering artifact, several samples, which were metallographically polished, were examined in the Auger microprobe. The data from a platelet of SiC sample from DWA, are shown in Fig. 2. In the SEM micrograph the scanning Auger probe traces are superimposed. One trace is for Al and other trace is for Si. This shows that Al has penetrated or diffused into the SiC, but there is no Si or C in the matrix. Then this sample was sputter etched and the process repeated and basically the same result was obtained. In order to determine what the effect of sputtering, (i.e., could the sample surface become cross contaminated by the sputtering operation) the sample was removed, etched slightly with Keller's etch, and then put back into the microprobe and then the process was repeated and again the same results were obtained. Figure 3 is the detailed Auger probe analysis of the Si and Al traces, the C trace superimposes right on the Si

trace. The interface is then defined as having finite width and that is the maximum probe size that is associated with the scanning microprobe apparatus.

In order to further validate these results, a STEM analysis was conducted of SiC samples, and Fig. 4 is a result of an energy dispersive X-ray analysis from the STEM using a thin foil of the composite. It is obvious that again there is evidence of Al diffusion into the SiC. In this particular case the probe size is much smaller ( $\sim 50 \text{ \AA}$ ) than that in the scanning Auger analysis. The thickness of the specimen was 1000 - 1500  $\text{\AA}$ ; (accelerating voltage, of the electrons 200 KV) thus the spatial resolution of the technique was about 300  $\text{\AA}$ , several times smaller than the range of penetration observed. In order to determine whether this may be a universal affect, an analysis was begun of Cu-W. Figure 5 is a typical scanning Auger microprobe result of Cu and W. The data indicates that Cu has diffused into the W, and there is a very sharp edge of the W filament and the matrix. It should be kept in mind that the experimental results of the bond strength between Cu and W is extremely good. STEM analysis of Cu-W interfaces are in progress.

#### Discussion of Conclusion

The observations of Al penetration into SiC and the Cu penetration into W to the extent observed is unexpected. There have been at least two investigations of Al diffusion into SiC<sup>(7,8)</sup>, and from those investigations it is possible to

calculate the mean diffusion distance  $X$  at 773 K,

$$X = \sqrt{Dt} \quad (1)$$

where  $D = D_0 e^{-Q/RT}$ ,  $t$  is the time of diffusion,  $Q$  for Al-SiC system is 471 kJ/mole and  $D_0$  equals  $1.8 \text{ cm}^2/\text{sec}$ . The value of  $X$  is less than one Å per year. (The values of  $D_0$  and  $Q$  given in literature vary substantially from each other. However all of these values give a value of  $X$  orders of magnitude lower than the observed penetration.) Needless to state this does not agree with the present data. In the case of Cu diffusion into W there have been no known reported investigations. In fact there is no phase diagram of Cu-W<sup>(9)</sup>, but there is SiC-Al<sub>3</sub>C<sub>4</sub> phase diagram<sup>(10)</sup> at 2133 K and it shows solubility of Al<sub>3</sub>C<sub>4</sub> in SiC. The fact that there is solubility of Al<sub>3</sub>C<sub>4</sub> in SiC does not explain how the Al could diffuse that far. However, from the second law of thermodynamics the presence of Al in SiC and Cu in W can be explained, as due a reduction in free energy due to the entropy of mixing. In fact there is some data (at 2073 K) of the solubility of Al<sup>(11)</sup> in SiC. The depth of penetration, i.e., diffusion, cannot be explained in terms of classical bulk diffusion, there must be a short circuit path. In the case of Cu-W, there may be substantial grain boundary diffusion, due to the small grain size in the W filaments.

In terms of bonding between the reinforcement and the matrix, in both cases the bonding appears to be very good, and there is penetration of the matrix into the reinforcement. It

may be concluded that the diffusion bonding results in a high strength bond.

#### Acknowledgements

The authors wish to acknowledge M. Losh of the University of Maryland for assistance with the experiments. Effective liaison with Dr. Bruce McDonald of the Office of Naval Research, Arlington, VA has been very helpful to the project.

#### References

1. A. Kelly, W. R. Tyson, J. Mech. Phys. Solids 13, 329 (1965).
2. R. J. Arsenault, to be published in Met. Sci. and Eng.
3. R. J. Arsenault and R. M. Fisher, Scripta Met. 17, 67 (1983).
4. N. Parratt, private communication.
5. W. R. Tyson, private communication.
6. T. Iseki, T. Kameda and T. Maruyama, J. Mater. Sci. 19, 1692 (1984).
7. H. C. Chang, C. Z. LeMay and L. F. Wallace, Silicon Carbide, Ed. by J. R. O'Connor and J. Smitons, Pergamon Press, Oxford, 1960 ,p. 496.
8. Y. Tajima, K. Kijima and W. D. Kinery, J. Chem. Phys. 77, 2592 (1982).
9. Constitution of Binary Alloys, P. Hanson, McGraw-Hill, 1958, Constitution of Binary Alloys, R. Elliott, McGraw-Hill, 1965.
10. G. Schneider, L. J. Gauckler, G. Petzow and A. Zanguil, J. American Cer. Soc. 62, 574 (1962).
11. Y. Tajima and W. D. Kingery, Com. of the Am. Cer. Soc. C-27 (1982).

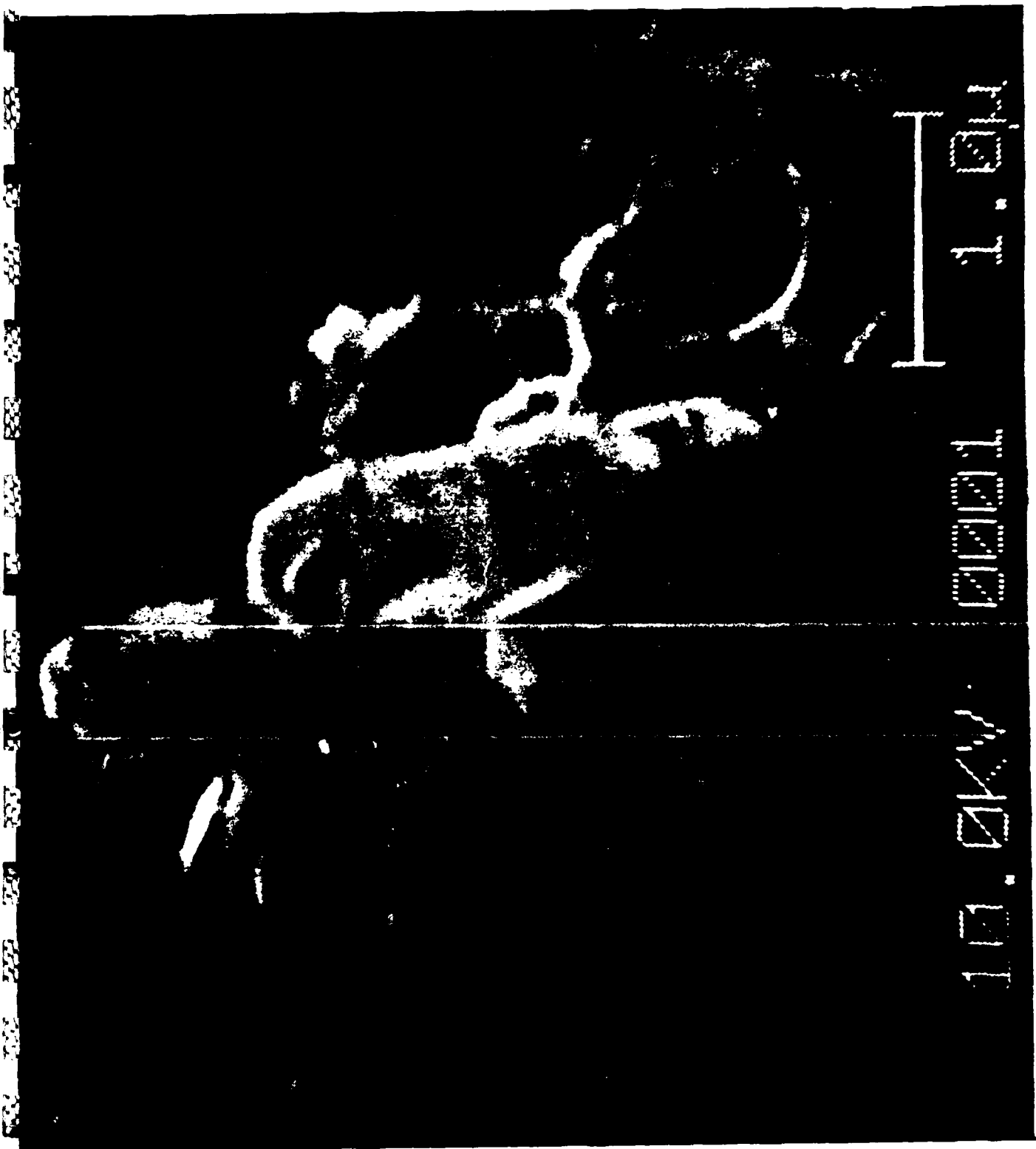


Fig. 1. A SEM micrograph taken in the Auger microprobe of the fracture surface of a whisker SIC-Al composite.

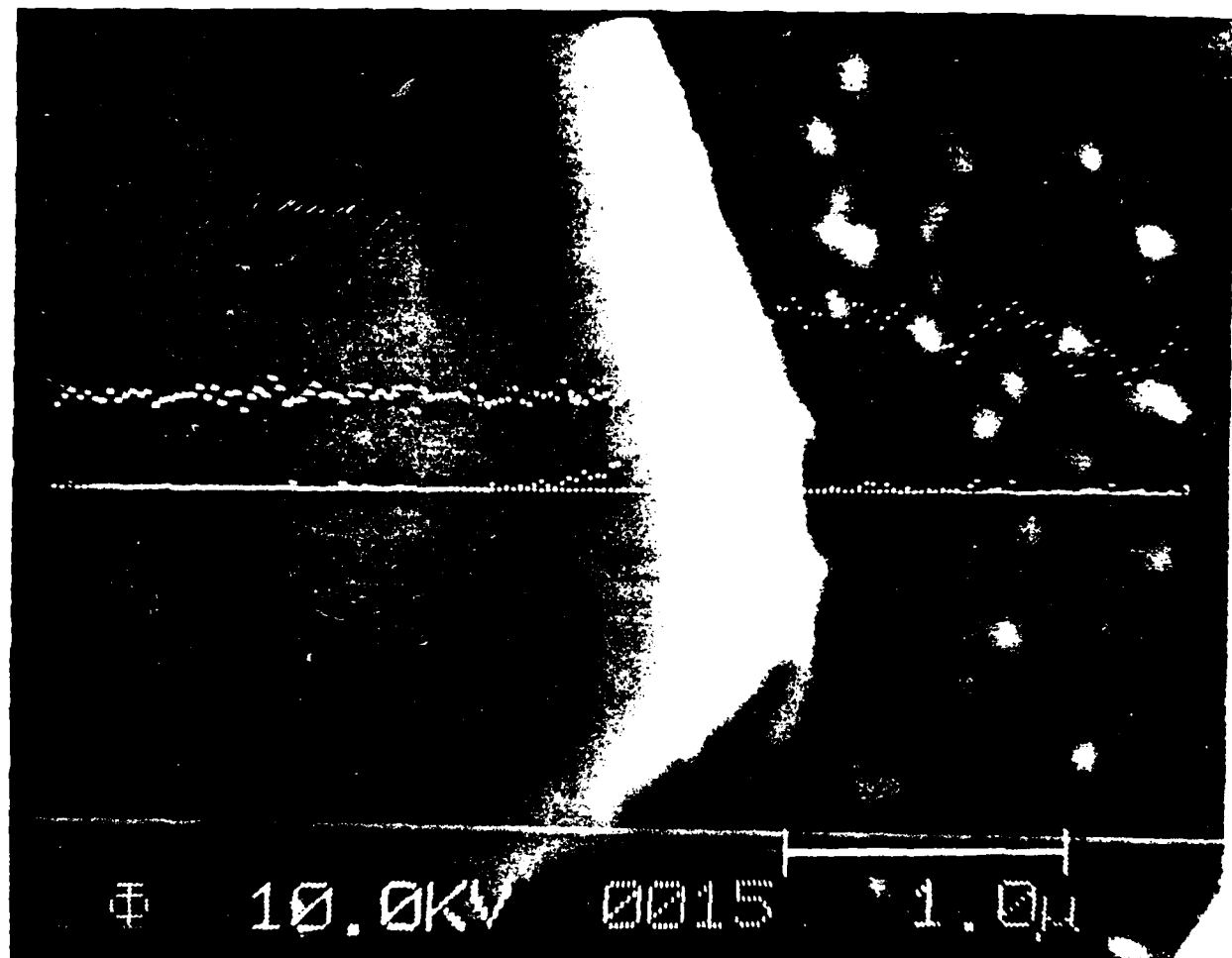


Fig. 2. A SEM micrograph taken in the Auger microprobe, on which the Al and Si Auger probe traces have been superimposed.

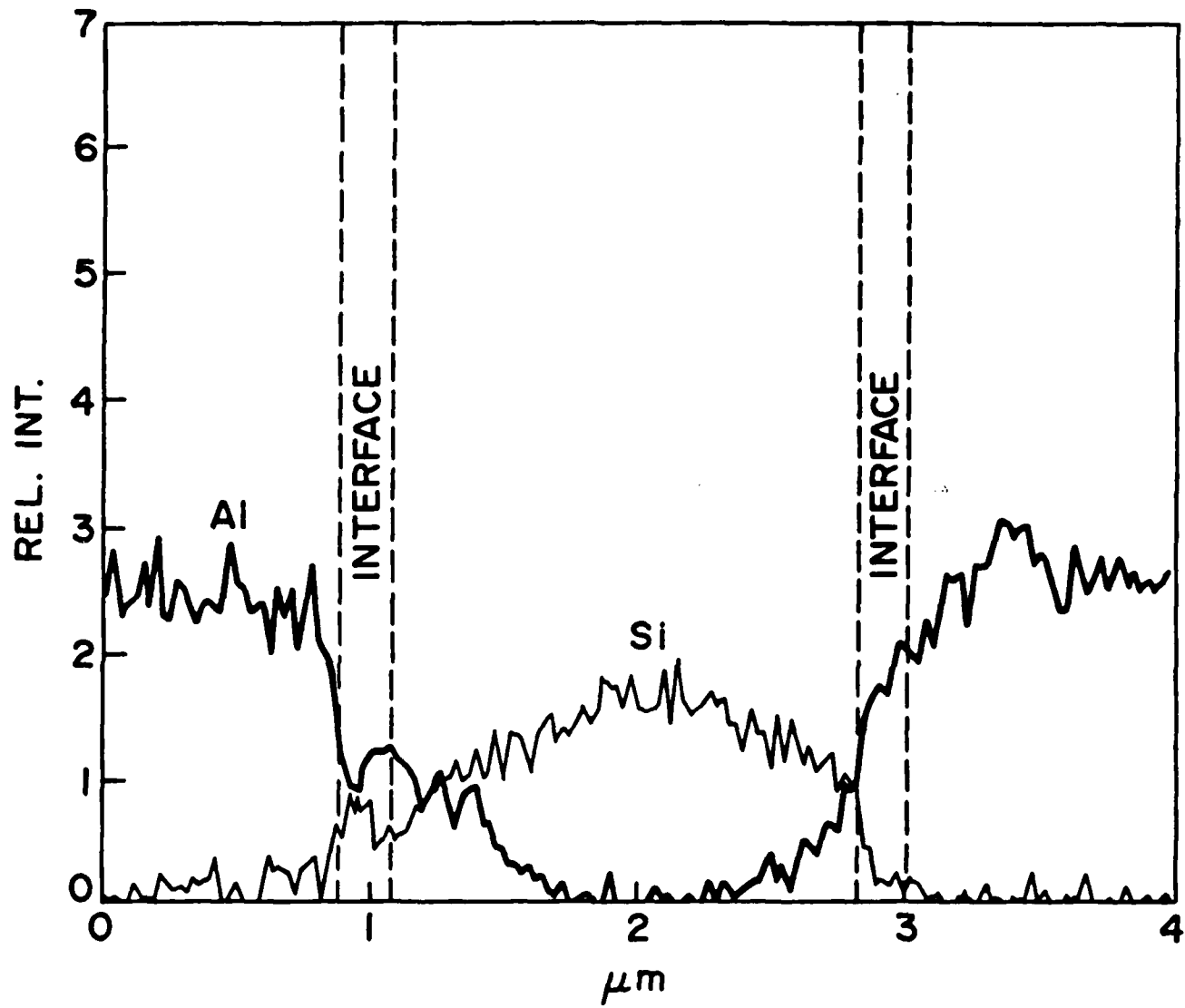


Fig. 3. An Auger microprobe analysis of SiC-Al. The relative intensities of Si and Al are plotted across the matrix, a particle of SiC and again the matrix.

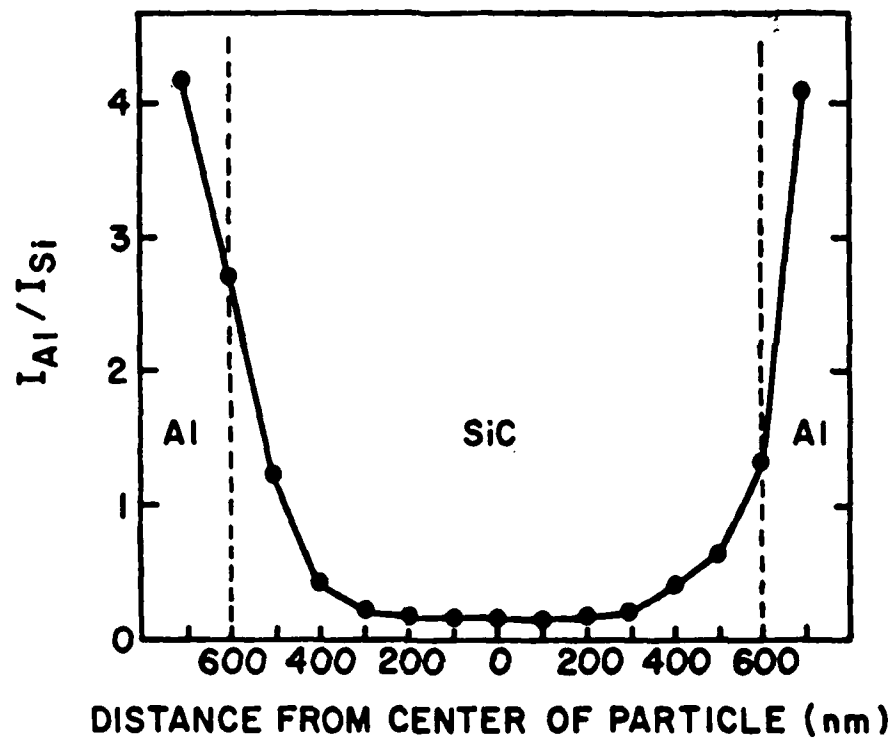


Fig. 4. A STEM EDXA analysis of Al concentration as a function of location ( $I_{Al}/I_{Si}$  plotted in arbitrary units).

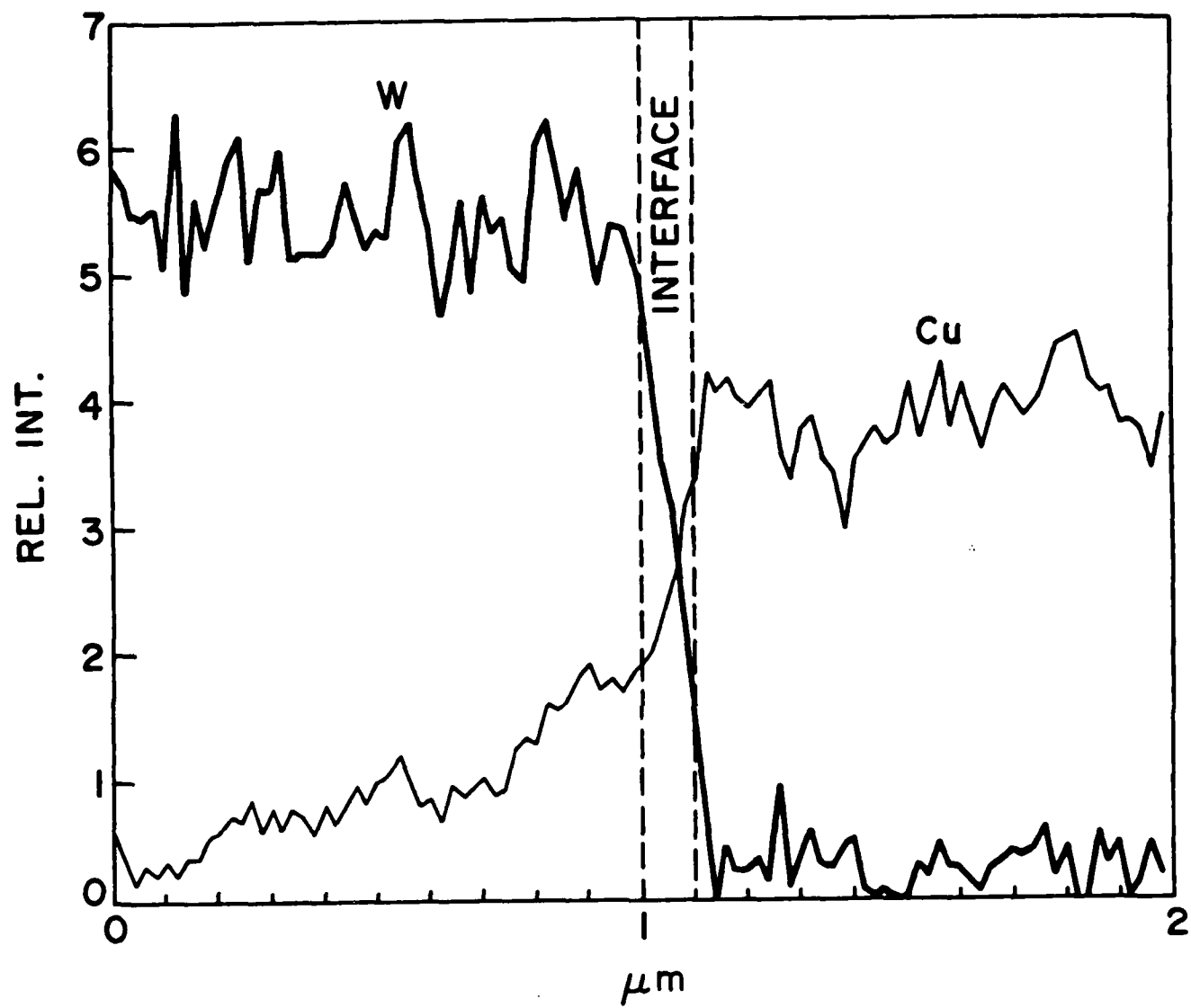


Fig. 5. An Auger microprobe analysis of W-Cu. The relative intensities of W and Cu are plotted as a function of location.

## Deformation in Al-SiC Composites Due to Thermal Stresses

Y. FLOM and R. J. ARSENAULT

Metallurgical Materials Laboratory, University of Maryland, College Park, MD 20742 (U.S.A.)

(Received January 2, 1985; in revised form March 13, 1985)

### ABSTRACT

*Plastic strains and the extent of the plastic zone due to differential thermal expansion were experimentally determined in an Al-SiC composite. The combined plastic shear strains  $\gamma_{cpss}$  at the Al-SiC interface for furnace-cooled, air-cooled and quenched samples were found to be 1.32%, 1.23% and 0.99% respectively. Profiles of  $\gamma_{cpss}$  were plotted versus distance from the interface and compared with the theoretical distribution of effective strain  $\bar{\epsilon}$ . The theoretical extent of the plastic zone measured from the interface was found to be 1.3 multiplied by the particle radius. This value was slightly less than the observed value. The plastic deformation on the heating half of the thermocycle was found to be at least equal to the deformation on the cooling half. A theoretical treatment of the local plastic deformation in a short composite cylinder was suggested, from which the effective plastic strain  $\bar{\epsilon}$  and the extent of the plastic zone were determined.*

### 1. INTRODUCTION

When a composite material is subjected to a temperature change, local plastic deformation can occur. The plastic deformation is due to a stress created by the difference between the coefficients of thermal expansion of the component phases, and this stress is at the matrix-reinforcement interfaces. The magnitude of the stress is equal to  $\Delta\alpha \Delta T$  where  $\Delta\alpha$  is the difference between the coefficients of thermal expansion of the phases under consideration and  $\Delta T$  is the temperature change. The relatively large (10 to 1) difference between the coefficient of thermal expansion of SiC and that of aluminum should result in the creation of a substantial misfit strain at the Al-SiC interface during cooling from the fabricating or

annealing temperature. The mechanical properties of the composite should be affected by the magnitude and extent of the plastic deformation that takes place in the soft matrix around a hard particle as a result of the misfit relaxation in the interface region. Recent investigations [1-4] have indeed shown the important role of the interfacial regions in the composite strengthening. Thus, knowledge of the magnitude of plastic strains and the size of the plastic zone as well as other characteristics of the interfacial region (the bond strength, the microstructure etc.) should contribute to the understanding of the mechanism of composite strengthening.

The experimental determinations of plastic strains and plastic zone radii about a particle in the matrix due to the difference between the coefficients of thermal expansion of the phases, to our knowledge, have not been reported in the literature.

Several theoretical investigations have been undertaken to predict the magnitude of the plastic strain in the plastic zone around a particle. The relaxation of the misfit caused by the introduction of an oversized spherical particle into a spherical hole in the matrix has been analytically described by Lee *et al.* [5]. Using the misfitting sphere model, they calculated strains in the plastic zone that surrounds a hard sphere and also the plastic zone radius. Hoffman [6] calculated the overall total strains in the tungsten-fiber-reinforced 80Ni-20Cr matrix, using a thick-wall long-cylinder approach and assuming that a hydrostatic stress state exists within each constituent.

Garmong [7], assuming uniformity of the stresses and strains in the matrix, calculated deformation parameters for a hypothetical eutectic composite and reported values of matrix plastic strains that were of the order of 0.4%.

Dvorak *et al.* [8] developed a new axi-symmetric plasticity theory of fiberous composites involving large thermal changes. The long-composite-cylinder model was adopted as a composite unit cell, and the microstress distribution as well as the yielding surfaces were obtained for Al-W composites.

Mehan [9] calculated the residual strains in an Al- $\alpha$ -Al<sub>2</sub>O<sub>3</sub> composite due to cooling from the fabricating temperature. He considered an idealized composite consisting of a long sapphire cylinder surrounded by an aluminum matrix. This is equivalent to the long-composite-cylinder model used by Dvorak *et al.* This model implies that the thermal strain along the cylinder axis is a constant, *i.e.* that

$$\epsilon_z = \frac{dl}{l} = \text{constant}$$

where  $l$  is the length of the cylinder. This simplifies the procedure of obtaining the radial  $\epsilon_r$  and the tangential  $\epsilon_\theta$  strains which was done using incompressibility and boundary conditions. The effective strain  $\bar{\epsilon}$  at the Al- $\alpha$ -Al<sub>2</sub>O<sub>3</sub> interface was found to be 1.6%.

However, the above-mentioned composite models do not give an accurate description of the plastic strain state in the short-composite-cylinder model. A short-cylinder model nearly duplicates the situation in the whisker and platelet Al-SiC composites at present produced.

The purpose of this work was to determine experimentally the magnitude of the local plastic strain produced in the aluminum matrix around a short SiC cylinder during a thermocycle and also to estimate the extent of the plastic zone around the cylinder. Also an effort was made to develop a theoretical

model of the plastic zone around the short cylinder.

## 2. EXPERIMENTAL PROCEDURE

The small particle interspacing (several micrometers) in a commercially available Al-SiC composite makes it impossible to measure the local plastic strain at the Al-SiC interface directly. Thus a composite model consisting of an SiC cylinder embedded in an aluminum matrix was fabricated so that direct strain measurements could be attempted.

Aluminum of 99.99% purity (to eliminate the influence of the alloying elements) and commercial carborundum were used to produce the composite model. Selected properties of these materials are given in Table 1.

Platelets of SiC were separated from carborundum conglomerates that are used in the production of abrasives. These platelets were spark planed on an electric discharge machine to plates approximately 1 mm thick. These flat plates were cut into rectangular rods approximately 1 mm  $\times$  1 mm. After this, each rod was spark machined to cylinders of about 1 mm diameter.

Pure aluminum rods, 12.5 mm in diameter in the as-received condition, were cut into studs 37 mm long. Two aluminum studs and one SiC rod were assembled together and put in a specially built compaction die, where they were hot pressed to produce one compact. Compaction was done on the Instron testing machine. During the entire compaction cycle (Table 2), a vacuum of about  $10^{-3}$  Torr was maintained using a mechanical vacuum pump.

TABLE 1  
Selected properties of the aluminum and SiC used in this paper

Material	Yield strength (MPa)	Elastic modulus (MPa)	Bulk modulus (MPa)	Poisson's ratio	Thermal expansion coefficient ( $\text{m m}^{-1} \text{K}^{-1}$ ) in the temperature range 293-773 K	Melting point (K)	Reference
Al	11.73	$62 \times 10^3$	$57.5 \times 10^3$	0.31	$28 \times 10^{-6}$	933	[10, 11]
SiC	34.5 (tension) 1380 (compression)	$483 \times 10^3$	$96.6 \times 10^3$	0.19	$3 \times 10^{-6}$	3373	[12, 13]

TABLE 2

Flow chart of the compaction of an Al-SiC composite cylinder

<i>Heating</i>	
Heating time	≈ 1 h
Temperature	≈ 843 K
<i>Compression</i>	
Cross-head speed	0.1 cm min <sup>-1</sup>
Total travel	10 mm
<i>Holding at constant load</i>	
Time	2 h
Pressure	2.28 MPa
<i>Incremental cooling under pressure</i>	
Time	12 h
Pressure	2.28 MPa

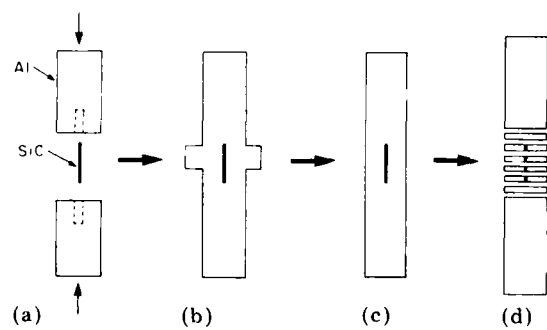


Fig. 1. A schematic diagram of the fabrication sequence of the Al-SiC composite model.

The central portion of the compacted sample was sliced in the transverse direction into disks 1 mm thick using the electric discharge machine, set at a low power, and each disk contained an SiC cylinder very close to the perfect center (Fig. 1). All Al-SiC disks were metallographically and then electrolytically polished to remove the thin cold-worked surface layer of aluminum.

The method adopted for the evaluation of plastic deformation was based on the direct observation of slip bands on the polished surface of the sample around the SiC particles. The amount of slip is a characteristic of the amount of plastic deformation (when deformation occurs by slip) in a crystalline solid. The plastic strain can be evaluated if the number of slip bands and the displacement on each band are known. The concept of combined plastic shear strain  $\gamma_{cpss}$  has been intro-

duced where  $\gamma_{cpss}$  is equivalent to the product of slip band density  $N$  and the amount of slip  $S$ , i.e.

$$\gamma_{cpss} = KNS \quad (1)$$

where  $K$  is a coefficient which takes into consideration different crystallographic situations. A detailed treatment of  $\gamma_{cpss}$  is given in Appendix A. Thus, the method reduces the data collection to the measurements of slip band densities and their heights in the area of interest.

The electropolished Al-SiC disks were separated into three groups: A, B and C. Each group was heated to about 823 K and then cooled as follows: group A, furnace cooled; group B, air cooled; group C, quenched in alcohol.

Since the surface of each disk had a high quality polish, slip bands could be observed around the SiC in an optical microscope. Slip band density and height measurements were obtained using a Zeiss interference microscope. Areas containing slip bands were photographed in white light and in green monochromatic light. Pictures taken in white light gave the actual image of the slip bands. Pictures of the same areas taken in monochromatic light gave interference fringe patterns (Figs. 2-4). Thus, the correlation between slip bands and interference fringes was established.

When a furrow is present in the plane surface of the object, the straight interference bands are deflected by the furrow and the furrow depth  $t$  can be determined from the deflection:

$$t = \frac{d \lambda}{b 2} \quad (2)$$

where  $d$  is the deflection of the interference band,  $b$  is the band interval, taken as the distance from the middle of one band to the middle of the next band and  $\lambda/2 = 0.27 \mu\text{m}$  for the thallium light. Band deflection can be estimated to be one-tenth of the band interval. Thus the height measurements can be as accurate as  $\pm 0.1 \times 0.27 = \pm 0.027 \mu\text{m}$ .

The slip band density was determined by using the "mesh" method which consisted of the following. Pictures of slip band images and interference patterns were enlarged to 10 cm  $\times$  12.5 cm on high contrast photographic paper. After that, a transparent plastic

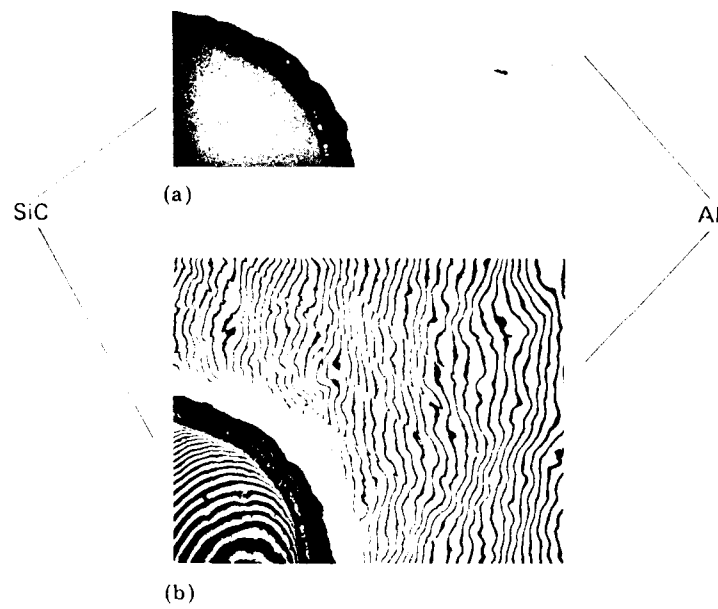


Fig. 2. (a) Slip bands and (b) interference fringe patterns of different areas around the SiC. (Magnification, 32 $\times$ .)

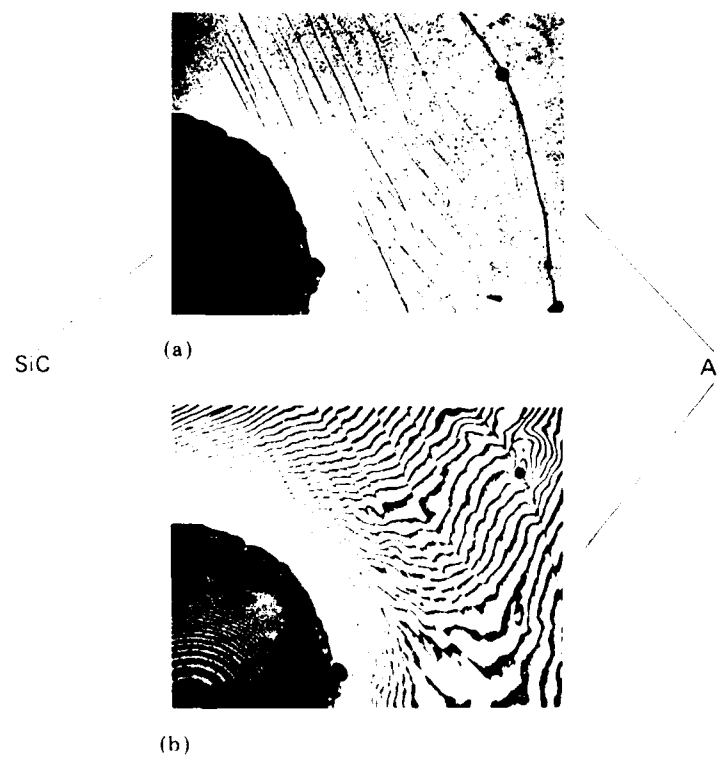


Fig. 3. (a) Slip bands and (b) interference fringe patterns of different areas around the SiC. (Magnification, 32 $\times$ .)

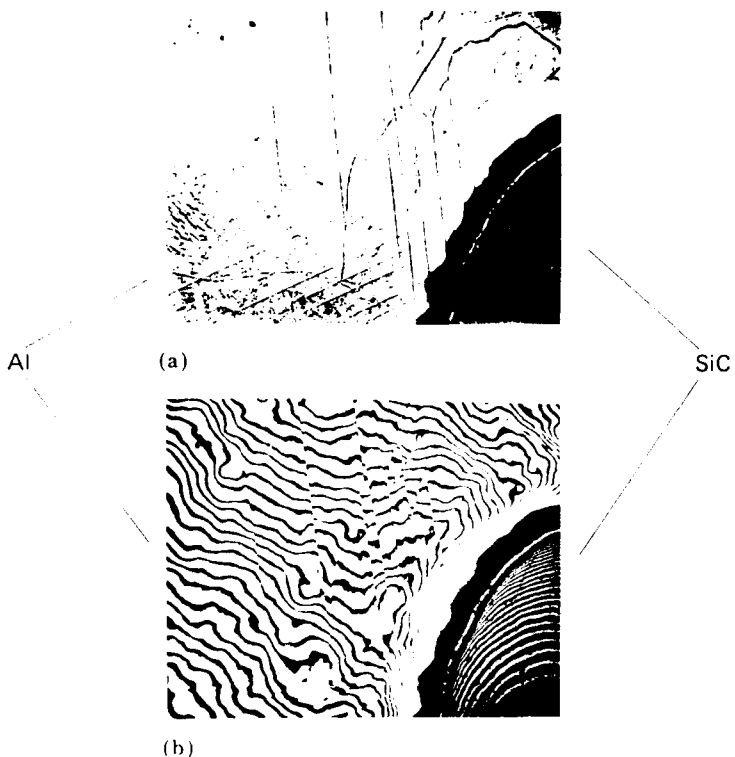


Fig. 4. (a) Slip bands and (b) interference fringe patterns of different areas around the SiC. (Magnification, 32 $\times$ .)

film with a square mesh of a specific size ( $1.0\text{ cm} \times 1.0\text{ cm}$  square for pictures with a magnification of  $80\text{X}$  and  $2.5\text{ cm} \times 2.5\text{ cm}$  square for pictures with a magnification of  $200\text{X}$ ) was overlaid on the photograph and the total length of the slip bands within each square along the radial direction was measured. If  $M$  is the magnification of the picture,  $L$  (m) the total length of slip bands in one square and  $A$  ( $\text{mm}^2$ ) the area of the square, then the slip band density  $N$  is

$$N = M \frac{L}{A} \times 10^{-3} \mu\text{m}^{-1} \quad (3)$$

The accuracy of slip band density measurements is much higher than that of height measurements. Therefore, the main source of error in combined plastic shear strain  $\gamma_{\text{cpss}}$  evaluation is the height of the slip band (provided that, of course, the assumptions and results of discussion given in Appendix A are reasonably correct).

### 2.1. Hot-stage experiment

Two Al-SiC disks were reduced in diameter to 7 mm and thermocycled in the hot stage of

a Leitz optical microscope. A reduction in size was necessary in order to fit the holder into the hot stage. The entire thermocycle was recorded on videotape using an RCA industrial television camera. The time was recorded by means of a digital generator interfaced to the recording unit, and the temperature was recorded on the sound track of the tape at 20 K intervals. The total length of the thermocycle was approximately 8 min. The maximum temperatures were around 873 K. The heating and cooling rates were around  $100\text{ K min}^{-1}$ .

## 3. EXPERIMENTAL RESULTS

### 3.1. Combined plastic shear strain

The experimentally determined values of combined plastic shear strain  $\gamma_{\text{cpss}}$  are presented in Tables 3-5. These combined plastic shear strains  $\gamma_{\text{cpss}}$  are plotted *versus* distance in the form of a histogram in Fig. 5. In the same figure we have a plot of effective strain  $\bar{\epsilon}$  which was determined theoretically (see Appendix B). The histogram represents the

TABLE 3

Combined plastic shear strain  $\gamma_{cpss}$  for group A samples (furnace cooled)

Sample	Path <sup>a</sup>	Combined plastic shear strain <sup>b</sup> $\gamma_{cpss}$ (%) for the following distances from the Al-SiC interface <sup>c</sup>				
		$6.25 \times 10^{-2} \text{ mm}$	$18.75 \times 10^{-2} \text{ mm}$	$31.25 \times 10^{-2} \text{ mm}$	$43.75 \times 10^{-2} \text{ mm}$	$56.25 \times 10^{-2} \text{ mm}$
1	1	0.86	0.35	0.18	0.09	0.026
1	2	0.61	0.40	0.22	0.06	0.07
1	3	0.41	0.140	0.24	0.08	
1	4	0.26	0.21	0.19	0.16	
1	5	0.42	0.32	0.32	0.13	0.03
1	6	0.51	0.41	0.30	0.08	
2	1	0.30	0.21	0.06		
2	2	0.45	0.28			
3	1	0.43	0.24	0.22	0.22	0.22
3	2	0.26	0.27	0.22	0.11	
3	3	0.39	0.22	0.26	0.16	
3	4	0.46	0.18	0.23		
3	5	0.45	0.26			
4	1	0.43	0.24	0.04		
Average		0.44	0.24	0.21	0.16	0.05

<sup>a</sup>The path is the route in the radial direction from the Al-SiC interface into the matrix, which was selected for slip band density and height measurements. Selection was based on the amount of slip that occurred, and those routes were selected in which the amount of slip bands appeared to be the greatest.

<sup>b</sup>The given strain is actually the result of the product  $NS$ . It does not include the coefficient  $K$  which was found to be equal to 3 (see Appendix A). Values of  $\gamma_{cpss}$  that incorporate  $K$  are given in Table 6.

<sup>c</sup>The distance given here is the distance from the Al-SiC interface to the centers of the first, second etc. squares. Therefore, values of  $\gamma_{cpss}$  represent the strain over the entire square.

TABLE 4

Combined plastic shear strain  $\gamma_{cpss}$  in group B samples (air cooled)

Sample	Path <sup>a</sup>	Combined plastic shear strain <sup>b</sup> $\gamma_{cpss}$ (%) for the following distances from the Al-SiC interface <sup>c</sup>					
		$6.25 \times 10^{-2} \text{ mm}$	$18.75 \times 10^{-2} \text{ mm}$	$31.25 \times 10^{-2} \text{ mm}$	$43.75 \times 10^{-2} \text{ mm}$	$56.25 \times 10^{-2} \text{ mm}$	$68.75 \times 10^{-2} \text{ mm}$
1	1	0.34	0.32	0.35	0.13		
1	2	0.25	0.25	0.17	0.19	0.13	0.11
1	3	0.56	0.31	0.19	0.11		
1	4	0.47	0.55				
1	5	0.25	0.07	0.014	0.08		
2	1	0.23	0.17				
4	1	0.65	0.41				
4	2	0.47	0.22				
4	3	0.54	0.29	0.1			
4	4	0.31	0.21	0.25			
4	5	0.48	0.25				
Average		0.41	0.27	0.18	0.12	0.13	0.11

<sup>a</sup>The path is the route in the radial direction from the Al-SiC interface into the matrix, which was selected for slip band density and height measurements. Selection was based on the amount of slip that occurred, and those routes were selected in which the amount of slip bands appeared to be the greatest.

<sup>b</sup>The given strain is actually the result of the product  $NS$ . It does not include the coefficient  $K$  which was found to be equal to 3 (see Appendix A). Values of  $\gamma_{cpss}$  that incorporate  $K$  are given in Table 6.

<sup>c</sup>The distance given here is the distance from the Al-SiC interface to the centers of the first, second etc. squares. Therefore, values of  $\gamma_{cpss}$  represent the strain over the entire square.

TABLE 5

Combined plastic shear strain  $\gamma_{cpss}$  in group C samples (quenched)

Sample	Path <sup>a</sup>	Combined plastic shear strain <sup>b</sup> $\gamma_{cpss}$ (%) for the following distances from the Al-SiC interface <sup>c</sup>		
		$6.25 \times 10^{-2}$ mm	$18.75 \times 10^{-2}$ mm	$31.25 \times 10^{-2}$ mm
1	1	0.40	0.16	
1	2	0.19	0.27	
1	3	0.69		
2	1	0.37	0.29	0.16
2	2	0.31	0.11	0.05
2	3	0.22	0.24	0.12
2	4	0.55	0.23	0.14
3	1	0.31	0.18	
3	2	0.44	0.24	0.23
4	1	0.25	0.21	0.08
4	2	0.25	0.10	0.04
4	3	0.18	0.13	0.05
Average		0.33	0.20	0.1

<sup>a</sup>The path is the route in the radial direction from the Al-SiC interface into the matrix, which was selected for slip band density and height measurements. Selection was based on the amount of slip that occurred, and those routes were selected in which the amount of slip bands appeared to be the greatest.

<sup>b</sup>The given strain is actually the result of the product  $NS$ . It does not include the coefficient  $K$  which was found to be equal to 3 (see Appendix A). Values of  $\gamma_{cpss}$  that incorporate  $K$  are given in Table 6.

<sup>c</sup>The distance given here is the distance from the Al-SiC interface to the centers of the first, second etc. squares. Therefore, values of  $\gamma_{cpss}$  represent the strain over the entire square.

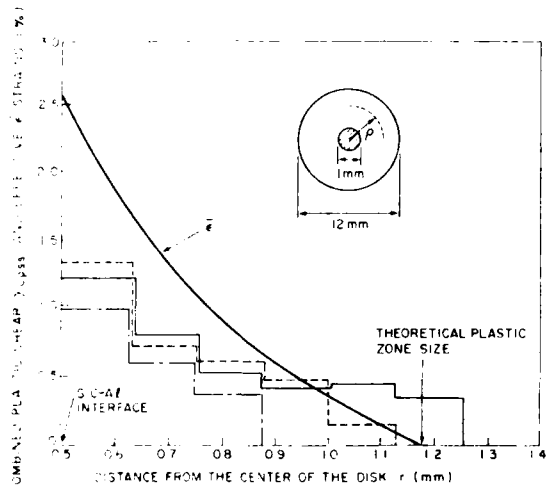


Fig. 5. Theoretical  $\bar{\epsilon}$  vs.  $r$  and experimental  $\gamma_{cpss}$  vs.  $r$  profiles around the SiC in Al-SiC composite disks thermocycled between 298 and 823 K ( $\rho$  is the plastic zone radius): - - -, group A; - - - - , group B; - - - - - , group C.

actual discrete character of the measurements of  $\gamma_{cpss}$ . Each horizontal portion of the histogram corresponds to the average value of

$\gamma_{cpss}$  obtained from the increment of the area of the specimen.

The largest combined plastic shear strain  $\gamma_{cpss}$  of 1.3% was observed at the Al-SiC interface in group A samples; group C showed the smallest amount of strain, 0.99% (Table 6). In addition, the extent of the plastic zone (*i.e.* the largest distance from the interface at which slip bands can still be measured) was smaller in samples from group C than in samples from groups A and B. This result corresponds to the effect of strain rate (which is proportional to the cooling rate) on the relative amount of plastic and elastic strains during deformation. Generally, higher heating and cooling rates will cause the elastic stresses to be larger, and lower heating and cooling rates will allow greater plastic relaxation [7].

The height of the slip bands was measured to  $\pm 0.1$  of a band interval. This gives an error of  $\pm 0.1 \times 0.27 \mu\text{m} = \pm 0.027 \mu\text{m}$  in the height values. As was mentioned before, the slip band density measurements introduce much less error. Therefore, the error range for

TABLE 6

Values of  $\gamma_{cpss}$  incorporating  $K$  for group A, B and C samples

Group	Combined plastic shear strain $\gamma_{cpss}$ (%) for the following distances from the Al-SiC interface					
	$6.25 \times 10^{-2} \text{ mm}$	$18.75 \times 10^{-2} \text{ mm}$	$31.25 \times 10^{-2} \text{ mm}$	$43.75 \times 10^{-2} \text{ mm}$	$56.25 \times 10^{-2} \text{ mm}$	$68.75 \times 10^{-2} \text{ mm}$
A	1.32	0.72	0.63	0.48	0.15	
B	1.23	0.81	0.54	0.36	0.39	0.83
C	0.99	0.60	0.3			

$\gamma_{cpss}$  determination can be evaluated as  $\pm (0.027/0.135) \times 100 \approx 20\%$  where  $0.135 \mu\text{m}$  is taken as the average slip band height. This is obviously a large error range.

### 3.2. Hot-stage observations

#### 3.2.1. Heating

Slip bands began to appear even before the temperature reached 373 K and were forming as widely spaced deep lines. As the temperature increased, the density of the slip bands increased also, reaching an apparent maximum at around 573 K. At around 533 K a new group of broken lines began to form with no relation to the previously formed slip bands. The development of these lines became more intensive at higher temperatures. When the temperature approached about the 653 K mark, the separation between the matrix and the SiC became fairly visible. At approximately 693 K, slip bands began to fade and disappeared almost totally by the time the temperature reached 853-873 K. At the maximum temperatures, the surface did not appear as flat as it did at the beginning.

#### 3.2.2. Cooling

On cooling, previously formed slip band patterns began to show up again but they did not reach the size and extent of the former slip band patterns. The development of the slip bands in new areas was not observed.

The broken line which encircled the entire SiC particle began to develop radial spokes that connected this line to the interface. When the sample cooled to room temperature, the surface of the sample remained rippled.

Subsequent thermocycles did not show any changes in slip band morphology. A broken line around the SiC cylinder became much more clearly defined with repeated thermocycles. The matrix appeared to be separated from the particle all the time.

## 4. DISCUSSION

Composite models discussed in the literature for the theoretical determination of stresses and strains in the matrix (spherical particle in a matrix, long composite cylinder etc.) cannot be applied to a short composite disk. Therefore, an attempt was made to evaluate the radius of the plastic zone and the plastic strains around the SiC particle using the approach described in Appendix B.

The resultant profile of the effective plastic strain  $\bar{\epsilon}$  around the SiC particle and the extent of the plastic zone are shown in Fig. 5. As can be seen,  $\rho \approx 1.15 \text{ mm}$ , and  $\bar{\epsilon} = 2.5\%$  at the interface. The theoretical plastic strain is higher than the observed plastic strain, and the theoretical plastic zone radius is smaller than the observed plastic zone radius. The theoretical plastic zone size is estimated on the assumption that deformation is homogeneous, *i.e.* uniform around the SiC particle. In the real case we have "bursts" of plastic flow in accordance with a particular crystallographic situation. Thus, the extent of the burst of plastic deformation can be larger than that of homogeneous deformation since the same amount of metal flow must be accommodated. The explanation of the difference between observed and calculated strains can be given as follows. On heating, because of the differential expansion between the aluminum and the SiC, the aluminum matrix tends to pull away from the SiC. If the bonding between the aluminum and the SiC is sufficient to resist the pulling action, the matrix undergoes deformation proportional to  $\Delta T$  of the cycle. If, however, the bonding is weak, the matrix breaks away from the SiC at a certain temperature  $T_B$ , and subsequent temperature increase has no effect on matrix deformation since it is now free to expand.

Hot-stage observations showed that slip band formation started at a temperature of less than 373 K. Accurate evaluation of the temperature at which slip became visible was not possible because the thermocouple in the hot stage was not sensitive enough in the temperature range between 298 and 373 K. It was noticed that more slip bands were formed on the heating half of the thermocycle than on the cooling half. The slip band arrangement on the cooling half repeated the arrangement developed during the heating half. When the temperature approached about 773 K, slip bands began to disappear. This can be explained from the surface tension point of view.

Another possible explanation of the stoppage of slip band development is that the aluminum matrix breaks away from the SiC and continues to expand freely without any restraint from the SiC. It is also possible that very fine slip bands still continued to form (high temperature creep, for example), but we did not see this because of the limitation in resolution of our optical system. It should be mentioned, however, that the disappearance of the slip bands corresponds to a similar observation made by Lammers *et al.* [14] in their *in situ* transmission electron microscopy investigation of Al-SiC composites. They observed "slip lines" in thermally cycled transmission electron microscopy foils, and these slip lines disappeared at high temperatures.

The fact that slip band patterns formed on cooling repeat themselves shows that the same slip systems are engaged in the "reversed" deformation, proving at least partially that there is a certain reversibility of the plastic deformation that occurs when the load is reversed.

The broken lines that form around SiC appeared to be the boundaries of recrystallized grains. If this is indeed the case, recrystallization took place at the interface and occurred very rapidly (2-3 min).

## 5. CONCLUSION

From the experimental data and the theoretical model the following conclusions were obtained.

(1) A new experimental technique for measuring local plastic strains was developed and utilized in the Al-SiC system.

(2) The theoretical treatment of the short composite cylinder gave the distribution and extent of the plastic strains, which are in fair agreement with the experimental results. There is a disagreement, however, between the experimental and theoretical values of plastic strains immediately at the Al-SiC interface.

(3) An Al-SiC bond is a very important factor influencing the plastic deformation around SiC particles.

## REFERENCES

- 1 R. J. Arsenault and R. M. Fisher, *Scr. Metall.*, 17 (1983) 67.
- 2 R. J. Arsenault and R. M. Fisher, in J. Carlsson and M. Ohlson (eds.), *Proc. 4th Int. Conf. on the Mechanical Behavior of Materials, Stockholm*, 1983, Vol. 1, Pergamon, Oxford, 1983, p. 451.
- 3 R. J. Arsenault, *Mater. Sci. Eng.*, 64 (1984) 171.
- 4 R. J. Arsenault and C. S. Pande, *Scr. Metall.*, 18 (1984) 1131.
- 5 J. K. Lee, Y. Y. Earmme, H. I. Aaronson and K. C. Russell, *Metall. Trans. A*, 11 (1980) 1837.
- 6 C. A. Hoffman, *J. Eng. Mater. Technol.*, 95 (1973) 55.
- 7 G. Garmong, *Metall. Trans.*, 5 (1974) 2183.
- 8 G. J. Dvorak, M. S. M. Rao and J. Q. Tarn, *J. Compos. Mater.*, 7 (1973) 194.
- 9 R. L. Mehan, *Metal Matrix Composites, ASTM Spec. Tech. Publ.* 438, 1968, p. 29.
- 10 G. E. Dieter, *Mechanical Metallurgy*, McGraw-Hill, New York, 2nd edn., 1976, p. 51.
- 11 *Metals Handbook*, Vol. 1, American Society for Metals, Metals Park, OH, 1961.
- 12 A. Taylor and R. M. Jones, in J. R. O'Connor and J. Smiltens (eds.), *Silicon Carbide*, Pergamon, Oxford, 1960, p. 147.
- 13 *Handbook of Material Science*, Vol. II, CRC Press, West Palm Beach, FL, 1975.
- 14 M. E. Lammers, R. J. Arsenault and R. M. Fisher, to be published.

## APPENDIX A

### A.1. Combined plastic shear strain $\gamma_{cpss}$

The relation between the slip band density  $N$ , the amount  $S$  of slip or displacement on the band and the plastic strain  $\gamma$  has been discussed in a number of publications [A1-A3]. In their classical works, Yamaguchi *et al.* [A1] and Brown [A2] found direct proportionality between the strain and amount of slip during plastic deformation. Cottrell

[A3] summarized their results and arrived at the expression  $\gamma = NS$  for the case when there is only one slip system in operation.

For a multiple-slip-system case, however, this expression must be modified to take into account the different crystallographic orientations of the slip systems.

The attempt to carry out this modification is offered in the present work and consists of the following: the highlights of the one-slip-system case; a description of the rigorous approach for multislip cases; a simplified approximation with the introduction of the combined plastic shear strain  $\gamma_{\text{cplss}}$  concept.

Let us assume first that slip occurs in one slip system only. Let us consider an imaginary block (Fig. A1) that is cut out of material in such a way that slip planes are perpendicular to the facets of the block. This block is oriented in such a way that its height is measured along the  $z$  axis.

Let us suppose that a shear stress  $\tau_{yz}$  is applied to the block which causes the block to slip as shown in Fig. A1.

By definition, the shear strain in this case is expressed as

$$\gamma_{yz} = \frac{\Delta S_y}{Z}$$

where  $\Delta S_y$  is the total displacement in the  $y$  direction and  $Z$  is the height of the block.

The total displacement  $\Delta S_y$  is equal to the sum of the displacements on each slip plane, *i.e.*

$$\Delta S_y = \sum_{i=1}^n S_i$$

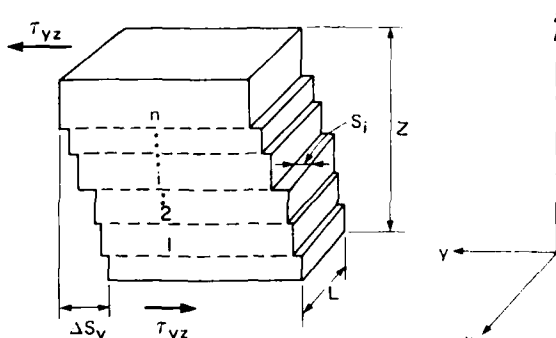


Fig. A1. Hypothetical block with one slip system.  $S_i$  is the displacement on the slip plane;  $\Delta S_y$  is the total displacement along the  $y$  axis.

where  $S_i$  is the slip or the displacement in the  $i$ th band\*. (Here  $S_i$  is analogous to the furrow depth  $t$  in eqn. (2).) If  $n$  is the total number of slip bands involved in the slip and  $\bar{S}_y$  is the average value of slip per one band, then

$$\begin{aligned} \Delta S_y &= \sum_{i=1}^n S_i \\ &\approx n \bar{S}_y \end{aligned}$$

As can be seen from Fig. A1,  $n$  is the number of intersects that the  $z$  axis makes with the slip bands and is equal to the total number of slip bands along the  $z$  direction. If the number  $N$  of slip bands per unit length along  $z$  is known (*i.e.* the slip band density), then

$$n = Nz$$

where  $N$  ( $\text{cm}^{-1}$ ) is the slip band density along the  $z$  direction. Now the total strain  $\gamma_{yz}$  can be expressed [A3] as

$$\begin{aligned} \gamma_{yz} &= \frac{\Delta S_y}{z} \\ &= \frac{n \bar{S}_y}{z} \\ &= \frac{Nz \bar{S}_y}{z} \\ &= N \bar{S}_y \end{aligned} \tag{A1}$$

$N$  can be evaluated as the total slip band length divided by the total area. To do this we can take eqn. (A1) and multiply the numerator and the denominator by the width  $L$  of the block:

$$\begin{aligned} \gamma_{yz} &= \frac{\Delta S_y}{z} \\ &= \frac{n \bar{S}_y}{z} \\ &= \frac{n \bar{S}_y L}{z L} \\ &= \frac{(nL) \bar{S}_y}{z L} \\ &= N_A \bar{S}_y \end{aligned}$$

\*Generally, the slip direction does not have to be perpendicular to the  $y$  plane as shown in Fig. A1. However, despite this and other rather crude assumptions that are made later, the purpose is to show the complexity of the rigorous treatment.

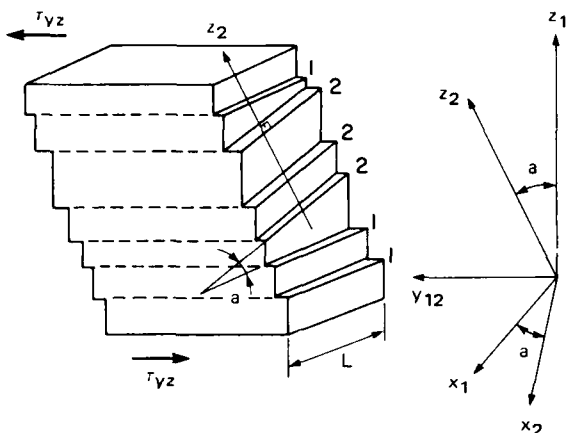


Fig. A2. Hypothetical block with two operational slip systems 1 and 2.

Here,  $nL$  is the total length of the slip bands on the side of the block,  $zL$  is the total area of this side and  $N_A$  ( $\text{cm}^{-1}$ ) =  $nL/zL$  is the slip band density. Thus,

$$\gamma_{yz} = N\bar{S}_y$$

In the case when more than one slip system is involved in plastic deformation, slip bands are not parallel but instead each slip system has its own orientation\* (Fig. A2). In this situation the equation for shear strain has to be modified to take into account the different orientations of the slip bands. The rigorous way to do this would be as follows.

(1) Determine the plastic strain  $\gamma_{y,z_1}$  using the same approach described previously for slip system 1.

(2) Rotate the coordinate system  $x_1, y_1, z_1$  to align it with system  $x_2, y_2, z_2$  where  $z_2$  is the direction perpendicular to slip bands in slip system 2. In the coordinate system  $x_2, y_2, z_2$ , determine  $\gamma_{y,z_2}$  using the relation

$$\gamma_{y,z_2} = a_{y,i} a_{z,j} \gamma_{ij} \quad (A2)$$

where  $a_{y,i} a_{z,j}$  is the rotation matrix and  $\gamma_{ij}$  is the strain tensor in the  $x_1, y_1, z_1$  coordinate system and is given by

$$\gamma_{ij} = \begin{bmatrix} 0 & 0 & 0 \\ 0 & 0 & \gamma_{y,z_1} \\ 0 & \gamma_{z,y_1} & 0 \end{bmatrix}$$

\*Here, the hypothetical assumption is made that slip planes from the second slip system are also perpendicular to the facets of the block.

(3) Combine the terms determined in step (3) with the terms from step (1) having the same indices. Now we have obtained the total strain tensor  $\epsilon_{ij}$  in the  $x_1, y_1, z_1$  coordinate system due to all slip systems:

$$\epsilon_{ij} = \begin{bmatrix} 0 & 0 & 0 \\ 0 & 0 & \gamma_{yz} \\ 0 & \gamma_{zy} & 0 \end{bmatrix}$$

(4) Determine the principal components of the strain tensor  $\epsilon_{ij}$  solving the following equation:

$$\begin{bmatrix} -\lambda & 0 & 0 \\ 0 & -\lambda & \gamma_{yz} \\ 0 & \gamma_{zy} & -\lambda \end{bmatrix} = 0 \quad (A3)$$

for  $\lambda$ . The three roots  $\lambda_1, \lambda_2$  and  $\lambda_3$  are the three principal strains  $\epsilon_1, \epsilon_2$  and  $\epsilon_3$  respectively.

(5) Determine the effective strain

$$\bar{\epsilon} = \frac{2^{1/2}}{3} ((\epsilon_1 - \epsilon_2)^2 + (\epsilon_2 - \epsilon_3)^2 + (\epsilon_3 - \epsilon_1)^2)^{1/2}$$

As a result of all these steps we finally get one data point on the plot  $\bar{\epsilon} = f(r)$ . This procedure is simple in principle but complicated to implement, since the crystallographic orientation has to be determined for each grain. As an alternative way of estimating the amount of plastic deformation that occurred around the SiC particle, the following approximation is offered.

First, the concept of *combined plastic shear strain*  $\gamma_{cpss}$  is introduced. We shall define  $\gamma_{cpss}$  as

$$\gamma_{cpss} = K N \bar{S}$$

where  $\bar{S}$  is the average step height. In general, the slip plane is not perpendicular to the surface and therefore the coefficient  $K$  is incorporated.  $K$  is a coefficient which will be evaluated later.  $N$  is the slip band density, which is obtained from the total slip band length of all slip systems divided by the area where the total slip band length is the length of all the slip bands enclosed in a selected area (e.g. a square mesh of some net). The selection of the size of the area is based on considerations of the scale. It is realized that the combined plastic shear strain  $\gamma_{cpss}$  has no direct correlation with the effective strain  $\bar{\epsilon}$ , the octahedral shear strain  $\gamma_{oct}$  or any other

specific strain. However, the relative simplicity in the determination of  $\gamma_{cpss}$  and the fact that  $\gamma_{cpss}$  takes into account direct proportionality between the amount of plastic deformation and the slip band density makes it very attractive for use as a criterion for plastic deformation in our case and in other similar cases in general.

#### A.2. Determination of the coefficient $K$

The coefficient  $K$  takes into account the different crystallographic orientations of slip systems. Let us consider the case when we have three slip systems operating, *i.e.* we see three slip band groups. The individual slip systems contribute the strain  $N_1 \bar{S}_1$ ,  $N_2 \bar{S}_2$  and  $N_3 \bar{S}_3$  to the total  $\gamma_{cpss}$ , *i.e.*

$$\gamma_{cpss} = N_1 \bar{S}_1 + N_2 \bar{S}_2 + N_3 \bar{S}_3$$

where  $N_1$ ,  $N_2$  and  $N_3$  are the slip band densities and  $\bar{S}_1$ ,  $\bar{S}_2$  and  $\bar{S}_3$  are the average displacements on the band within each slip system, given by

$$\bar{S}_1 = \frac{\bar{S}_{M1}}{\sin \theta_1}$$

$$\bar{S}_2 = \frac{\bar{S}_{M2}}{\sin \theta_2}$$

and

$$\bar{S}_3 = \frac{\bar{S}_{M3}}{\sin \theta_3}$$

where  $\bar{S}_{M1}$ ,  $\bar{S}_{M2}$  and  $\bar{S}_{M3}$  are the average heights of the slip bands in the three slip systems, measured perpendicularly to the surface, and  $\theta_1$ ,  $\theta_2$  and  $\theta_3$  are the angles between the slip planes and the surface plane. Thus,

$$\gamma_{cpss} = N_1 \bar{S}_{M1} \frac{1}{\sin \theta_1} + N_2 \bar{S}_{M2} \frac{1}{\sin \theta_2} + N_3 \bar{S}_{M3} \frac{1}{\sin \theta_3}$$

Now we shall assume that the amounts of strain  $N_1 \bar{S}_{M1}$ ,  $N_2 \bar{S}_{M2}$  and  $N_3 \bar{S}_{M3}$  are approximately equal because of the symmetry of the specimen and provided that no voids or cracks are created. Furthermore,

$$\gamma_{cpss} = N \bar{S}_M \left( \frac{1}{\sin \theta_1} + \frac{1}{\sin \theta_2} + \frac{1}{\sin \theta_3} \right)$$

or

$$\gamma_{cpss} = K N \bar{S}_M$$

where

$$K = \frac{1}{\sin \theta_1} + \frac{1}{\sin \theta_2} + \frac{1}{\sin \theta_3}$$

Let us evaluate the range within which  $K$  can change by considering a unit triangle (Fig. A3). Let the directions shown on the triangle correspond to the poles of the surface of the sample. Then the values of  $K$  would be as shown in Table A1. The average value of  $K$  is about 4.5 when three slip systems are operating. Thus, the average correction factor per one slip system is  $4.5/3 = 1.5$ . In general, slip band densities were measured along directions going through areas where two slip systems, *i.e.* two sets of slip bands, were present. Thus for, two slip systems,  $K = 2 \times 1.5 = 3$ .

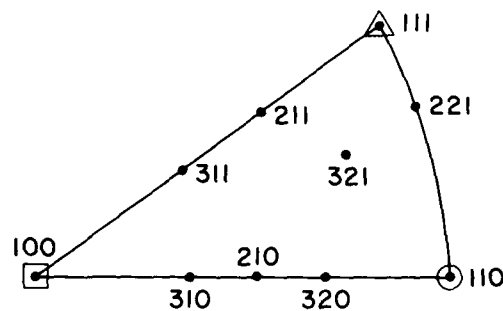


Fig. A3. Some orientations of the sample for which values of  $K$  were determined.

TABLE A1

Values of  $K$  corresponding to the orientations shown in Fig. A3

Surface plane pole <i>K</i> for (111) slip plane	(111)	(110)	(100)	(210)	(211)	(221)	(310)	(311)	(320)	(321)
	3.2	3.7	3.7	3.66	5.1	5.9	3.6	4.2	3.1	4.9

## References for Appendix A

A1 K. Yamaguchi, *Sci. Paper Inst. Phys. Chem. Res. Tokyo*, 8 (1928) 289; 11 (1929) 151.  
 A2 A. F. Brown, *J. Inst. Met.*, 80 (1951) 115.  
 A3 A. H. Cottrell, *Dislocations and Plastic Flow in Crystals*, Clarendon, Oxford, 1965, p. 157.

## APPENDIX B

Among the several composite models described in the literature, there is one that appears to be close to our case; this is known as the long-composite-cylinder model. It consists of long continuous fiber surrounded by the metal matrix. This model implies that plastic strain in the direction of the fiber (the  $z$  direction) resulted from unequal expansion or contraction of fiber and that the matrix is a constant, *i.e.*  $\epsilon_z = dl/l = \text{constant}$  where  $l$  is the length of the fiber.

Therefore, the total plastic strain state becomes a plane strain case which enables two other plastic strains  $\epsilon_r$  and  $\epsilon_\theta$  to be found without difficulty. Although short composite cylinders have the same symmetry as long composite cylinders, the strain in the  $z$  direction is not a constant but is in general a function of two variables: (1) the distance from the interface and (2) the position along the  $z$  axis. Since  $\epsilon_z \neq \text{constant}$ , the long-cylinder approach cannot be used in our case.

We shall discuss the case shown in Fig. B1. Let us consider an Al-SiC disk that cools from a temperature  $T$ . As a result of cooling, a certain amount of aluminum will be pushed back because of the differential shrinkage of

SiC and aluminum. If we did not have SiC in the center of the aluminum disk, the aluminum ring would shrink without any restraint and the size of the bore would be reduced by

$$U_a = \Delta a = a \Delta \alpha \Delta T$$

where  $a$  is the radius of the SiC,  $\Delta \alpha$  ( $\approx 25 \times 10^{-6} \text{ K}^{-1}$ ) is the difference between the coefficient of thermal expansion of aluminum and that of SiC,  $\Delta T$  ( $\approx 500 \text{ K}$ ) is the temperature interval and  $U_a$  is the displacement at the interface. The reduction in the radius of the bore does not occur when SiC is present in the center of the aluminum disk. The amount of aluminum that is not allowed to go towards the center of the bore would cause plastic flow of the adjacent matrix in all directions away from the SiC. Thus, some of the matrix will spill out (as shown in Fig. B1). As we go further away from the interface, the plastic flow is restricted by the matrix that surrounds the central portion. Two regions can be considered: the plastic region that we assume is adjacent to the SiC and the elastic region that encloses the plastic region. Let us make the following assumptions.

(1) In the plastic zone the matrix is a perfectly plastic material, *i.e.* no work hardening occurs.

(2) At the starting temperature  $T$  of 773 K, SiC and aluminum are just in contact with one another.

(3) The profile of the aluminum which has spilt out is a straight line.

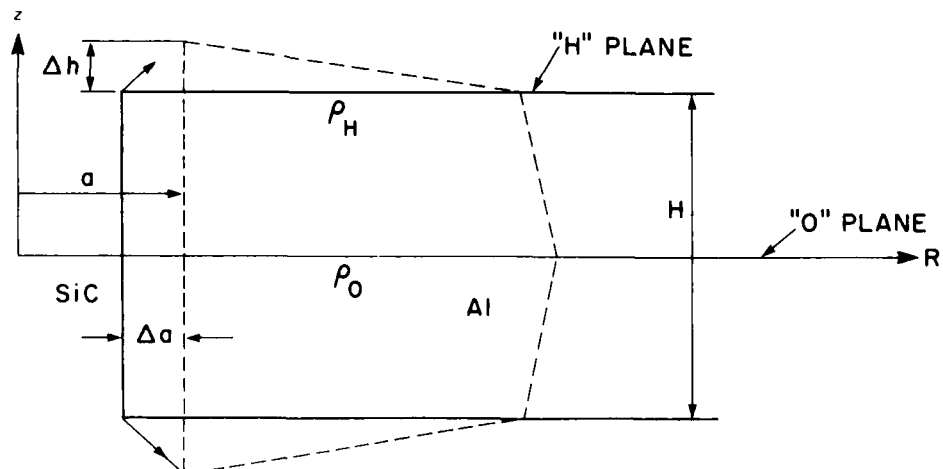


Fig. B1. Schematic representation of the plastic-elastic shell around the SiC.

(4) The plastic-elastic front is also a straight line.

Now let us consider the radius  $\rho$  of the plastic zone. It is a function of the vertical position of the transverse plane in which  $\rho$  is considered. According to our assumption,

$$\rho = \rho_0 - qz$$

(the equation of the straight line) where  $\rho_0$  is the plastic zone radius in the "0" plane, which is the plane of symmetry between the upper and lower halves of the composite disk. To determine  $q$  we let  $z = \frac{1}{2}H$ , i.e. the top of the "H" plane is considered. When  $z = \frac{1}{2}H$ ,  $\rho = \rho_H$ . Therefore

$$\rho_H = \rho_0 - q \frac{1}{2}H$$

From this

$$q = 2(\rho_0 - \rho_H) \frac{1}{H}$$

and now

$$\rho = \rho_0 - 2(\rho_0 - \rho_H) \frac{z}{H} \quad (B1)$$

Let us consider now the portion of the matrix that spills out. From the triangle shown in Fig. B2 we can write

$$U_z = \Delta h \frac{\rho_H - r}{\rho_H - a} \quad (B2)$$

where  $U_z$  is the vertical displacement. Generally speaking, the vertical displacement  $U_z$  is a function of  $z$  and  $r$ , i.e.

$$U_z = \phi\{f(z), g(r)\}$$

Equation (B2) gives only an expression for  $U_z$  when the "H" plane is considered. The problem thus is to find a general expression for  $U_z$ . To do this, let us replace  $\rho_H$  in eqn.

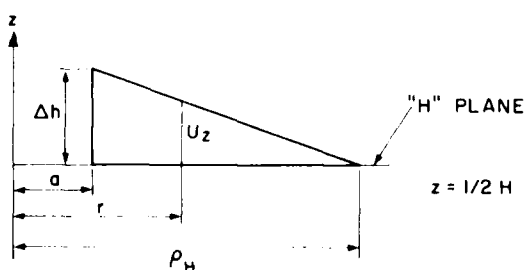


Fig. B2. "Spill-out" portion of the aluminum matrix.

(B2) with a general expression for  $\rho$  (eqn. (B1)) when  $z = \frac{1}{2}H$

$$U_z = \Delta h \frac{\rho_0 - 2(\rho_0 - \rho_H) \frac{1}{2} - r}{\rho_0 - 2(\rho_0 - \rho_H) \frac{1}{2} - a}$$

$$\Delta h = \frac{1}{2}H \Delta \alpha \Delta T$$

and

$$U_z = \frac{1}{2}H \Delta \alpha \Delta T \frac{\rho_0 - 2(\rho_0 - \rho_H) \frac{1}{2} - r}{\rho_0 - 2(\rho_0 - \rho_H) \frac{1}{2} - a} \quad (B3)$$

If we simplify eqn. (B3) it reduces to eqn. (B2), but let us leave eqn. (B3) in its form and examine it in more detail. First let us substitute  $H = 1$  mm in eqn. (B3), since this is a convenient way of simplifying this expression and  $H = 1$  mm happens to be the actual height of our composite disks. Now we can rewrite eqn. (B3) as

$$U_z = \frac{1}{2} \Delta \alpha \Delta T \frac{\rho_0 - 2(\rho_0 - \rho_H) \frac{1}{2} - r}{\rho_0 - 2(\rho_0 - \rho_H) \frac{1}{2} - a} \quad (B4)$$

for  $z = \frac{1}{2}H$  or if we normalize  $z' = z/H = \frac{1}{2}$ . Let us check the values of  $U_z$  at different  $z$  values. First, let  $z = \frac{1}{2}$  ("H" plane), and so

$$U_z = \frac{1}{2} \Delta \alpha \Delta T \frac{\rho_0 - 2(\rho_0 - \rho_H) \frac{1}{2} - r}{\rho_0 - 2(\rho_0 - \rho_H) \frac{1}{2} - a}$$

Then, when  $r = a$ ,

$$U_z = \frac{1}{2} \Delta \alpha \Delta T = \Delta h$$

and, when  $r = \rho_H$ ,

$$U_z = 0$$

Let  $z = 0$  ("0" plane), and so  $U_z = 0$ , since the "0" plane is the plane of vertical symmetry. At this point we can see a certain logic in eqn. (B4), which enables us to suggest the general expression for  $U_z$  in the following form:

$$U_z = z' \Delta \alpha \Delta T \frac{\rho_0 - 2(\rho_0 - \rho_H)z' - r}{\rho_0 - 2(\rho_0 - \rho_H)z' - a} \quad (B5)$$

(since  $H = 1$ ). It is realized that eqn. (B5) lacks rigorous proof. However, since it incorporates our boundary conditions and since we do not have any additional information, it is reasonable to adopt eqn. (B5) and to see what results we can obtain and then to judge the validity of this expression. Let us consider the cylindrical coordinate system in which the  $z$  axis coincides with the  $z$  axis of our sample. By definition

$$\begin{aligned}
 \epsilon_r &= \frac{dU_r}{dr} \\
 \epsilon_\theta &= \frac{U_r}{r} \\
 \epsilon_z &= \frac{dU_z}{dz} \\
 \epsilon_z &= \frac{dU_z}{dz} \\
 &= \Delta\alpha \Delta T \frac{\rho_0 - 2(\rho_0 - \rho_H)z - r}{\rho_0 - 2(\rho_0 - \rho_H)z - a} + \\
 &\quad + z \Delta\alpha \Delta T \frac{2(\rho_0 - \rho_H)(a - r)}{[\rho_0 - 2(\rho_0 - \rho_H)z - a]} \tag{B5}^*
 \end{aligned}$$

Incompressibility requires that

$$\epsilon_r + \epsilon_\theta + \epsilon_z = 0$$

or

$$\frac{dU_r}{dr} + \frac{U_r}{r} + \epsilon_z = 0 \tag{B6}$$

Let us consider the "0" plane, where  $z = 0$ ; then

$$\epsilon_z = \Delta\alpha \Delta T \frac{\rho_0 - r}{\rho_0 - a} \tag{B7}$$

Equation (B6) then becomes

$$\frac{dU_r}{dr} + \frac{U_r}{r} + \Delta\alpha \Delta T \frac{\rho_0 - r}{\rho_0 - a} = 0 \tag{B8}$$

$$\frac{dU_r}{dr} + \frac{U_r}{r} + M - Nr = 0 \tag{B9}$$

where

$$M = \Delta\alpha \Delta T \frac{\rho_0}{\rho_0 - a}$$

and

$$N = \Delta\alpha \Delta T \frac{1}{\rho_0 - a}$$

The solution of eqn. (B9) is

$$U_r = -\frac{M}{2}r + \frac{C}{r} + \frac{N}{3}r^2 \tag{B10}$$

\*From here on we omit the superscript prime in  $z'$  and use  $z$  instead to prevent confusion, but it should be borne in mind that the value  $z$  is normalized with respect to  $H$ .

To find the constant  $C$  we use the boundary condition  $U_{r=a} = U_a = a \Delta\alpha \Delta T$ :

$$U_a = a \Delta\alpha \Delta T = -\frac{M}{2}a + \frac{C}{a} + \frac{N}{3}a^2$$

$$C = aU_a + \frac{M}{2}a^2 - \frac{N}{3}a^3$$

Now eqn. (B10) becomes

$$U_r = -\frac{M}{2}r + \frac{U_a a}{r} + \frac{Ma^2}{2r} - \frac{Na^3}{3r} + \frac{N}{3}r^2 \tag{B11}$$

Now we can find the strains  $\epsilon_r$ ,  $\epsilon_\theta$  and  $\epsilon_z$  for the "0" plane:

$$\begin{aligned}
 \epsilon_r &= \frac{dU_r}{dr} = -\frac{M}{2} - \frac{U_a a}{r^2} - \frac{Ma^2}{2r^2} + \frac{Na^2}{3r^2} + \frac{2}{3}Nr \\
 \epsilon_\theta &= \frac{U_r}{r} = -\frac{M}{2} + \frac{U_a a}{r^2} + \frac{Ma^2}{2r^2} - \frac{Na^3}{3r^2} + \frac{N}{3}r \\
 \epsilon_z &= M - Nr
 \end{aligned} \tag{B12}$$

Let us consider the tip of the plastic-elastic interface, i.e.  $r = \rho_0$ . Then ( $\epsilon_z = 0$  from eqn. (B7))

$$\begin{aligned}
 \epsilon_r &= -\epsilon_\theta \\
 &= -\frac{U_{\rho_0}}{\rho_0}
 \end{aligned} \tag{B13}$$

where  $U_{\rho_0}$  is the displacement of the tip of the plastic-elastic front:

$$U_{r=\rho_0} = U_{\rho_0}$$

Each point of the plastic-elastic front is in the state of incipient yielding, i.e.

$$\bar{\epsilon} = \epsilon_0$$

where  $\bar{\epsilon}$  is the effective strain at the interface and  $\epsilon_0$  is the yielding strain taken from the yielding condition of the tensile sample in uniaxial loading:

$$\sigma_y = E\epsilon_0$$

Therefore

$$\epsilon_0 = \frac{\sigma_y}{E}$$

$$\begin{aligned}
 &= \frac{11.73}{62 \times 10^3} \\
 &\approx 2 \times 10^{-4}
 \end{aligned}$$

where  $\sigma_y = 11.73 \text{ MPa}$  and  $E = 62 \times 10^3 \text{ MPa}$  for pure aluminum. Thus we have a system of equations:

$$\begin{aligned}\epsilon_r(r=\rho_0) &= -\frac{U_{\rho_0}}{\rho_0} \\ \epsilon_\theta(r=\rho_0) &= \frac{U_{\rho_0}}{\rho_0} \\ \epsilon_z(r=\rho_0) &= 0\end{aligned}\quad (\text{B14})$$

Applying the von Mises yielding condition,

$$\bar{\epsilon} = \frac{2^{1/2}}{3} \{(\epsilon_1 - \epsilon_2)^2 + (\epsilon_1 - \epsilon_3)^2 + (\epsilon_2 - \epsilon_3)^2\}^{1/2}$$

where  $\epsilon_1$ ,  $\epsilon_2$  and  $\epsilon_3$  are the principal strains. Generally speaking, the strains  $\epsilon_r$ ,  $\epsilon_\theta$  and  $\epsilon_z$  do not coincide with the principal strains  $\epsilon_1$ ,  $\epsilon_2$  and  $\epsilon_3$ , because of the existence of the shear component in the total strain tensor, which is given by

$$\gamma_{rz} = \frac{dU_z}{dr} + \frac{dU_r}{dz}$$

The components  $\gamma_{\theta r}$  and  $\gamma_{z\theta}$  are equal to zero because of the symmetry around SiC.

$$\frac{dU_z}{dr} = -\frac{\Delta\alpha \Delta T z}{\rho_0 - 2(\rho_0 - \rho_H)z - a}$$

for the "0" plane; when  $z = 0$ ,  $dU_z/dr = 0$ . To evaluate  $dU_r/dz$ , let us consider the region of the matrix adjacent to the "0" plane as shown in Fig. B3. Point A is displaced to point A', and point B to point B'. (B is a mirror image of A.) The displacements  $U_{AA'}$  and  $U_{BB'}$  are equal because of the symmetry and from the assumption that no voids are created. The displacement  $U_r$  varies as we go along the  $z$  axis and presents a continuous function of  $z$ . Since the function is continuous and sym-

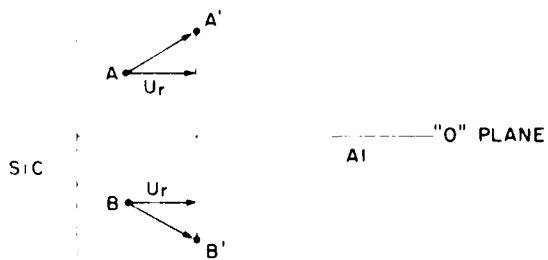


Fig. B3. Displacements AA' and BB' of the matrix symmetrical about the "0" plane.

metrical about the "0" plane, it goes through its local *maximum* or *minimum* point when it crosses the "0" plane and therefore  $dU_z/dz = 0$  when  $z = 0$ . Thus we found that, within the "0" plane, all the shear components of the strain tensor are equal to zero, which means that  $\epsilon_r = \epsilon_1$ ,  $\epsilon_\theta = \epsilon_2$  and  $\epsilon_z = \epsilon_3$  for the "0" plane. Thus, if we go back to the von Mises condition of yield, the effective strain  $\bar{\epsilon}$  can now be expressed as

$$\bar{\epsilon} = \frac{2^{1/2}}{3} \{(\epsilon_r - \epsilon_0)^2 + (\epsilon_\theta - \epsilon_0)^2 + (\epsilon_z - \epsilon_0)^2\}^{1/2}$$

and, from eqn. (B14),

$$\begin{aligned}\bar{\epsilon} &= \frac{2^{1/2}}{3} \left\{ \left( \frac{U_{\rho_0}}{\rho_0} \right)^2 + \left( \frac{2U_{\rho_0}}{\rho_0} \right)^2 + \left( \frac{U_{\rho_0}}{\rho_0} \right)^2 \right\}^{1/2} \\ &= 1.155 \frac{U_{\rho_0}}{\rho_0}\end{aligned}$$

However,

$$\begin{aligned}\bar{\epsilon} &= \epsilon_0 \\ &= 2 \times 10^{-4} \\ &= 1.155 \frac{U_{\rho_0}}{\rho_0}\end{aligned}$$

Therefore

$$\frac{U_{\rho_0}}{\rho_0} = 1.7 \times 10^{-4} \quad (\text{B15})$$

From eqn. (B11) we get

$$U_{\rho_0} = -\frac{M}{2} \frac{\rho_0}{\rho_0} + \frac{U_a a}{\rho_0} + \frac{Ma^2}{2\rho_0} - \frac{Na^3}{3\rho_0} + \frac{N}{3} \frac{\rho_0^2}{\rho_0^2}$$

and, substituting for  $M$  and  $N$ , we obtain

$$U_{\rho_0} = \frac{\Delta\alpha \Delta T}{\rho_0} \left\{ \frac{\rho_0^2 + a\rho_0 + a^2}{3} - \frac{(a + \rho_0)\rho_0}{2} + a^2 \right\} \quad (\text{B16})$$

Equations (B15) and (B16) can be solved as a system of two equations with two unknowns,  $U_{\rho_0}$  and  $\rho_0$ . Solving them, we obtain  $\rho_0 = 1.15$  mm. In order to find  $\rho_H$  we can follow the same procedure. However, for the "H" plane case the strains  $\epsilon_r$ ,  $\epsilon_\theta$  and  $\epsilon_z$  are not equal to  $\epsilon_1$ ,  $\epsilon_2$  and  $\epsilon_3$ . Therefore the procedure has to be modified. The new procedure would be to find an expression for

$$\gamma_{rz} = \frac{dU_z}{dr} + \frac{dU_r}{dz}$$

for  $z = \frac{1}{2}$  and then to solve the equation

$$\begin{bmatrix} \epsilon_r - \lambda & 0 & \gamma_{rz} \\ 0 & \epsilon_0 - \lambda & 0 \\ \gamma_{rz} & 0 & \epsilon_z - \lambda \end{bmatrix} = 0$$

This is a cubic equation. Three roots give the values for the principal strains:

$$\lambda_1 = \epsilon_1$$

$$\lambda_2 = \epsilon_2$$

and

$$\lambda_3 = \epsilon_3$$

This is simple in principle but very complex to implement for the following reason. The individual components of this tensor are of the type expressed by eqns. (B11) and (B15). If the coefficients of the cubic equation were numerical, then we could solve it using the trial-and-error method. In our case, all the coefficients have a general expression. The general solution of the cubic equation has the form

$$\lambda_1 = \left[ -\frac{q}{2} + \left\{ \left( \frac{q}{2} \right)^2 + \left( \frac{p}{3} \right)^3 \right\}^{1/2} \right]^{1/3} +$$

$$+ \left[ -\frac{q}{2} - \left\{ \left( \frac{q}{2} \right)^2 + \left( \frac{p}{3} \right)^3 \right\}^{1/2} \right]^{1/3}$$

Each  $q$  and  $p$  would be a combination of the expressions for  $\epsilon_r$ ,  $\epsilon_0$ ,  $\epsilon_z$  and  $\gamma_{rz}$ . Because of the difficulty of determining  $\rho_H$  in a rigorous way we can use an approximate solution by treating strains  $\epsilon_r$ ,  $\epsilon_0$  and  $\epsilon_z$  as the principal strains  $\epsilon_1$ ,  $\epsilon_2$  and  $\epsilon_3$ . This implies that we ignore the influence of the shear strain  $\gamma_{rz}$ . It is realized that the resulting value for  $\rho_H$  will not be a true value but it will at least give

an idea of the extent of the plastic zone on the surface of the sample. Additionally, if the magnitude of  $\gamma_{rz}$  is small, the deviation of  $\epsilon_r$ ,  $\epsilon_0$  and  $\epsilon_z$  from  $\epsilon_1$ ,  $\epsilon_2$  and  $\epsilon_3$  will also be small.

Now, considering  $z = \frac{1}{2}$  and using the yielding condition at the plastic-elastic front, we can follow steps similar to those that we used for the "0" plane. As a result  $\rho_H = 1.11$  mm. It is useful to find a general expression for  $\bar{\epsilon}$  in the "0" plane. After substitution of the numerical values for  $a$  and  $\rho$ , eqn. (B12) becomes, for  $z = 0$ ,

$$\epsilon_z = \frac{1.15 - r}{0.65} \Delta\alpha \Delta T$$

$$\epsilon_0 = \frac{0.513r^3 + 0.407 - 0.885r^2}{r^2} \Delta\alpha \Delta T$$

$$\epsilon_z = \frac{0.667r^3 - 0.575r^2 - 0.265}{0.65r^2} \Delta\alpha \Delta T$$

$$\bar{\epsilon} = 9.077 \times 10^{-3} \times$$

$$\times \left( 4.668r^2 - 10.35r + 5.952 - \frac{0.531}{r} - \frac{0.42}{r^4} \right)^{1/2}$$

This effective strain is plotted as a function of  $r$  in Fig. 5. When  $\bar{\epsilon} = \epsilon_0 = 2 \times 10^{-4}$  is substituted in the expression above, the theoretical plastic zone radius can be obtained from  $r = \rho = 1.15$  mm. The radius of the fiber is 0.5 mm. Thus  $\rho = 1.15/0.5 = 2.3 \times$  fiber radius. This radius includes the fiber size. Thus the extent of the plastic zone measured from the interface is  $(2.3 - 1) \times$  fiber radius =  $1.3 \times$  fiber radius.

THE EFFECTS OF DIFFERENCES IN THERMAL COEFFICIENTS OF  
EXPANSION IN SIC WHISKER 6061 ALUMINUM COMPOSITE\*

Richard J. Arsenault

Metallurgical Materials Laboratory  
University of Maryland  
College Park, MD 20742 USA

Minoru Taya  
Department of Mechanical and Aerospace Engineering  
University of Delaware  
Newark, DE 19716 USA

Summary

When a metal matrix composite is cooled down to room temperature from the fabrication or annealing temperature, residual stresses are induced in the composite due to the mismatch of the thermal expansion coefficients between the matrix and whisker.

An investigation was undertaken of the extent of the thermal residual stresses by an X-ray diffraction technique as well as of the difference of the yield stresses  $\Delta\sigma_y$  between tension and compression resulting from the thermal residual stresses. A theoretical model based on the Eshelby's method was then constructed for the prediction of the thermal residual stresses and  $\Delta\sigma_y$ . The agreement obtained was very good between the experimental results and the theoretical predictions.

Arsenault

\* This research was supported in part under a contract from the Office of Naval Research, Contract No. N00014-85K-0007.

## Introduction

Metal matrix composites (MMCs), including eutectic composites, are becoming important in their application to structural components which are to be used at intermediate and high temperatures. When MMCs are fabricated at high temperature or annealed at a certain high temperature and cooled down to room temperature, undesirable results, such as low tensile yield stress and strength of the MMC upon mechanical testing at room temperature, are produced. These results are mainly due to residual stresses that are caused by the mismatch of the thermal expansion coefficients between the matrix and fiber. This subject has been studied by a number of researchers (for examples see references 1-13). The residual stresses so induced have been observed in tungsten fiber/copper composites<sup>(7)</sup> and in SiC whisker/6061 Al composites<sup>(8,9)</sup>. Most of the models purposed to estimate the residual stress were based on one-dimensional analysis<sup>(1-3)</sup>, continuous fiber system<sup>(4,5)</sup>, or spherical particle system<sup>(10)</sup>.

The model based on Eshelby's equivalent inclusion method<sup>(7)</sup> has been used to solve the problem of thermal residual stress<sup>(12-14)</sup>. The advantages of the Eshelby's model are that it can solve a three-dimensional composite system such as short whisker composite and also can take into account the effect of the volume fraction of whisker ( $V_w$ ) easily.

Eshelby's method has been used also for predicting the yield stress and work-hardening rate of metal matrix composites<sup>(15-19)</sup>. The effect of the thermally induced residual stress on the yield stresses has been discussed by Wakashima et al.<sup>(18)</sup> who predicted that the yield stress in compression ( $\sigma_y^c$ ) exceeds that in tension ( $\sigma_y^t$ ) for continuous B fiber/Al composites which were cooled down, although no comparison with the experimental data was made.

In this paper we focus on the residual stresses induced in a short whisker MMC due to the temperature drop and its effect on the yield stresses. The target short whisker MMC is SiC whisker/6061 Al composite.

## Experimental Procedure

### Materials

The target short fiber MMC was SiC whisker/6061 Al composite and was purchased from ARCO/SILAG. The composite was in the form of an extruded rod 15.5 mm in diameter. Three different volume fractions of whisker ( $V_w$ ) were used:  $V_w = 0, 0.05$  and  $0.2$ . The composite was supplied as-fabricated (no heat treatment made), was machined into samples (Fig. 1a and 1b), annealed for 12 hours at 810 K, and then furnace cooled.

### Testing Methods

Tension and Compression Tests. The testing was performed in an Instron testing machine using a liquid metal container as the lower gripping device. This method of gripping was employed to ensure very good alignment of the sample. This test procedure is described in greater detail elsewhere<sup>(20)</sup>. Samples of two different gauge lengths were used to determine if there was a gauge length effect (there was none). The effective gauge length of the

samples was determined by glueing strain gauges on the center portion of the sample and comparing the results obtained from a clip on an extensometer which mounted into the "V" grooves. If the extensometer is mounted directly to the uniform gauge section, there is a high probability that the sample will fracture where the "knife" edge of the extensometer makes contact with the sample. Several tests in the low stress range were conducted using both the extensometer and the strain gauge; from these tests the effective gauge length was determined. Subsequent tests were conducted using only the extensometer. The samples, which were tested in the range from  $8 \times 10^{-5} \text{ sec}^{-1}$  to  $2 \times 10^{-3} \text{ sec}^{-1}$ , showed no effect on strain rate.

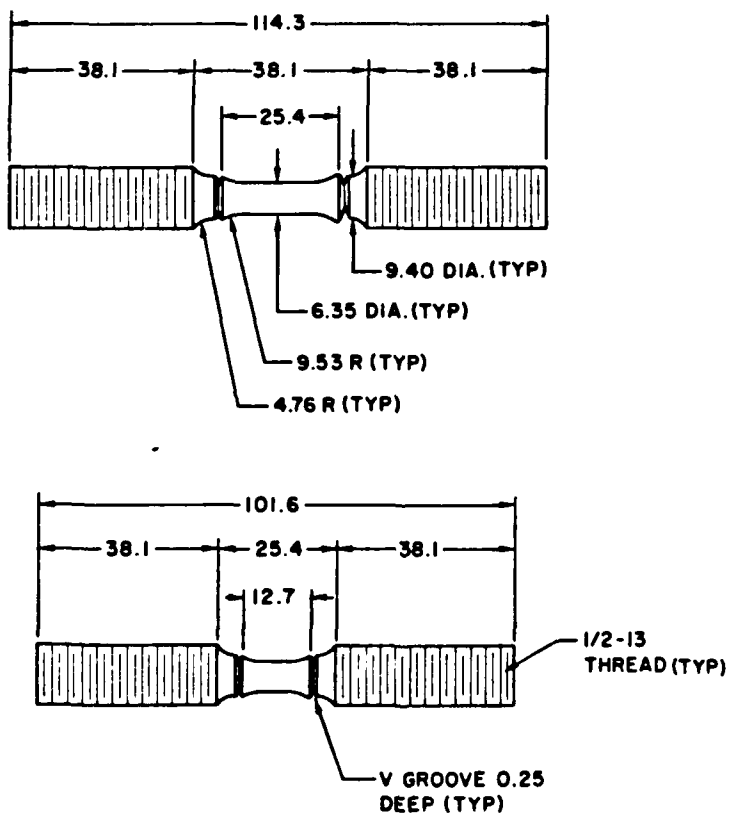


Figure 1 - A schematic diagram of the sample configuration which was used in the tension and compression testing. The dimensions are in millimeters.

Residual Stress Measurement by X-ray Diffraction. The X-ray diffraction technique was used to measure residual stress. Two components of the residual stress were focused on: the stress along the extrusion direction (longitudinal direction), which coincides with the whisker axis of a majority of whiskers ( $\sigma_L$ ), and the one in the transverse direction ( $\sigma_T$ ).

The data were obtained and reduced by standard techniques as outlined by Cohen et al. (21).

Arsenault

3

16

### Experimental Results

The stress-strain curves of  $V_w = 0$ , 0.05 and 0.2 composites are plotted in Fig. 2a, 2b, and 2c, respectively. The solid and dashed curves denote the tensile and compressive test results, respectively. The yield stress was measured as 0.2% off set strain and is indicated in the figures by arrows.

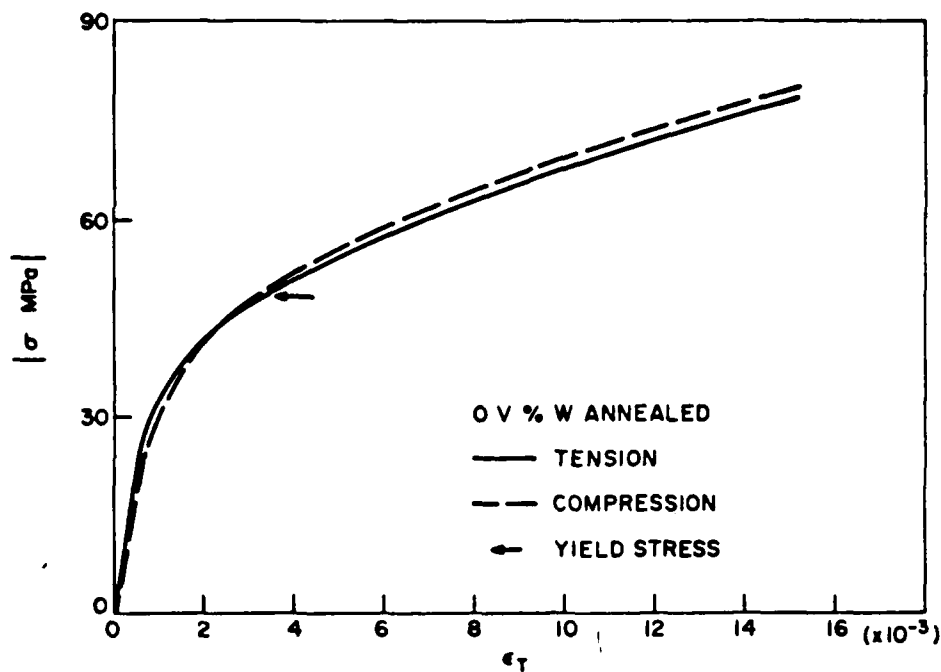
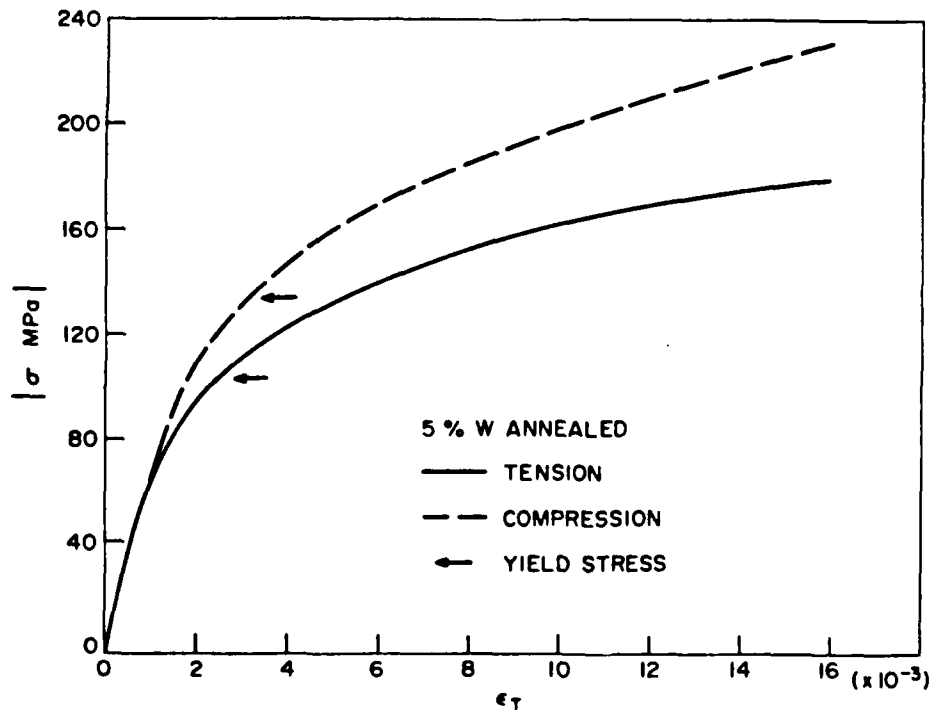


Figure 2a - The absolute stress vs. strain curves for tension and compression test of 0 volume % whisker material in the annealed condition.



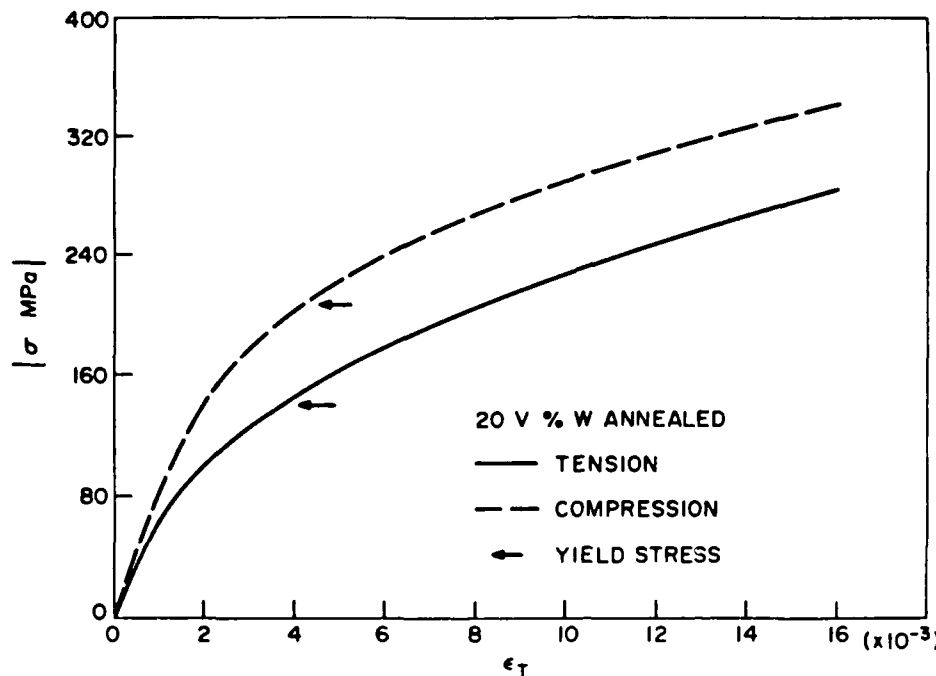


Figure 2c - The absolute value of the stress as a function of strain for 20 volume % whisker material in the annealed condition.

The residual stresses were measured by X-ray diffraction on three different values of  $V_w$  (0, 0.05, and 0.2) and are tabulated in Table 1 where the range of scattered data is also shown. It is noted that the values of  $\sigma_L$  and  $\sigma_T$  represent the volume average quantity in the matrix (6061 Al). It should also be noted that a compressive residual stress was found for all cases.

Table I  
Residual Stresses X-Ray Determination

Sample Designation $V_w$ %	Trans. $\sigma_T$ MPa	Long. $\sigma_L$ MPa
0	-37 to -44	-18 to -22
5	-17 to -41.4	-29 to -41.4
20	-49 to -57.3	-24 to -44.2

- compressive residual stress

#### Theoretical Procedure

The theoretical model used here is based on Eshelby's equivalent inclusion model. Mori and his co-workers<sup>(15-17)</sup> extended Eshelby's method to predict the yield stress ( $\sigma_y$ ) and work-hardening rate of aligned short whisker composites. Wakashima et al.<sup>(18)</sup> extended the above approach to predict  $\sigma_y$  by considering the mismatch of the thermal expansion coefficients of the matrix and fiber. Following the above models, Takao and Taya<sup>(14)</sup>

have recently computed the stress field in and around a short fiber in a short fiber composite where the fiber is anisotropic both in stiffness and thermal expansion.

In this paper we focus on the average thermal residual stress induced in the matrix by the cool-down process and also the yield stresses in tension ( $\sigma_y^t$ ) and compression ( $\sigma_y^c$ ) when the composite is tested at the room temperature. The former case is essentially based on the model by Takao and Taya<sup>(14)</sup>, and as the latter case, we extend the model by Wakashima et al.<sup>(18)</sup> to account for the bi-linear stress-strain curve of the matrix.

### Formulation

Consider an infinite body (D) which contains ellipsoidal whiskers ( $\Omega$ ) aligned along the  $x_3$ -axis (Fig. 3). This composite body D is subjected to the applied stress field  $\sigma_{ij}^0$ . The stiffness tensors of the matrix (D- $\Omega$ ) and whisker ( $\Omega$ ) are denoted by  $C_{ijkl}$  and  $C_{ijkl}^W$ , respectively. Following Eshelby, the transformation strain<sup>(11)</sup> or eigenstrain<sup>(22)</sup> is given in the fiber domain  $\Omega$  as

$\alpha_{ij}^*$ , where  $\alpha_{ij}^*$  is the strain due to the mismatch of the thermal expansion coefficients and the uniform plastic

strain  $e_{ij}^P$  is prescribed in the matrix<sup>(15)</sup>. As far as the stress field is concerned, the model of Fig. 4 is equivalent to that of Fig. 3. Thus, the present problem is reduced to "inhomogeneous inclusions problem" (Fig. 4)<sup>(22)</sup>. The model of Fig. 4 will be used not only to predict the yield stresses and work-hardening rate, but also to compute the thermal residual stress. For in the latter case, we will set

$$\sigma_{ij}^0 = e_{ij}^P = 0.$$

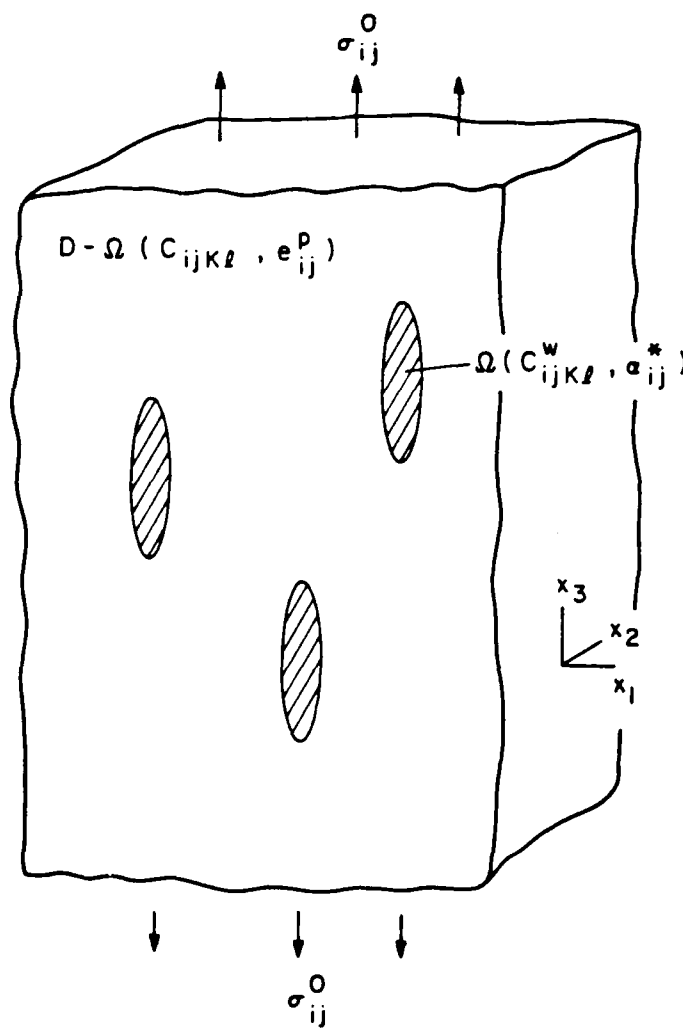


Figure 3 - Theoretical model; actual case

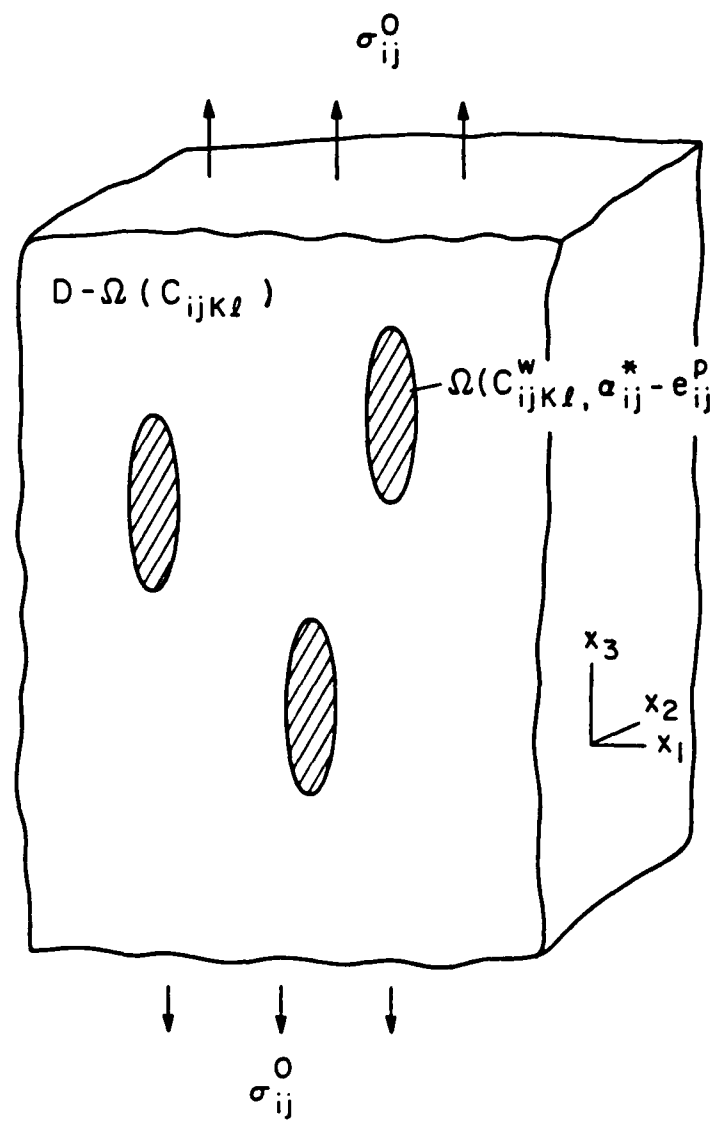


Figure 4 - The equivalent inclusion model converted from Figure 3.

Following the Eshelby's equivalent inclusion method modified for a finite volume fraction of whiskers<sup>(22,23)</sup>, the total stress field in the fibers  $\sigma_{ij}^0 + \sigma_{ij}$  is given by

$$\begin{aligned} \sigma_{ij}^0 + \sigma_{ij} &= C_{ijkl}^W \{ e_{kl}^0 + \tilde{e}_{kl} + e_{kl} - (\alpha_{kl}^* - e_{kl}^p) \} \\ &= C_{ijkl} \{ e_{kl}^0 + \tilde{e}_{kl} + e_{kl} - (\alpha_{kl}^* - e_{kl}^p) - e_{kl}^* \} \end{aligned} \quad (1)$$

where

$$\sigma_{ij}^0 = C_{ijkl} e_{kl}^0 \quad \text{in } D \quad (2)$$

$$\langle \sigma_{ij} \rangle_m = C_{ijkl} \tilde{e}_{kl} \quad \text{in } D-\Omega \quad (3)$$

In Eq. (1),  $e_{ke}^*$  is the fictitious eigenstrain<sup>(22)</sup> which was introduced to connect the present problem to "inclusion problem" and  $\tilde{e}_{ij}$  is the average strain disturbance in the matrix and related to the average stress disturbance in the matrix  $\langle \sigma_{ij} \rangle_m$  by Eq. (3).  $\langle \sigma_{ij} \rangle_m$  is defined by

$$\langle \sigma_{ij} \rangle_m = \frac{1}{V_{D-\Omega}} \int_{D-\Omega} \sigma_{ij} dv \quad (4)$$

where  $V_{D-\Omega}$  is the total volume of the matrix and  $\sigma_{ij}$ , and  $e_{ij}$  in Eqs. (1) and (4) is the stress and strain disturbance, respectively, by a single fiber  $\Omega$  when it is embedded in an infinite matrix. Since the stress disturbance when it is integrated in the entire domain  $D$  vanishes,

$$\int_D \sigma_{ij} dv = 0 \quad (5)$$

The stress disturbance  $\sigma_{ij}$  is obtained from Eqs. (1) and (2)

$$\sigma_{ij} = C_{ijkl} (\tilde{e}_{kl} + e_{kl}^* - e_{kl}^{**}) \quad (6)$$

where

$$e_{kl}^{**} = e_{kl}^* + e_{kl}^* - e_{kl}^p \quad (7)$$

From Eqs. (3), (5) and (6), we obtain

$$\tilde{e}_{ij} = - V_w (e_{ij}^* - e_{ij}^{**}) \quad (8)$$

According to Eshelby,  $e_{ij}$  is related to the total eigenstrain  $e_{kl}^{**}$  as

$$e_{ij} = S_{ijkl} e_{kl}^{**} \quad (9)$$

where  $S_{ijke}$  is the Eshelby's tensor and a function of  $C_{ijkl}$ ,  $C_{ijkl}^w$  and the geometry of the ellipsoidal whisker<sup>(22)</sup>. The fiber is assumed as a prolate spheroid, hence the whisker aspect ratio  $l/d$  is a single geometrical parameter. For simplicity, we assume that the matrix and fiber are isotropic both in stiffness and thermal expansion coefficient. Thus,  $C_{ijkl}$ ,  $C_{ijkl}^w$  and  $\alpha_{ij}^*$  are given by

$$C_{ijkl} = \lambda \delta_{ij} \delta_{kl} + \mu (\delta_{ik} \delta_{jl} + \delta_{il} \delta_{kj}) \quad (10)$$

$$C_{ijkl}^w = \lambda^w \delta_{ij} \delta_{kl} + \mu^w (\delta_{ik} \delta_{jl} + \delta_{il} \delta_{kj}) \quad (11)$$

$$\alpha_{ij}^* = - (\alpha_w - \alpha) \delta_{ij} \Delta T \quad (12)$$

In the above equations,  $\delta_{ij}$  is the Kronecker's delta,  $\lambda$  ( $\lambda^w$ ) and  $\mu$  ( $\mu^w$ ) are Lame's constants of the matrix (whisker),  $\alpha$  ( $\alpha_w$ ) is the thermal expansion coefficient of the matrix (fiber) and  $\Delta T$  is the change in temperature ( $\Delta T > 0$  corresponds to the temperature drop).

The stress field in the fiber is obtained from Eqs. (6), (8), (9) and (10)

$$\sigma_{ij} = (1 - v_w) \{ (S_{kkmn} e_{mn}^{**} - e_{kk}^{**}) \lambda \delta_{ij} + 2\mu (S_{ijmn} e_{mn}^{**} - e_{ij}^{**}) \} \quad (13)$$

After solving for  $e_{ij}^{**}$  in Eq. (1) by use of Eqs. (8) and (9), we can compute the stress disturbance  $\sigma_{ij}$  in the whisker from Eq. (13).

### Yield Stresses $\sigma_y^t$ , $\sigma_y^c$ and Work-Hardening Rate

The method of computing the yield stresses  $\sigma_y^t$  and  $\sigma_y^c$  and the work-hardening rate of the composite is described briefly. The total potential energy of Fig. 3,  $U$ , is given by

$$U = \frac{1}{2} \int_D (\sigma_{ij}^0 + \sigma_{ij}) (u_{ij}^0 + \tilde{u}_{ij} + u_{ij} - e_{ij}^p - \alpha_{ij}^*) dV - \int_{|D|} \sigma_{ij}^0 n_j (u_i^0 + \tilde{u}_i + u_i) ds \quad (14)$$

where  $u_i^0$ ,  $\tilde{u}_i$  and  $u_i$  are the displacement components corresponding to  $e_{ij}^0$ ,  $\tilde{e}_{ij}$  and  $e_{ij}$ , respectively; the index  $j$  preceded by a comma denotes a partial differentiation with respect to  $x_j$ ;  $|D|$  is the boundary of  $D$ ; and  $n_j$  is the  $j$ -th component of an unit vector outer normal to  $|D|$ . Then, the change in  $u$  due to the change in the plastic strain  $\delta e_{ij}^p$  is given by

$$\delta U = - \int_D (\sigma_{ij}^0 + \sigma_{ij}) \delta e_{ij}^p dV \quad (15)$$

In the above deviation, the Gauss' divergence theory and the following equation were used

$$\int_D \sigma_{ij} (\delta \tilde{u}_{ij} + \delta u_{ij}) dV = 0$$

Noting that the plastic strain exists only in the matrix ( $D - \Omega$ ), Eq. (15) is reduced to

$$\delta U = - \delta e_{ij}^p \{ (1 - v_w) \sigma_{ij}^0 - v_w \sigma_{ij} \} \quad (16)$$

Under the uniaxial stress along the  $x_3$ -axis ( $\sigma_0^0$ ),  $\sigma_{ij}^0$  and  $e_{ij}^p$  are given by

$$\sigma_{ij}^0 = \begin{matrix} 0 & -1/2 e_p \\ 0 & -1/2 e_p \\ \sigma_0 & e_p \\ 0 & 0 \\ 0 & 0 \\ 0 & 0 \end{matrix} \quad (17)$$

where the six components of  $\sigma_{ij}^0$  and  $e_{ij}^p$  are expressed in the order of  $(ij) = 11, 22, 33, 23, 31$ , and  $12$ , and  $e_p$  is the plastic strain along the  $x_3$ -axis. On the other hand, the energy dissipation due to the plastic work in the matrix,  $\delta Q$ , is given by

$$\delta Q = (1 - v_w) \sigma_y^t \delta e_p \quad (18)$$

where  $\sigma_y$  is the flow stress of the matrix for the bilinear model

$$\sigma_y = \sigma_y^0 + E_T(e - e_p) \quad (19)$$

where  $\sigma_y^0$  and  $E_T$  are the initial yield stress and tangent, modulus of the matrix, respectively, and  $e$  is the total strain. Since  $\delta U + \delta \Omega = 0$ , we obtain

$$\sigma_0 = \sigma_y + \frac{v}{(1-v)} \frac{w}{w} (\sigma_{33} - \sigma_{11}) \quad (20)$$

In the above deviation,  $\sigma_{11} - \sigma_{22}$ ,  $e_{11}^p = e_{22}^p = -\frac{1}{2} e_p$  were used. Combining the solutions of  $\sigma_{ij}$  in Eq. (13) and Eq. (20), we can obtain the yield stress of the composite in tension ( $\sigma_y^t = \sigma_0$ ) and that in compression ( $\sigma_y^c = \sigma_0$ ) as

$$\sigma_y^t / \sigma_y^0 = C_0 + C_1 \alpha_m \Delta T \quad (21)$$

$$\sigma_y^c / \sigma_y^0 = C_0 - C_1 \alpha_m \Delta T$$

Similarly, the work-hardening rate of the composite,  $\bar{E}_T$  is obtained as

$$\bar{E}_T / E_T = C_2 + C_3 \left( \frac{E}{E} \right) \quad (22)$$

In the above equations,  $C_0$ ,  $C_1$ ,  $C_2$ , and  $C_3$  are functions of the mechanical properties of the matrix and whisker and the fiber aspect  $l/d$ ,  $E$  is the Young's modulus of the matrix.

### Thermal Residual Stress

When the composite is cooled down by  $\Delta T$ , the thermal residual stress is induced in the composite. The theoretical model for this problem is the same as that shown in Fig. 4 except that  $\sigma_{ij}^0 = e_{ij}^p = 0$  in the present case. Hence, the formulation up to Eq. (13) is valid and will be used to compute the thermal residual stress. Once the stress within the whisker  $\sigma_{ij}^{(in)}$  is computed, the stresses just outside the whisker  $\sigma_{ij}^{(out)}$  can be obtained by the following relation (13)

$$\sigma_{pq}^{(out)} = \sigma_{pq}^{(in)} + C_{pqmn} \left\{ - C_{klij} e_{ij}^{**} n_l n_m \frac{(\lambda+2\mu)\delta_{km} - (\lambda+\mu)n_k n_m}{\mu(\lambda+2\mu)} + e_{mn}^{**} \right\} \quad (23)$$

where  $\sigma_{pq}^{(in)}$  is given by Eq. (13),  $e_{ij}^{**}$  is solved by Eq. (1),  $\lambda$  and  $\mu$  are previously defined and  $n_i$  is the  $i$ -th component of the unit vector perpendicular to the surface of the whisker. If one wants to compute the stresses just outside the equator of the ellipsoidal whisker where  $n = (1, 0, 0)$ , we can obtain the stresses in polar coordinates,  $\sigma_r$ ,  $\sigma_\theta$  and  $\sigma_z$  there as

$$\begin{aligned}
 \sigma_r^{(out)} &= \sigma_r^{(in)} \\
 \sigma_\theta^{(out)} &= \sigma_\theta^{(in)} + 2\mu \left\{ \frac{1}{1-\nu} e_{11}^{**} + \frac{\nu}{1-\nu} e_{33}^{**} \right\} \\
 \sigma_z^{(out)} &= \sigma_z^{(in)} + 2\mu \left\{ \frac{\nu}{1-\nu} e_{11}^{**} + \frac{1}{1-\nu} e_{33}^{**} \right\}
 \end{aligned} \tag{24}$$

where  $\nu$  is the Poisson's ratio of the matrix.

Next the average stress field in the matrix,  $\langle \sigma_{ij} \rangle_m$ , can be also obtained from Eqs. (3), (8) and (9) as

$$\langle \sigma_{ij} \rangle_m = -v_w C_{ijkl} (S_{klmn} e_{mn}^{**} - e_{kl}^{**}) \tag{25}$$

The average stress in the matrix,  $\langle \sigma_r \rangle_m$ ,  $\langle \sigma_\theta \rangle_m$  and  $\langle \sigma_z \rangle_m$ , will be computed by setting  $ij = 11, 22$ , and  $33$  in Eq. (25). It should be noted here that  $\langle \sigma_r \rangle_m = \langle \sigma_\theta \rangle_m$  due to the assumptions of an aligned short whisker composite which results in the transverse isotropy of the volume average quantity.

### Theoretical Results

The thermo-mechanical data of the matrix and whisker for the theoretical calculations are obtained from the stress-strain curve of the matrix (Fig. 2a) and the material properties handbook.

Annealed 6061 Al matrix (bilinear model):

$$\begin{aligned}
 E &= 47.5 \text{ GPa} \\
 E_T &= 2.3 \text{ GPa} \\
 \sigma_y^0 &= 47.5 \text{ MPa} \\
 \nu &= 0.33 \\
 \alpha &= 23.6 \times 10^{-6}/^\circ\text{C}
 \end{aligned} \tag{26}$$

SiC Whisker:

$$\begin{aligned}
 E_w &= 427 \text{ GPa} \\
 \nu_w &= 0.17 \\
 \alpha_w &= 4.3 \times 10^{-6}/^\circ\text{C} \\
 l/d &= 1.8
 \end{aligned} \tag{27}$$

where the average value of the fiber aspect ratio ( $l/d$ ) was used<sup>(24)</sup> and the bilinear stress strain curve of the matrix is indicated by a dash-dot line in Fig. 2a. The temperature drop  $\Delta T$  is defined as

$$\Delta T = T_1 - T_0 \tag{28}$$

where  $T_1$  is taken as the temperature below which dislocation generation is minimal during the cooling process<sup>(9)</sup> and  $T_0$  is the room temperature. Thus, for the present composite system  $\Delta T$  is set equal to 200 K.

The theoretically predicted  $\sigma_y^c$  and  $\sigma_y^t$  can be obtained from Eq. (21). The differences between  $\sigma_y^c$  and  $\sigma_y^t$  ( $\sigma_y^c - \sigma_y^t$ ) for various  $v_w$  are shown as the solid line in Fig. 5. The differences between  $\sigma_y^c$  and  $\sigma_y^t$  increase with increasing  $v_w$ . The experimentally determined differences between  $\sigma_y^c$  and  $\sigma_y^t$  are represented by the open circles in Fig. 5. The experimental values of the yield stresses are taken as the stresses 0.2% off-set strain. It follows (Fig. 5) that good agreement is obtained between the experimental

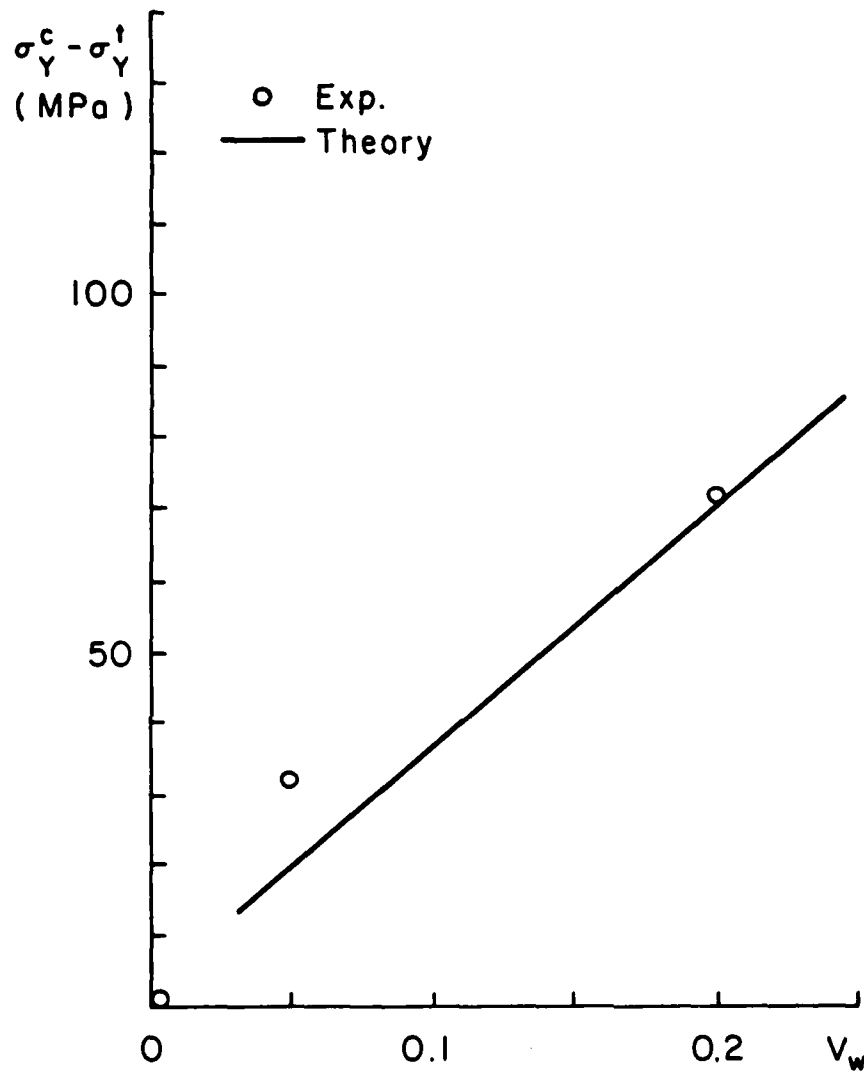


Figure 5 - The difference in yield stress between compression and tensin as a function of volume % silicon carbide whisker.

and theoretical results of the difference in the compressive tensile yield stresses. However, the experimental values of  $\sigma_y^c$  are greater than the theoretical values of  $\sigma_y^c$ , and similarly the experimental values of  $\sigma_y^t$  are greater than the theoretical values of  $\sigma_y^t$ .

From the data given by Eqs. (26) - (27) and the use of Eq. (25), we have computed the average stresses in the matrix and the stresses just outside the fiber and plotted schematically the  $\sigma_L$  and  $\langle \sigma_L \rangle_m$  along the x (or  $x_2$ ) and  $x_3$  axes in Fig. 6.

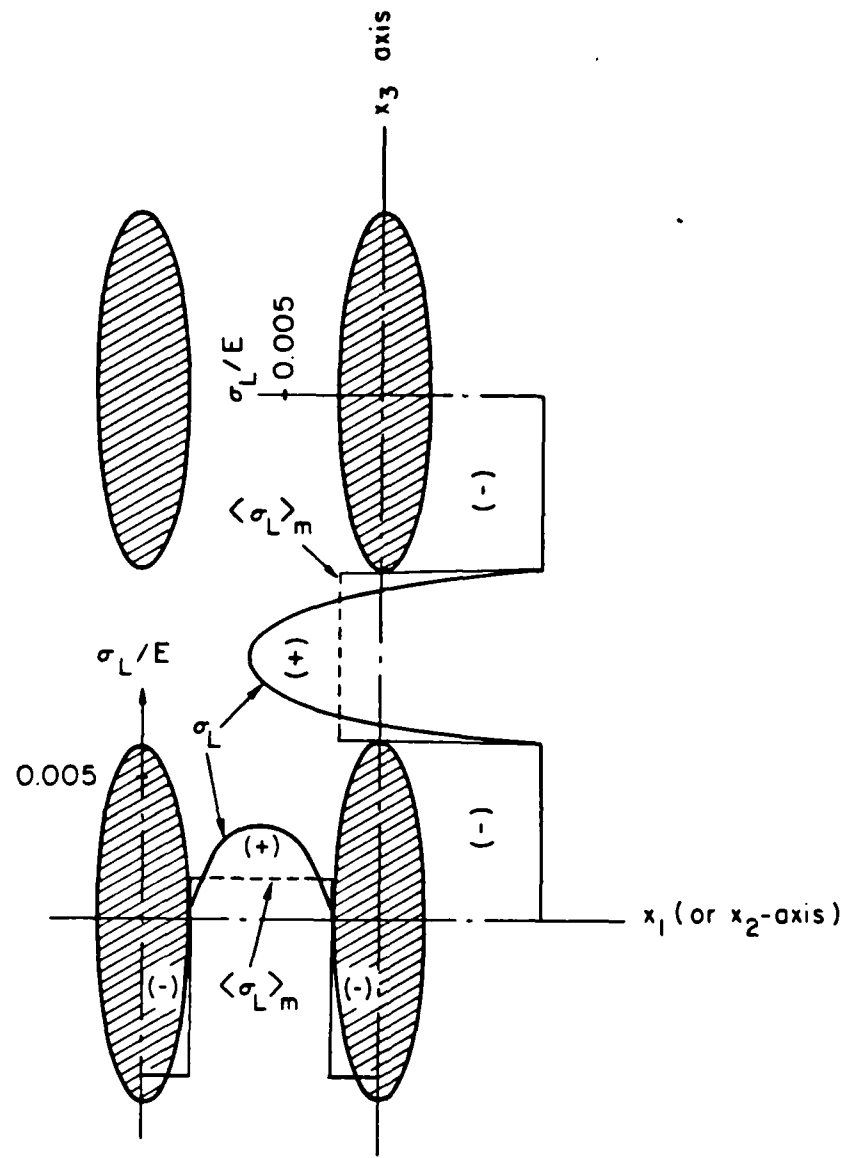


Figure 6 - Is a schematic of the stress distribution in the matrix and in the reinforcement due to the difference in thermal coefficient of expansion between the silicon-carbide and aluminum.

Next, the thermal residual stresses averaged in the matrix of the SiC whisker/6061 Al are predicted by Eq. (25) and the results on  $\langle\sigma_T\rangle_m$  and

$\langle\sigma_L\rangle_m$  are plotted in Fig. 7 as a function of the volume fraction of whisker ( $V_w$ ), where the subscripts, T and L denote the component along the transverse direction (r and θ) and longitudinal direction (z). The average theoretical thermal-residual stress is predicted to be tensile in nature.

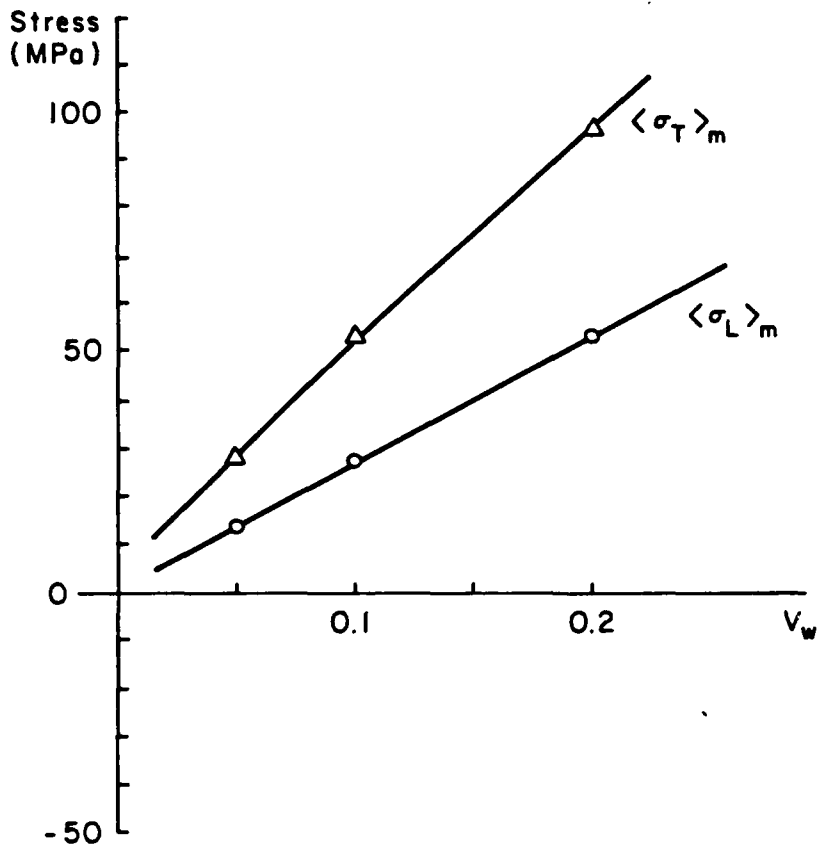


Figure 7 - Predicted residual stress in the matrix for the transverse and longitudinal directions.

#### Discussion and Conclusions

The theoretical predictions and experimental results are in very good agreement in most cases, and in some cases the differences are to be expected.

The theoretical model is based on an extension of previous work by Eshelby (11), Mura and Taya (13), and Tanaka and Mori (15), and it can predict the yield stress in tension and compression and the thermal residual stress. The predicted values of the yield stress in tension and compression are less than the experimentally determined values of the yield stress in tensional compression. This difference between the theoretical and experimental stresses is due to the fact that the  $V_w = 0$  curves of stress vs. strain were used for the matrix in the composite cases. It has been demonstrated by Arsenault and Fisher (8) and Vogelsang, et al. (9) that there is a much higher dislocation density in the annealed composite matrix than in the  $V_w = 0$  material. Therefore, the matrix is stronger than the annealed  $V_w = 0$  matrix alloy. However, this increase in matrix strength due to a higher dislo-

tion density does not influence the difference in yield stress in the compression vs. tension. The theoretical prediction is that the yield stress in compression should be higher than the yield stress in tension, and this is exactly what is observed experimentally.

The theoretical prediction that the compressive yield stress is higher than the tensile yield stress suggests that a tensile residual stress exists in the matrix of composite. An average tensile residual stress is predicted in the matrix as shown in Figs. 6 and 7. However, the experimentally determined residual stress is compressive, i.e., opposite of the prediction. This difference can qualitatively be explained in terms of the magnitude of the tensile and compressive residual stresses in the matrix. If the compressive regions of the matrix were eliminated and only the tensile regions were examined, then there would be no change in the diffraction peak conditions, because the limit of detection is  $\sim 50$  MPa. If a similar experiment were conducted, but in this case only the compressive regions were kept then there would be a change in peak position because the compressive residual stress is greater than the detection limit. Now, if both tensile and compressive regions are combined, the net result, a small compressive residual, will be experimentally detected, which is in agreement with the X-ray residual stress measurements.

It is possible to arrive at the following conclusions from the theoretical model and the experimental results.

1. The theoretical model predicts a higher compression yield stress than tensile yield stress, which is in agreement with the experimental results.
2. The absolute magnitude of the predicted yield stress (tensile and compressive) is less than the experimental yield stress due to an increase in matrix strengthening. The increased matrix strength is due to a higher dislocation density in the matrix; the higher dislocation density is a consequence of the difference in coefficient of thermal expansion between the Al alloy matrix and the SiC.
3. The magnitude of the average residual stress is small, but at the SiC-Al alloy interface there can be a large compressive stress.
4. The residual stress, in the region between SiC whiskers, is tensile and this is the likely region where plastic deformation would begin. For in this region the matrix contains a lower dislocation density than adjacent to the SiC whisker, i.e., in this region the matrix is weaker.

#### References

1. E. R. Thompson, D. A. Koss, and J. C. Chestnutt, Metall. Trans. 1 (1970), p. 2807.
2. D. A. Koss and S. M. Copley, Metall. Trans. 2 (1971), p. 1557.
3. J. K. Lees, Polymer Eng. Sci. 8 (1968), p. 195.
4. S. S. Hecker, C. H. Hamilton and L. J. Ebert, J. Mater. Sci. 5 (1970), p. 868.
5. J. Gayda and L. J. Ebert, Metall. Trans. 10A (1979), p. 349.
6. S. D. Tsai, D. Mahulikar, H. L. Marcus, I. C. Noyan and J. B. Cohen, Mater. Sci. & Eng. 47 (1981), p. 145.
7. K. K. Chawla and M. Metzger, J. Mater. Sci. 7 (1972), p. 34.
8. R. J. Arsenault and R. M. Fisher, Scripta Metall. 17 (1983), p. 67.

9. M. Vogelsang, R. J. Arsenault, and R. M. Fisher, submitted for publication.
10. J. K. Lee, Y. Y. Earmme, H. I. Aaronson and K. C. Russell, Metall. Trans. 11A (1980), p. 1837.
11. J. D. Eshelby, Proc. Roy. Soc. London A241 (1957), p. 376.
12. K. Wakashima, M. Otsuka and S. Umekawa, J. Comp. Mater. 8 (1976), p. 391.
13. T. Mura and M. Taya, Proc. of the 2nd U.S.-Japan Conf. on Comp. Mater. ASTM, under review.
14. Y. Takao and M. Taya, J. Appl. Mech., under review.
15. K. Tanaka and T. Mori, Acta Metall. 18 (1970), p. 931.
16. K. Tanaka, K. Wakashima and T. Mori, J. Mech. Phys. Solids 21 (1973), p. 207.
17. S. C. Lin, T. Mura, M. Shibata and T. Mori, Acta Metall. 21 (1973), p. 505.
18. K. Wakashima, S. Kurihara and S. Umekawa, Japan Soc. Comp. Mater. 2 (1976), p. 1.
19. A. Daimaru and M. Taya, Proc. of the 4th Intl. Conf. on Comp. Materials, Edited by Hayashi et al., Japan Soc. Comp. Materials, Tokyo (1982), p. 199.
20. R. Hsu and R. J. Arsenault, Mat. Sci. & Eng. 66 (1984), p. 35.
21. J. B. Cohen and L. Schwartz, Diffraction Methods in Materials Science, MacMillan.
22. T. Mura, Micromechanics of Defects in Solids, Martinus Nijhoff Publishers, 1982.
23. T. Mori and K. Tanaka, Acta Metall. 21 (1973), p. 571.
24. R. J. Arsenault, Mater. Sci. & Eng., 64 (1984), p. 171.

INTERFACIAL BOND STRENGTH IN A  
6061 Al/SiC COMPOSITE\*

by

Y. Flom and R. J. Arsenault

Metallurgical Materials Laboratory  
University of Maryland  
College Park, MD 20742

Materials Science and Engineering,  
Vol. 77, 1986, p. 191.

\* This research was supported through a grant from the Office of Naval Research N00014-85K-0007.

### Abstract

An investigation was undertaken to evaluate the strength of the interfacial bond between SiC and the 6061 Al alloy matrix. Approximate bounding analysis provided the conditions for separation of the inclusion from the ductile matrix under the local negative pressure (triaxial tensile stress). The experimental data was analyzed to determine the local interfacial stresses at the particle-matrix interfaces. The lower bound value of the bond strength was determined to be equal to at least 1690 MPa. Debonding of SiC particulates from the matrix was found to be a rare event.

### Introduction

The quality of interfacial bond between Al and SiC is important in composite strengthening, independent of the strengthening mechanism that is assumed to be operative. One of the key elements in the continuum mechanics treatment of the composite strengthening is that the interface transfers the load from the matrix into the reinforcement<sup>[1-3]</sup>. The rule of mixtures that emerges from the continuum mechanics relates a given property of the composite to the properties of its constituent materials. The credibility of this approach depends on, among other things, the bond integrity and the efficiency of the load transfer from the matrix to the reinforcement.

Recently it has been shown[4-6] that in Al/SiC systems the interfaces are a major source of the dislocation generation (on cooling from fabricating temperature due to the difference in the coefficient of thermal expansion). The resultant dislocation densities at the Al/SiC interfaces can be very high ( $10^9$  to  $10^{10}$   $\text{cm}^{-2}$ ), which significantly contributes to the overall composite strength. Interestingly, when an Al/SiC system is subject to heating, the Al/SiC interface also generates dislocations (providing that Al/SiC bond is quite strong)[7]. If the bond is weak, the Al just pulls away from the particle and is free to expand without any restrictions on the part of the SiC, and in the subsequent cooling no dislocations are generated. Therefore, a good bond is required to produce the high dislocation density.

Several investigators have reported that the bond between Al/SiC is generally good[8,9], but a systematic evaluation of the bond strength has not been, to our knowledge, reported in the literature. Direct measurements of the interfacial shear strength in metal matrix systems have been made using flat plate and fiber pullout tests[10]. The fiber pullout test, which is of more interest for this investigation, was used to determine interfacial shear strength in Cu/W and Cu/Mo systems[11]. Several attempts were made to carry out a direct measurement of the interfacial bond shear strength in Al/SiC using the pullout test due to its apparent simplicity. However, all these attempts resulted in brittle failure of SiC (single crystal, very large grain, and sintered SiC were used) at very moderate loads.

In addition, an effort was made to perform a punch test using Al disks with pieces of the SiC embedded in the center. This effort also resulted in premature failure of the SiC.

Another way to evaluate the interfacial bond strength is based on the general understanding of the mechanism of the ductile fracture[12-15] and was applied for the determination of the interfacial bond strength in spheroidized 1045 steel, Cu-0.6 pct. Cr alloy, and maraging steel containing Fe<sub>3</sub>C, Cu-Cr and TiC particles, respectively[16,17]. Providing that the ductile fracture starts by void nucleation at the inclusions and second phase particles, the theoretical bounding analysis[15] allows the evaluation of the interfacial strength in the systems with the small volume fraction of the second phase.

The purpose of this investigation was to experimentally determine the bond strength between SiC and Al in a commercial composite material using the analysis of separation of the inclusion from the matrix under the negative pressure.

#### Experimental Procedure

One volume percent (1V%) SiC particulate in a 6061 Al alloy matrix composite purchased from DWA was used for this investigation. The low volume percent of the particulate was necessary in order to: 1) provide favorable conditions for a ductile fracture and thus activate the mechanism of void nucleation and growth type failure, 2) satisfy criteria of non-interacting particles[17]. At higher volume concentrations, the Al/SiC

composites exhibited very little ductility. The theoretical analysis of the inclusion separation from the matrix that was used in this investigation was based on the assumption that there is no interaction between the particles, which is a reasonable statement for a small-volume concentration.

The composite material was machined to a standard tensile test specimens. In order to introduce a local triaxial stress state, a circumferential groove was electrical discharge machined (EDM) in the center of the specimen (Fig. 1). Subsequently, the specimen were solution-annealed at 823 K for 12 hours and ice water quenched in order to keep the  $Mg_2Si$  phase in the solution and thus limit the presence of particles other than SiC. After quenching, the samples were placed into the freezer of a commercial refrigerator where they were stored at 265 K and within a few minutes the samples were able to warm up to the testing temperature of 295 K. The specimens were tested in tension to fracture using the Instron testing machine at cross-head velocity of  $0.05 \frac{cm}{min}$ . The fractured halves were EDM, cut longitudinally (parallel to the tensile axis), and mechanically polished. Final polishing was done using a colloidal silica suspension as abrasive (Buehler's Mastermet) on the special moderate length nap cloth (Buehler's Mastertex). Since this suspension has a slightly alkali reaction, the final polishing was accomplished both mechanically and chemically. Therefore, the surface was ready for inspection without the necessity of etching to delineate the SiC particulates. Polished sections were examined for voids and particles separation using the

scanning electron microscope (SEM).

### Experimental Results and Discussion

The experimental technique adopted in this work was based on the determination of local stresses during plastic deformation under a triaxial stress state<sup>[16]</sup>. The bonding analysis<sup>[16]</sup> showed that the interfacial stress  $\sigma_{rr}$  can be expressed as

$$\sigma_{rr} = \sigma_T + Y(\bar{e}^p) \quad (1)$$

where  $\sigma_T$  is the local negative pressure (triaxial tensile stress),  $Y(\bar{e}^p)$  is true flow stress in tension corresponding to the local average plastic strain, had the second phase particle been absent. This analysis was based on the assumption that: (1) particles have an equiaxed shape, and (2) volume fraction of the second phase is small. Also, it can be mentioned that SiC is rigid and undeformed. This physical property agrees very well with the assumption of rigidity of the inclusions<sup>[16]</sup>.

The distribution of the triaxial tensile stress along the radial line in the plane of the groove was obtained from the theory of stress concentrations on circumferentially grooved elastic bars originally considered by Neuber and then expressed<sup>[16]</sup> as:

$$\frac{\sigma_T}{\sigma_0} = \frac{c}{\sqrt{1 - \left(\frac{r}{a}\right)^2}} \quad (z = 0) \quad (2)$$

where  $\frac{\sigma_T}{\sigma_0}$  represents the triaxiality,  $\sigma_T$  is the negative pressure,  $\sigma_0$  is the flow stress or average ligament stress,  $z$  is equal to the vertical distance along the  $z$  axis, i.e., tensile axis center line of sample, and  $r$  is the distance from the  $z$  axis. Since triaxiality  $\sigma_T/\sigma_0$  reaches its maximum value at the bottom of the groove,  $r$  should be equal to  $\underline{a}$ , where  $2a$  is the diameter of the ligament (see Fig. 1). Parameters  $c$  and  $\bar{a}$  are defined as follows:

$$c = \frac{1 + \frac{a}{R} + \sqrt{1 + \frac{a}{R}}}{2(2 + \frac{a}{R} + \sqrt{1 + \frac{a}{R}})} \quad (3)$$

$$\bar{a} = \frac{a \sqrt{1 + \frac{a}{R}}}{\sqrt{\frac{a}{R}}} \quad (4)$$

where  $a$  is the radius of the ligament and  $R$  is the radius of the groove (see Fig. 1b). The longitudinal sections of the tested specimen are shown on Fig. 2. In general, the number of voids associated with debonding of SiC particulates was much smaller than the total number of voids related to the fracture. Several examples of the areas where debonded SiC particulates can be observed are shown in Fig. 3. Debonding shown in Fig. 3 is a rather rare event and is not typical of Al/SiCp fractured samples[18].

According to the Neuber analysis, the largest negative pressure occurs at the outer surface of the groove (see Fig. 1). Since, in general, no separation between the SiC particulates and Al matrix was observed, it is reasonable to assume

that for Al/SiC bond:

$$\sigma_{rr} > \sigma_T^{\max} + Y(\bar{e}^p)$$

value of  $Y(\bar{e}^p)$  was obtained from stress-strain curve as

$$Y(\bar{e}^p) = \frac{P_f}{A_f} = \sigma_0 = \text{flow stress} \quad (5)$$

where  $P_f$  will equal the load at failure which will equal 750 kg and  $A_f$  will equal the area across the grooved region. The values of  $c$  and  $\bar{a}$  we get from expressions (3) and (4), respectively. At the bottom of the circumferential grove ( $z = 0$ ) these values are  $c = 0.48$  and  $\bar{a} = 2.3$  mm.

Substituting Eqs. (5) and (2) into Eq. (1) we obtain:

$$\sigma_{rr} = \sigma_0 \frac{c}{\sqrt{1 - (\frac{r}{\bar{a}})^2}} + \sigma_0 \approx 1690 \text{ MPa}$$

Thus, the lower bound value for Al/SiC bond strength is 1690 MPa: the Neuber analysis is applicable to a linear solid, i.e., to a material with linear strain hardening. From the stress-strain curves obtained, it was felt that the behavior of the tested specimen could be approximated to a linear body.

### Conclusions

Providing that the above-mentioned assumptions are reasonable (and there is no reason to question the assumptions if a lower limit of the bond strength is determined), it can be concluded that the 6061 Al/SiCp bond strength is at least 1690 MPa. (This is 40 times higher than the yield stress of the annealed 6061 Al alloy.) It is thought that debonding can be attributed to the defects during fabrication of the composite material. Ductile fracture of low-volume percent 6061/SiCp occurs by void nucleation at SiC particulates and also at the matrix imperfections (preexisting voids, inclusions,  $MgSi_2$ , etc.). A separate investigation, however, is required to determine explicitly the origin of the ductile fracture in Al/SiC systems. It is realized that the assumption of the equiaxiality of the SiCp is rather poor. This results in further under-estimation of the bond strength since, under the same macro stress state, irregular shaped particles would have higher stress concentrations, and, thus, separation from the matrix would be expected to occur at the earlier stage compared to a spherical particle. If the irregular shape of the particle could be taken into account, the lower limit would increase.

## REFERENCES

1. A. Kelly, "Strong Solids", 2nd Ed., Clarendon Press, Oxford, 1972.
2. M. R. Piggott, "Load-Bearing Fibre Composites", Pergamon Press, 1980.
3. B. D. Agarwal, L. J. Broutman, "Analysis and Performance of Fiber Composites", John Wiley & Sons, 1980.
4. R. J. Arsenault and R. M. Fisher, Scripta Met. 17, (1983) 67.
5. R. J. Arsenault and R. M. Fisher, Mech. Behavior of Materials, Ed. by J. Carlson and M. Olson, 1, (1983), 451.
6. R. J. Arsenault, Mat. Sci. & Eng, 64, (1984) 171.
7. Y. Flom and R. J. Arsenault, accepted for publication in Mat. Sci. & Eng.
8. A. P. Divecha, S. G. Fishman, and S. D. Karmarkar, Journal of Metals, September 1981, p. 12.
9. D. L. McDanel, NASA Technical Memorandum 83610, 1984.
10. L. J. Broutman and R. H. Krock, Interfaces in Metal Matrix Composites, Composite Materials, Vol. 1, Ed. by A. G. Metcalfe, Academic Press, 1974.
11. A. Kelly and W. R. Tyson, J. Mech. Phys. Solids, 13, (1965) 328.
12. L. M. Brown and J. D. Embury, Proc. of 3rd Int. Conf. on Strength of Metals and Alloys, Cambridge, U.K., 1973, p. 164.
13. G. LeRoy, J. D. Embury, G. Edward, and M. F. Ashby, Acta Met., 29, (1981) 1509.
14. J. D. Embury, "Ductile Fracture" in Strength of Metals and Alloys, Vol. 3, Ed. by R. G. Gifkins, Pergamon Press, 1983.
15. A. S. Argon, J. Im, and R. Safoglu, Met. Trans. A, 6A, (1975) 825.
16. A. S. Argon, J. Im, and A. Needleman, Met. Trans. A, 6A, (1975) 815.
17. A. S. Argon and J. Im, Met. Trans. A, 6A, (1975) 839.
18. University of Maryland, Metallurgical Materials Laboratory, unpublished results.

## List of Figures

Fig. 1 A schematic view of the specimen (a) and enlarged portion of the groove (b) showing groove geometry and location of the maximum triaxial stresses.

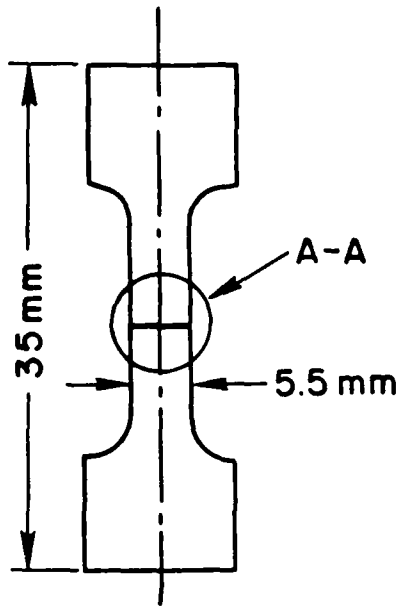
Fig. 2 Electron micrographs of the different areas of the longitudinal cross sections of the fractured 1V% Al/SiCp specimens.

(a,b) - taken in the vicinity of the bottom of the groove. No apparent debonding is present at the position of maximum triaxial stress.

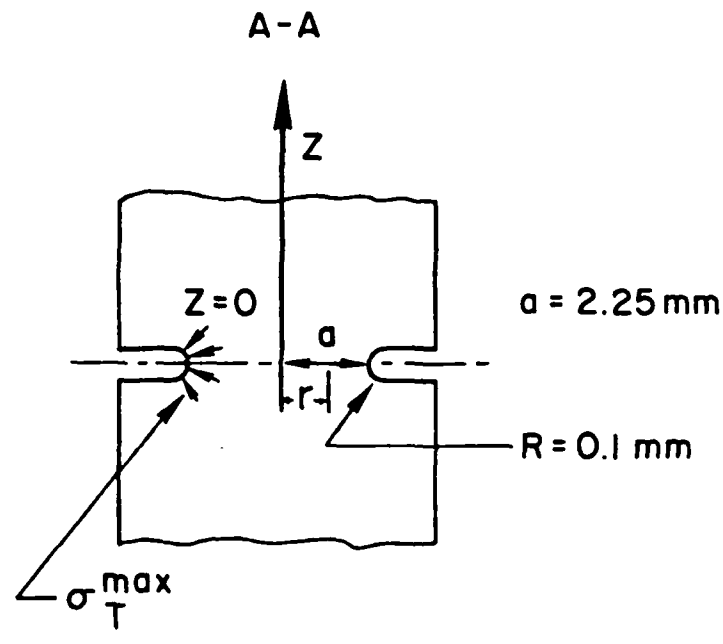
(c,d,e,f,g) - taken below the fracture surface away from the groove.

(h,i,j) - taken far away from the fracture and represent the bulk of the specimen.

Fig. 3 Electron micrographs of the areas below fracture surface at the bottom of the groove (a) and away from it (b-e) where debonding was observed.

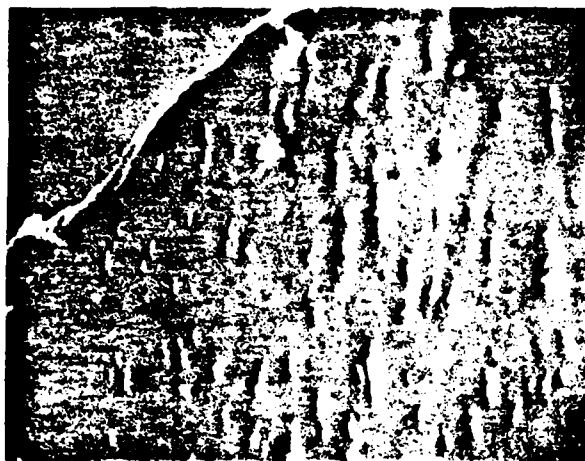


(a)



(b)

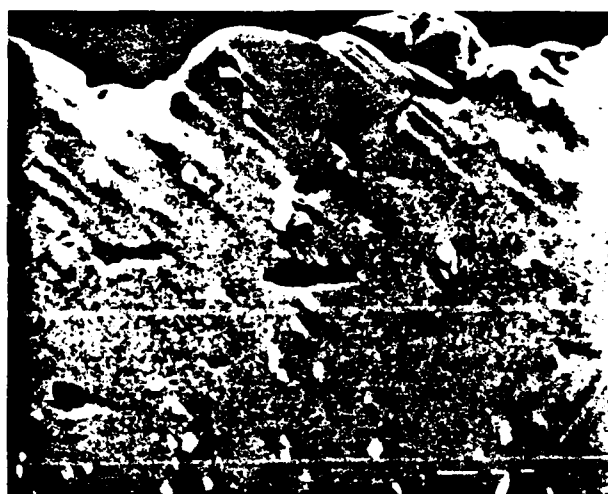
Fig. 1 A schematic view of the specimen (a) and enlarged portion of the groove (b) showing groove geometry and location of the maximum triaxial stresses.



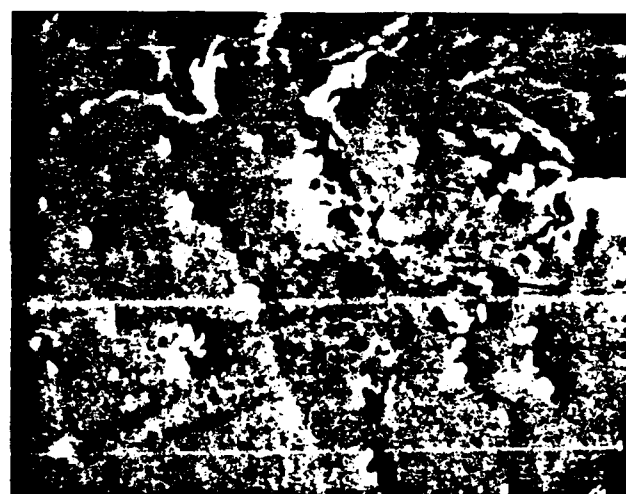
(A) x450



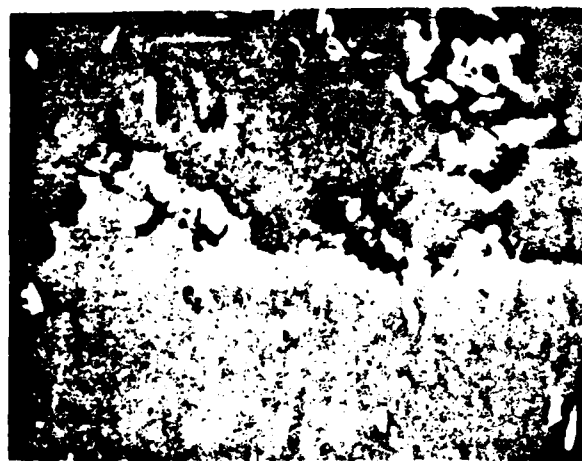
(B) x 600



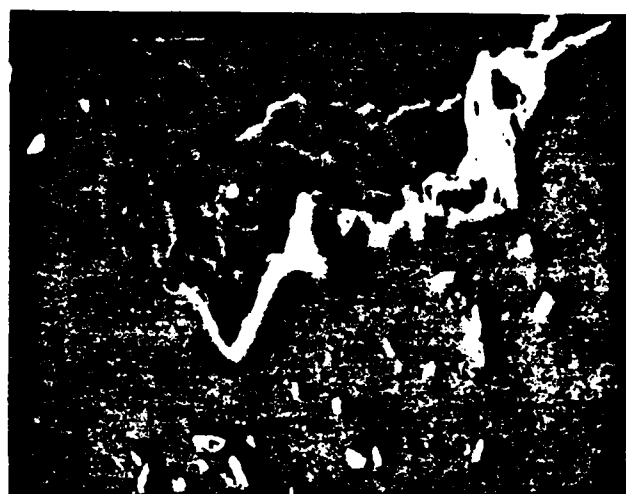
(C) x 550



(D) x 550



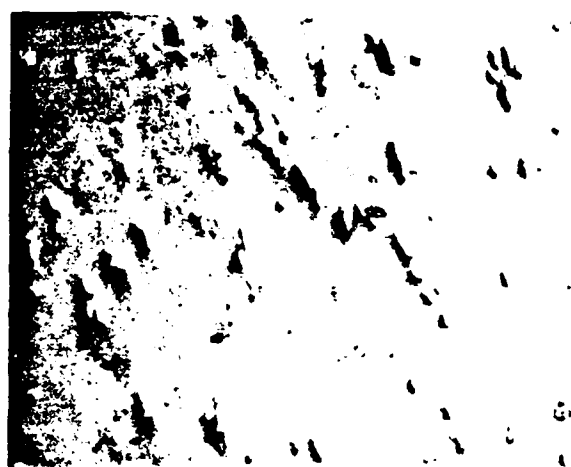
(E) x 1000



(F) x 700



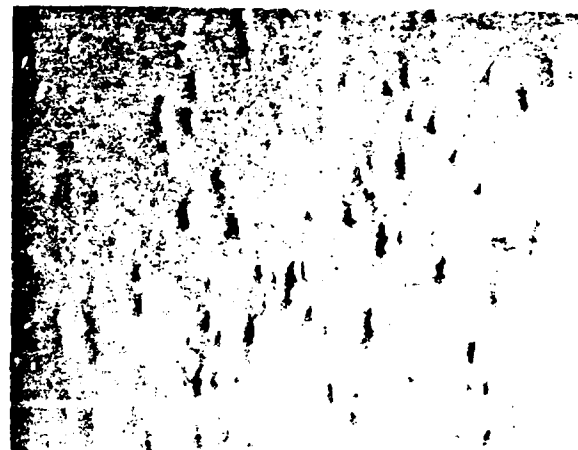
(G) x800



(H) x500



(I) x650



(J) x450

Fig. 2 Electron micrographs of the different areas of the longitudinal cross sections of the fractured 17% Al/SiCp specimens.

(a,b) - taken in the vicinity of the bottom of the groove. No apparent debonding is present at the position of maximum triaxial stress.

(c,d,e,f,g) - taken below the fracture surface away from the groove.

(h,i,j) - taken far away from the fracture and represent the bulk of the specimen.



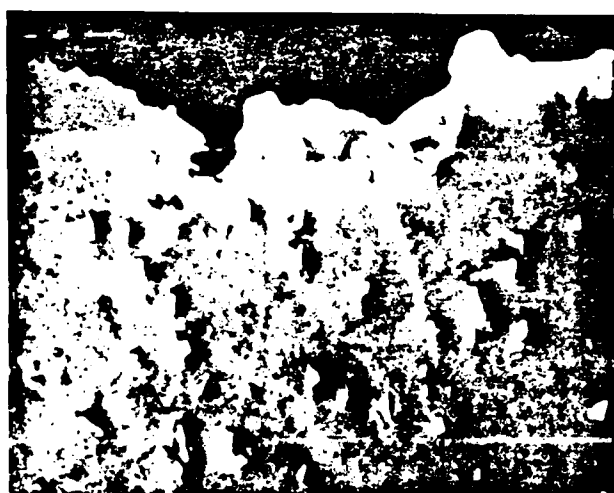
(A)

$\times 600$



(B)

$\times 500$



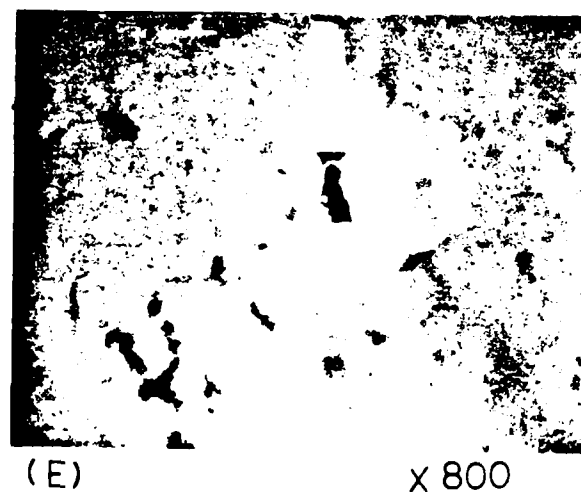
(C)

$\times 550$



(D)

$\times 800$



(E)

$\times 800$

Fig. 3 Electron micrographs of the areas below fracture surface at the bottom of the groove (a) and away from it (b-e) where debonding was observed.

# An *In Situ* HVEM Study of Dislocation Generation at Al/SiC Interfaces in Metal Matrix Composites

MARY VOGELSANG, R. J. ARSENAULT, and R. M. FISHER

Annealed aluminum/silicon carbide (Al/SiC) composites exhibit a relatively high density of dislocations, which are frequently decorated with fine precipitates, in the Al matrix. This high dislocation density is the major reason for the unexpected strength of these composite materials. The large difference (10:1) between the coefficients of thermal expansion (CTE) of Al and SiC results in sufficient stress to generate dislocations at the Al/SiC interface during cooling. In this *in situ* investigation, we observed this dislocation generation process during cooling from annealing temperatures using a High Voltage Electron Microscope (HVEM) equipped with a double tilt heating stage. Two types of bulk annealed composites were examined: one with SiC of discontinuous whisker morphology and one of platelet morphology. In addition, control samples with zero volume percent were examined. Both types of composites showed the generation of dislocations at the Al/SiC interface resulting in densities of at least  $10^{13} \text{ m}^{-2}$ . One sample viewed end-on to the whiskers showed only a rearrangement of dislocations, whereas, the same material when sectioned so that the lengths of whiskers were in the plane of the foil, showed the generation of dislocations at the ends of the whiskers on cooling. The control samples did not show the generation of dislocations on cooling except at a few large precipitate particles. The results support the hypothesis that the high dislocation density observed in annealed composite materials is a result of differential thermal contraction of Al and SiC. The SiC particles act as dislocation sources during cooling from annealing temperatures resulting in high dislocation densities which strengthen the material.

## I. INTRODUCTION

THE incorporation of 20 vol pct discontinuous SiC whiskers into a 6061 Al matrix increases the yield strength of annealed powder compacted 6061 Al alloy by more than a factor of two. This increase in strength cannot be explained directly by continuum mechanics theories. Continuum mechanics formulations developed by Piggott<sup>1</sup> and applied to the case of discontinuous Al/SiC composites by Arsenault<sup>2</sup> predict an ultimate strength of only 186 MPa for 20 vol pct SiC composite, whereas the measured value of ultimate strength for this material is 448 MPa. Arsenault and Fisher<sup>3</sup> proposed that the increased strength could be accounted for by a high dislocation density in the Al matrix which is observed in bulk composite material annealed for as long as 12 hours at 810 K.

The dislocation generation mechanism proposed by Arsenault and Fisher to account for this high dislocation density is based on the large difference (10:1) in coefficients of thermal expansion (CTE) of Al and SiC.<sup>4</sup> When the composite is cooled from elevated temperatures of annealing or processing, misfit strains occur due to differential thermal contraction at the Al/SiC interface which are sufficient to generate dislocations.

Chawla and Metzger, in an elegant investigation of Cu/W composites using etch-pitting techniques, observed a high dislocation density at the Cu/W interface which decreased with increasing distance from the interface.<sup>5</sup> They observed that if the volume fraction of W was 15 pct, the minimum dislocation density in the matrix was  $7 \times 10^{11} \text{ m}^{-2}$  in-

creasing to  $4 \times 10^{12} \text{ m}^{-2}$  at the interface of W and Cu, and concluded that the dislocations were caused by the differences (4:1) in CTE of Cu and W. Recalling that the CTE difference between Al and Si is 10:1, i.e., more than twice as great as the Cu/W system, one would expect thermal stresses in Al/SiC to be sufficient to generate dislocations in this composite.

Other causes may also contribute to the high dislocation density observed in annealed Al/SiC material. Dislocations are introduced into this material during the plastic deformation processes of manufacturing, such as extrusion. During annealing, the dislocations introduced during processing may not be annihilated; they could be trapped by the SiC, resulting in a high dislocation density after annealing.

It is important to determine the origins of the high dislocation density in the composite since the strength of the composite depends on the high density. If the differential thermal contraction is the cause of the dislocations, as Arsenault and Fisher<sup>3</sup> suggest, then dislocations should be observed being generated in a composite thin foil sample on cooling from annealing temperatures in an *in situ*, HVEM experiment.

*In situ* dynamic HVEM experiments have certain advantages over other experimental techniques. The major advantage is that direct observation of a dynamic process altering a microstructure is possible while the deforming force, in this case a thermal stress, is operating. Operating at higher voltages allows penetration of thicker samples so that surface effects are minimized and bulk behavior is more closely approximated. Also, a high voltage microscope can better accommodate special stages required for *in situ* work because of the large pole piece region.

Numerous *in situ* HVEM heating stage investigations of Al have been performed. Hale *et al.*<sup>6</sup> and Caillard and Martin<sup>7</sup> investigated dislocation motion during creep at

MARY VOGELSANG and R. J. ARSENAULT, Director, are with the Metallurgical Materials Laboratory, University of Maryland, College Park, MD 20742. R. M. FISHER is with Center for Advanced Materials, Lawrence Berkeley Laboratory, University of California, Berkeley, CA 94720.

Manuscript submitted April 8, 1985.

elevated temperatures using HVEM. Kivilahti *et al.*<sup>8</sup> observed an Al-2 pct Mg alloy *in situ* during recovery processes at elevated temperatures recording dislocation interactions on videotape. Shimotomori and Hasiguti<sup>9</sup> observed *in situ* prismatic punching of dislocation loops at second phase precipitates in an Al-1.3 pct Li alloy. Electron irradiation of Al at elevated temperatures has been extensively studied using HVEM.<sup>10,11</sup>

There have been several non-dynamic, non-*in situ* TEM investigations of dislocations about particles in a metal matrix. Weatherly<sup>12</sup> observed multiple slip mode dislocation tangles around silica in Cu, and concluded they were caused by differential thermal contraction of the two materials on quenching. Ashby *et al.*<sup>13</sup> observed dislocations about pressurized silica-Cu, noting a critical size dependence for dislocation generation. Williams and Garmong<sup>14</sup> reported a high incidence of dislocations at the Ni/W interface in this directionally solidified eutectic composite.

Calculations of the dislocation density in Al/SiC due to thermal stresses predict high dislocation densities. The misfit strain which develops at the circumference of a 1  $\mu\text{m}$  diameter SiC particle due to differential thermal contraction during cooling is approximately 1 pct. The plastic strain at one-half the interparticle spacing, obtained from Lee *et al.*,<sup>15</sup> ranges from 1 to 2 pct. The dislocation density can be simply calculated from the following equation:

$$\epsilon_p = \rho L b. \quad [1]$$

where  $\epsilon_p$  is the plastic strain (1 pct),  $\rho$  is the dislocation density ( $\text{m}^{-2}$ ) generated,  $L$  is the average distance moved by the generated dislocations, which was taken to be 1/2 the inter-whisker spacing, *i.e.*, 2  $\mu\text{m}$ , and  $b$  is the Burgers vector of Al. The  $\rho$  obtained is  $1.8 \times 10^{13} \text{ m}^{-2}$ .

Consideration of another type of dislocation described by Ashby<sup>16</sup> predicts additional dislocations in the matrix. These dislocations are called "geometrically necessary" dislocations by Ashby, and occur in order to allow compatible deformation of a system with geometrical constraints such as hard particles which do not deform as the surrounding ductile matrix. These geometrically necessary dislocations are required if the deformation takes place without the formation of voids about the hard particles. Slip dislocations are a function of the material properties of the system, and are not dependent on the microstructural constraints. According to Ashby, the density of geometrically necessary dislocations,  $\rho^G$ , is given by:

$$\rho^G = \frac{4\gamma}{\lambda^G b} \quad [2]$$

where  $\lambda^G$  is the "geometrical slip distance" analogous to the slip distance in pure crystals. For platelet particles,  $\lambda^G$  is equal to the length of the plate and  $\gamma$  is the shear strain. For a 1 pct shear strain and  $\lambda^G = 4 \mu\text{m}$ ,  $\rho^G$  equals approximately  $3 \times 10^{13} \text{ m}^{-2}$ . Taking these dislocations into account results in a further addition to the predicted dislocation density in the Al matrix.

The purpose of this investigation was to determine if dislocation generation occurs at the Al/SiC interface on cooling a composite from annealing temperatures, and to determine if the observed densities of dislocations generated during cooling are in agreement with densities predicted by theoretical calculations.

## II. MATERIAL

Three types of material were examined. The first was a SiC whisker composite purchased from ARCO-Silag. It is a powder metallurgy product: 6061 Al alloy powder is compressed with SiC whiskers to form a billet; then the billet is extruded to align the whiskers and form a 12.5 mm diameter rod. Three different volume fractions of SiC were considered: 0 pct, 5 pct, and 20 pct. The zero vol pct material served as a control.

The second type of composite was purchased from DWA, and contains SiC of platelet morphology. The platelets are 5 to 7  $\mu\text{m}$  long and have an aspect ratio of two to three. This composite is also a powder metallurgy product supplied in the form of a plate.

Third type of material was wrought 1100 grade Al in the form of a 12.5 mm diameter rod, and it was in the as-received condition. This material also served as a control.

## III. SAMPLE PREPARATION AND EXAMINATION PROCEDURE

An ion milling technique was required for the production of TEM samples due to the SiC in the Al matrix.

These two types of composite and the 0 vol pct control were machined into rods (12 mm in diameter, 4 cm long), annealed for 12 hours at a solutionizing temperature of 810 K, and furnace cooled. After annealing, slices of 0.76 mm thickness were cut by electric discharge machining (EDM) at 80 to 100 V. Deformation damage from EDM is estimated to extend 0.20 mm beneath the surface.<sup>17,18</sup> The slices were fixed to a brass block with double-sided tape and surrounded by brass shims, then mechanically thinned on a rotating water flooded wheel covered with 400 then 600 grit paper to remove the EDM damage and reduce the thickness to approximately 0.127 mm. Final thinning was carried out using argon ion plasma bombardment, operating at 6 kV, and ion current of 50 micro amperes and a sample inclination of 15 deg to the ion beam. For these operating parameters the projected range, or average distance the argon ion travels into the foil, is only 20 nm.<sup>19,20</sup> Dupuoy<sup>21</sup> conducted an *in situ* ion thinning experiment on Fe and Al-Ag specimens using a 3 MV microscope. Dislocation arrangements and microstructures in Al-Ag and Fe are not altered by ion thinning even though some point defects are introduced into the near surface region of the sample by ion bombardment. Therefore, it can be concluded that ion-milling does not introduce or remove dislocations in the TEM foils.

The 1100 grade Al control samples were prepared from the as-received wrought rod in the same manner as the composite samples, except electro-polishing was employed instead of ion-thinning.

The thinned samples were then observed in the HVEM operating at 800 kV with a beam current of 2.3  $\mu\text{A}$ . A double tilt, side-entry, furnace type heating stage was used to heat the specimen. While being observed in the microscope, the samples were heated to 800 K and held for 15 minutes, then cooled to ambient temperature. Subgrains exhibiting dislocations in contrast were chosen for observation. During heating and cooling, thermal drift of the stage and thermal expansion and contraction of the sample caused the chosen subgrain to move. In order to maintain the

same subgrain in the field of view at the same crystallographic orientation, it was necessary to slightly translate and tilt the specimen almost continuously. Since changing to SAD conditions during cycling to monitor orientation would have resulted in loss of the chosen area from the field of view, the orientation was maintained constant by monitoring the contrast of microstructures such as a subgrain boundary or SiC/Al interface in the bright-field mode. One thermal cycle required about one hour, and most of the samples were observed throughout several thermal cycles. The thickest regions of the sample penetrated by the beam were chosen for observation, and at operating voltage of 800 KV the beam will penetrate 0.8  $\mu\text{m}$  thick Al.<sup>22</sup> The dislocation density,  $\rho$ , was determined by a line intercept method adapted from Hale.<sup>23</sup> A grid of lines is placed over the TEM micrograph, then the intersections of dislocation lines with the grid lines are counted. The dislocation density,  $\rho$ , is given by

$$\rho = \frac{2N}{LT}$$

where  $N$  is the number of dislocation intersections with the grid lines,  $L$  is the length of the grid lines divided by the magnification,  $t$  is the thickness of the sample (0.8  $\mu\text{m}$ ), and the length of the lines on the grids was 0.58 m. Each reported dislocation density is an average value obtained from 3 to 10 micrographs.

#### IV. RESULTS

The discussion of the experimental results will be divided into three parts: 0 vol pct, 5 vol pct, and 20 vol pct of SiC. In all cases, typical results will be described. A total of 800 micrographs were taken.

##### A. Controls. 0 Vol Pct SiC, 6061 Al, and 1100 Al

The 0 vol pct 6061 Al control sample had a large subgrain size (approximately 5  $\mu\text{m}$ ) and a low dislocation density ( $8 \times 10^{12} \text{ m}^{-2}$ ) (Figure 1(a)). A few of the larger second phase precipitate particles (Mg<sub>2</sub>Si) were surrounded by dislocation tangles bowing out from the precipitate interface (Figure 1(b)). On heating, the dislocations began to move in the sample, migrating away from the particles. Other dislocations were also generated in other areas of the subgrain and moved through the matrix, occasionally being pinned by precipitate particles. Eventually, at elevated temperatures (670 K), all of the dislocations disappeared. Slip traces left behind when the dislocations moved also disappeared at temperatures close to 700 K, possibly due to surface diffusion. The sample was held at 800 K for about 15 minutes.

The image tended to be out of focus at high temperatures due to thermal drift of the stage (Figures 1(b) and 1(c)). On cooling, dislocations reappeared at the large particle interface at about 500 K, sometimes moving faster than they could be seen. The dislocations formed tangles in the vicinity of the precipitate; however, most of the matrix did not accumulate any dislocations (Figure 1(d)). There were a few dislocations generated at subgrain or grain boundaries.

The 1100 Al sample had a dislocation density initially of  $4 \times 10^{12} \text{ m}^{-2}$ , and a large subgrain size, 5  $\mu\text{m}$  (Figures 2(a)

and 2(b)). Thicker regions containing few precipitates were chosen for observation. On heating, most of the dislocations had disappeared by 673 K. At this temperature, the heating stage mechanism failed; therefore, the sample never reached 800 K, but heating was sufficient to remove the dislocations from the area under observation. The dislocations in this area did not return on cooling, except a few which were connected to precipitate particles (Figures 3(a) and 3(b)).

##### B. 5 Vol Pct—Transverse and Longitudinal Whisker SiC

The 5 vol pct whisker sample, sectioned transverse to the whiskers so that the hexagonal whiskers are viewed end-on in the microscope, had a small subgrain size, 2.0  $\mu\text{m}$ , and a high dislocation density,  $4 \times 10^{13} \text{ m}^{-2}$ , in the subgrains (Figure 4(a)). In this case, on heating the dislocations did not disappear but straightened from an initially bowed configuration and became more regularly spaced: a polygonized configuration. These dislocations did not disappear at high temperatures (Figures 4(b) and 4(c)). On cooling, the dislocations again bowed away from the Al/SiC interface but the density of dislocations did not increase; if anything, the number slightly decreased (Figures 4(d) and 4(e)). Several of the subgrains appeared to change shape during the thermal cycle; however, their boundaries did not move past the surrounding SiC whiskers.

The longitudinal 5 vol pct sample, sectioned parallel to the SiC whisker axis so that the whiskers could be viewed lengthwise, did show the characteristic disappearance of dislocations at high temperatures, and then the return of dislocations on cooling, especially at the ends of the whiskers (Figures 5(a) through (f)). The parallel lines in the whiskers have been previously identified as microtwins.<sup>24</sup>

##### C. 20 Vol Pct Whisker and Platelet

The microstructure of the 20 vol pct whisker sample before heating is characterized by a small subgrain size of the order of 2 to 3  $\mu\text{m}$  and also by a dislocation density of about  $10^{13} \text{ m}^{-2}$  (Figure 6(a)). The sample was heated while focusing on a single subgrain surrounded by several SiC whiskers. The dislocations began to move and rearrange, some moving very quickly, and eventually disappearing. Upon reaching 470 K most of the dislocations had disappeared. The sample was heated further to 800 K (Figure 6(b)), held for a few minutes, and then cooled. On cooling, dislocations reappeared and emanated from the whisker interface forming a tangle of dislocations in the small subgrain. Although some dislocations began appearing on cooling at about 473 K, a great number of them formed at temperatures less than 373 K. The dislocation density after cooling was comparable to the dislocation density before the thermal cycle (Figures 6(c), 6(d), and 6(e)). When black spots began obscuring the picture, another area free of the black spots was moved into the field of view.

The 20 vol pct platelet sample (Figure 7(a)) exhibited behavior similar to the whisker sample, in that most of the dislocations disappeared upon reaching 650 K (Figure 7(b)), and then on cooling, dislocations reappeared (Figures 7(c) and 7(d)). However, certain aspects of the microstructural alterations on cooling were peculiar to the platelet sample. In the first cycle, the dislocations disappeared and then reappeared on cooling. An unusual subgrain was observed

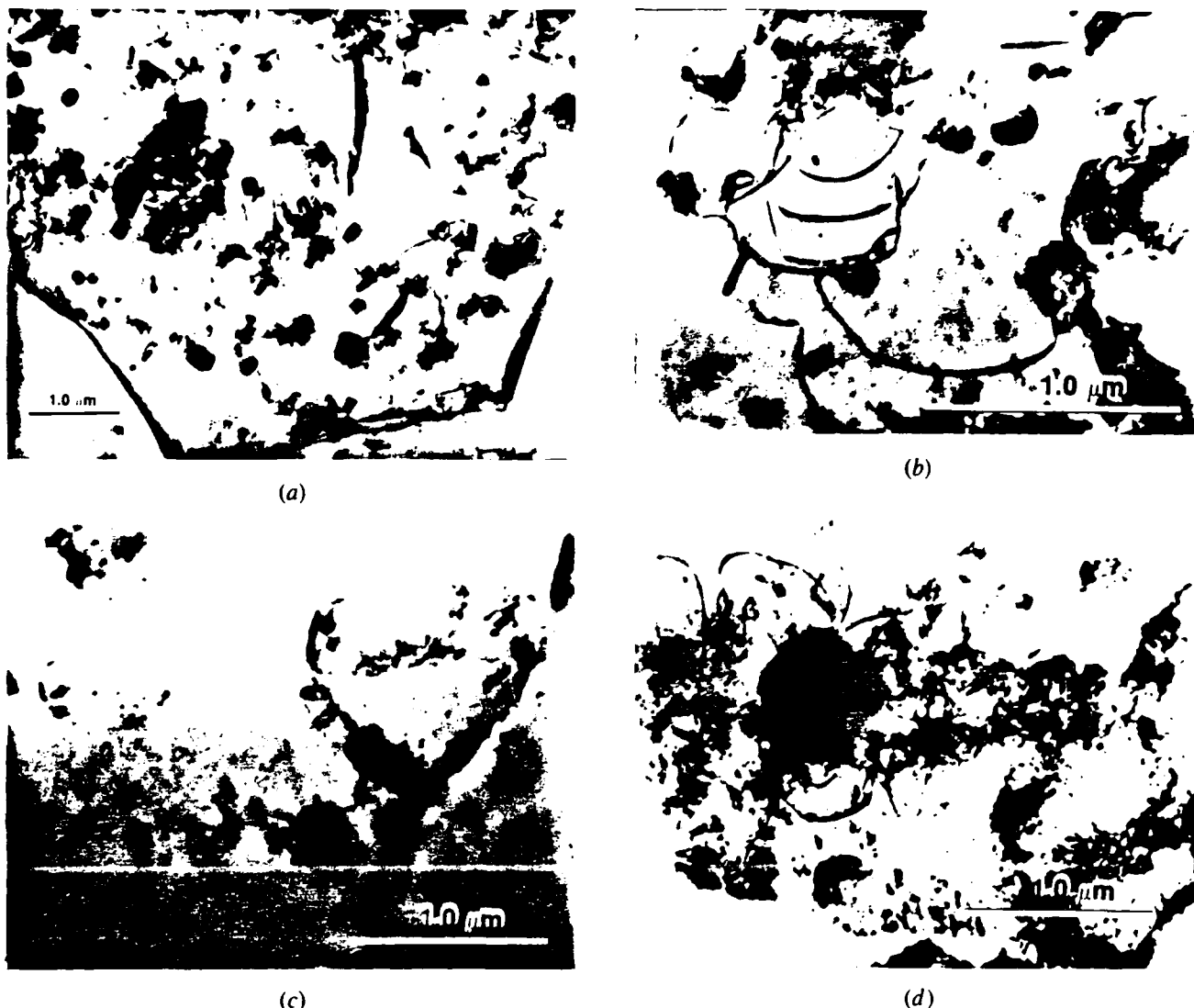


Fig. 1—(a) Micrograph of a control sample illustrating the low dislocation density and the large grain size of annealed powder compacted 6061 Al with no SiC. The few dislocations present in this control sample are associated with the second phase precipitates of the 6061-Al alloy. Compare the dislocation densities and subgrain sizes with those of composites shown in Figs. 4(a), 6(a), and 7(a). (b) A large second phase precipitate (top center) surrounded by dislocations at the beginning of the thermal cycle (340 K). (c) As temperature increased to annealing temperatures in the microscope (780 K), the dislocations gradually disappeared until only a few remained (same area as Fig. 1(b)). (d) During *in situ* cooling of the control sample dislocations reformed in the area of the precipitates, shown here. However, most of the matrix remained free of dislocations (same area as Figs. 1(a) and 1(b)).

which was filled with slip traces. This area was chosen as the area of focus in the next cycle. The parallel lines disappeared on heating; then on subsequent cooling, packets of slip traces appeared emanating from the SiC platelet. The slip traces formed in three directions at angles of about 82 deg and 45 deg to each other and were associated with dislocations which had appeared. The dislocations causing the slip traces had moved too quickly to be seen. After the third thermal cycle, many subgrains were filled with slip traces originating at the SiC platelet interface.

#### D. Dislocation Densities

The dislocation densities of all samples before and after *in situ* annealing are shown in Table I. The densities are higher in the composite samples than in the control samples

both before and after *in situ* thermal cycling, *i.e.*, annealing. However, the dislocation densities reported are lower limit densities. There was difficulty in taking selected area diffraction patterns of a given subgrain and then tilting to a specific reflection, *i.e.*, [420] and assuring that the same orientation was maintained throughout. Therefore, the reported densities could be  $\frac{1}{2}$  to  $\frac{1}{3}$  of the actual density.<sup>25</sup>

The distribution of the dislocations within the samples was not uniform; there was a higher density, as to be expected, near the SiC. Also greater dislocation generation was observed at larger SiC platelets and whiskers than at the smaller ones, and more dislocations were generated at the ends of the SiC whiskers where plastic strain during cooling is greatest, than at the middle of the whisker length. The dislocation generation in the platelet sample was much greater than the dislocation generation in the

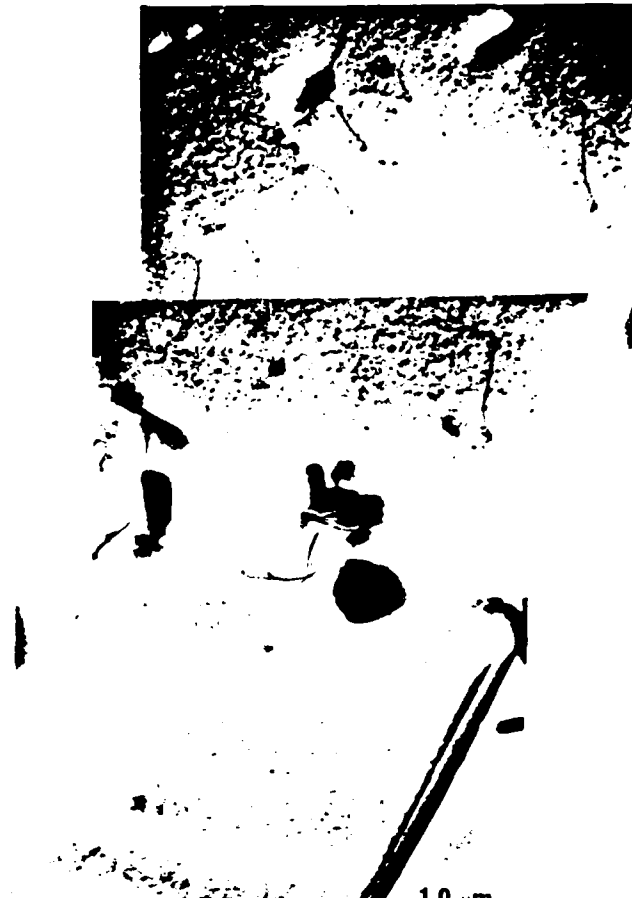


(a)

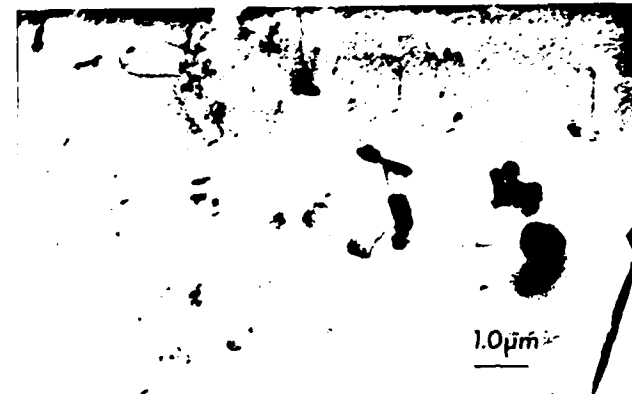


(b)

Fig. 2—(a) Wrought 1100 Al control sample, as-received condition. Before *in situ* thermal cycling, this control sample with no SiC had a high dislocation density. Like the 6061 Al control, this sample has a large grain size, and the dislocations present are often associated with precipitates. The white structure is a corrosion tunnel from electropolishing. (b) Low magnification view of 1100 control sample including area of Fig. 2(a).



(a)



(b)

Fig. 3—(a) The same areas in Fig. 2(a) after *in situ* thermal cycling. In the absence of SiC, few dislocations reappear in a thermally cycled sample; the few dislocations present are associated with second phase precipitate particles. (b) Low magnification view of area in Fig. 3(a) after thermal cycling.



(a)



(b)



(c)



(d)



(e)

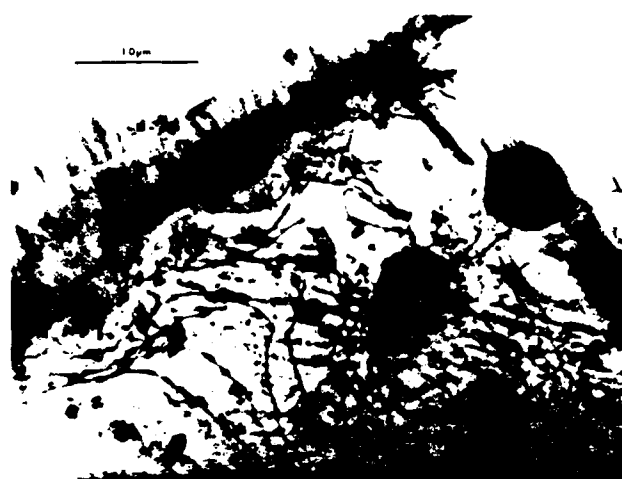
Fig. 4—(a) A foil cut transverse to the whisker axis (5 vol pct SiC). At the beginning of the thermal cycle, 370 K, the dislocations tended to bow away from the two hexagonal SiC whiskers. (b) The dislocations straighten on further heating to 570 K (same area as Fig. 4(a)). (c) Further rearrangement of the dislocations occurred on heating to the annealing temperature of 800 K in the microscope. The dislocations straightened and moved to more equally spaced positions (same area as Figs. 4(a) and 4(b)). (d) During cooling to 570 K the dislocations again began to bow away from the SiC whiskers (same area as Figs. 4(a-c)). (e) On cooling to 360 K, the curvature of the dislocations became pronounced, indicating the operation of a thermal stress; however, the generation of new dislocations did not occur (same area as Figs. 4(a-d)).

whisker samples, for SiC platelets are about 5 times larger than SiC whiskers.

As a consequence, of all the dislocation generation, there is a possibility of void formation at the SiC-Al interface. Voids were not observed in any of the samples.

## V. DISCUSSION

The presence of SiC particles of either whisker or platelet morphology in an Al metal matrix composite resulted in the generation of dislocations at the Al/SiC interface when the



(a)



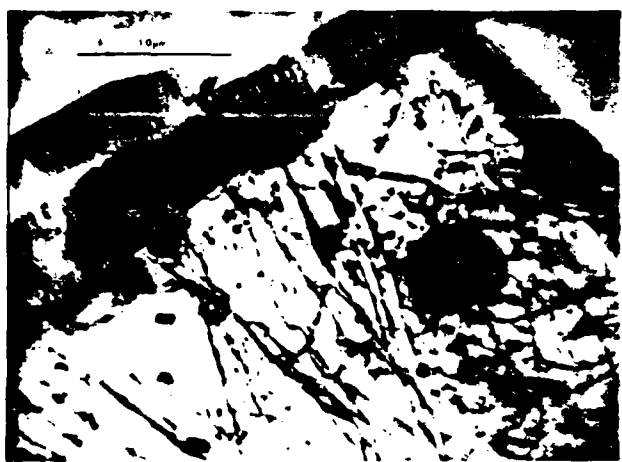
(b)



(c)



(d)

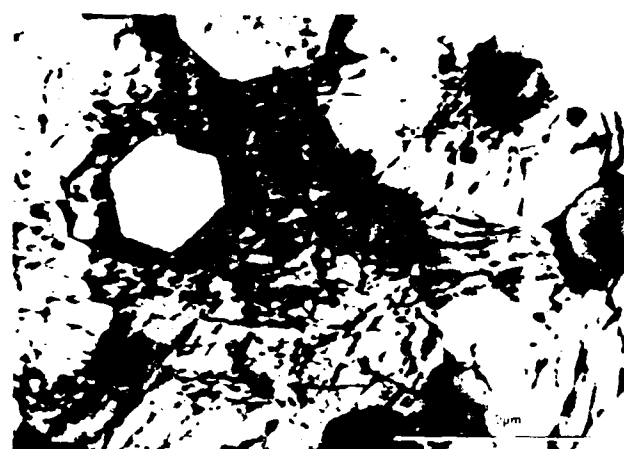


(e)



(f)

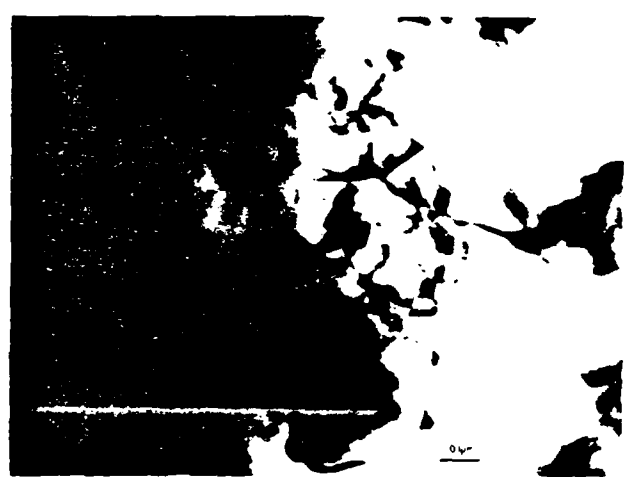
Fig. 5—(a) This sample was prepared from the same 5 vol pct whisker material shown in Figs. 4(a-e), only sectioned parallel to the SiC whisker axis. Dislocations are associated with the SiC and second phase precipitates at the beginning of the thermal cycle at 340 K. Also visible are parallel slip traces from the previous thermal cycle. (b) The same region at annealing temperature, 810 K, after most dislocations have disappeared. (c) The same area after one dislocation has reappeared on cooling to 580 K. (d) On further cooling the sample to 480 K more dislocations have formed, some leaving slip traces as they moved away from the Al/SiC interface. (e) On cooling to 430 K, dislocation activity greatly increased as evidenced by the higher density of dislocations and slip traces. (f) Another location in the sample at 340 K which also shows dislocation generation clearly associated with the SiC. This area was not irradiated by the electron beam during the thermal cycle.



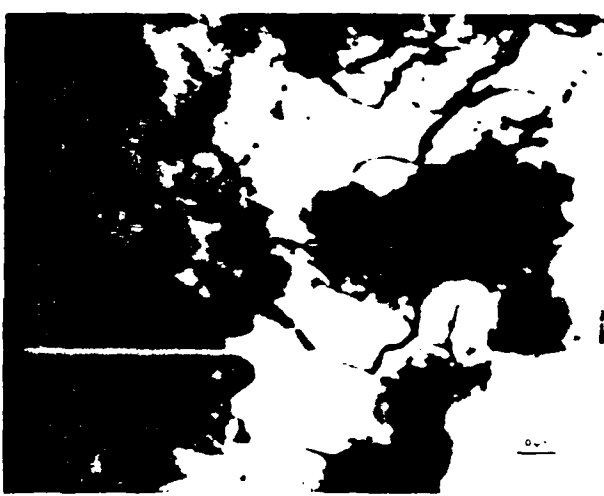
(a)



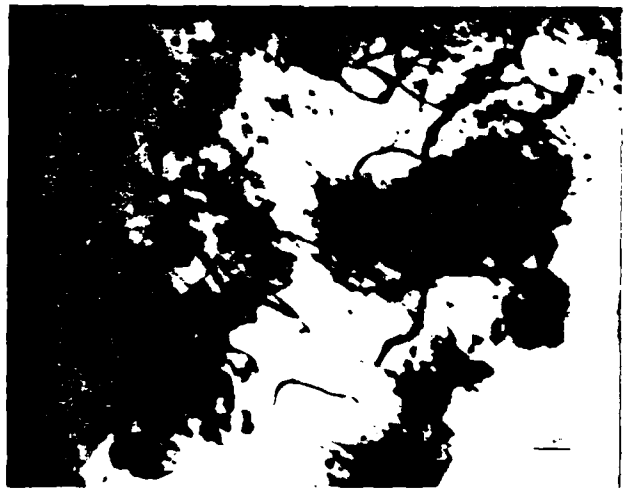
(b)



(c)



(d)



(e)

composite was cooled from the annealing temperature. In general, the high density of dislocations originally present in the composite samples disappeared at 500 to 650 K, then reappeared on cooling at densities close to the high densities originally observed in the annealed specimens. In contrast,

Fig. 6—(a) The initial high dislocation density and small subgrain size of the 20 vol pct whisker composites is shown here. (b) The dislocations disappeared from the sample during *in situ* heating to 800 K. Thermal drift of the stage prevented sharp focusing of the image. (c) On cooling to 375 K, dislocations had reappeared in the sample, emanating from the Al/SiC interface and moving into the matrix until a dislocation tangle formed. (d) The clear area at 375 K (Fig. 6(c)) as temperature decreased to 340 K. Black spots also began to form on the sample at this temperature. (e) At lower center, the appearance of a hook-shaped dislocation is observed. The black spots have become more prominent, 330 K.

dislocations were not generated to the same extent in either of the control samples during cooling.

The small subgrain size and high dislocation densities previously observed by Arsenault and Fisher<sup>7</sup> can be associated with the presence of the SiC in the composite, specifically the CTE differential. The difference in CTE resulted in stresses large enough to cause plastic deformation, *i.e.*, the generation of dislocations. These dislocations can be defined as slip dislocations. Dislocation generation is also required to accommodate the heterogeneous plastic flow in the vicinity of the deforming matrix since voids are not observed. We can conclude, therefore, that both of

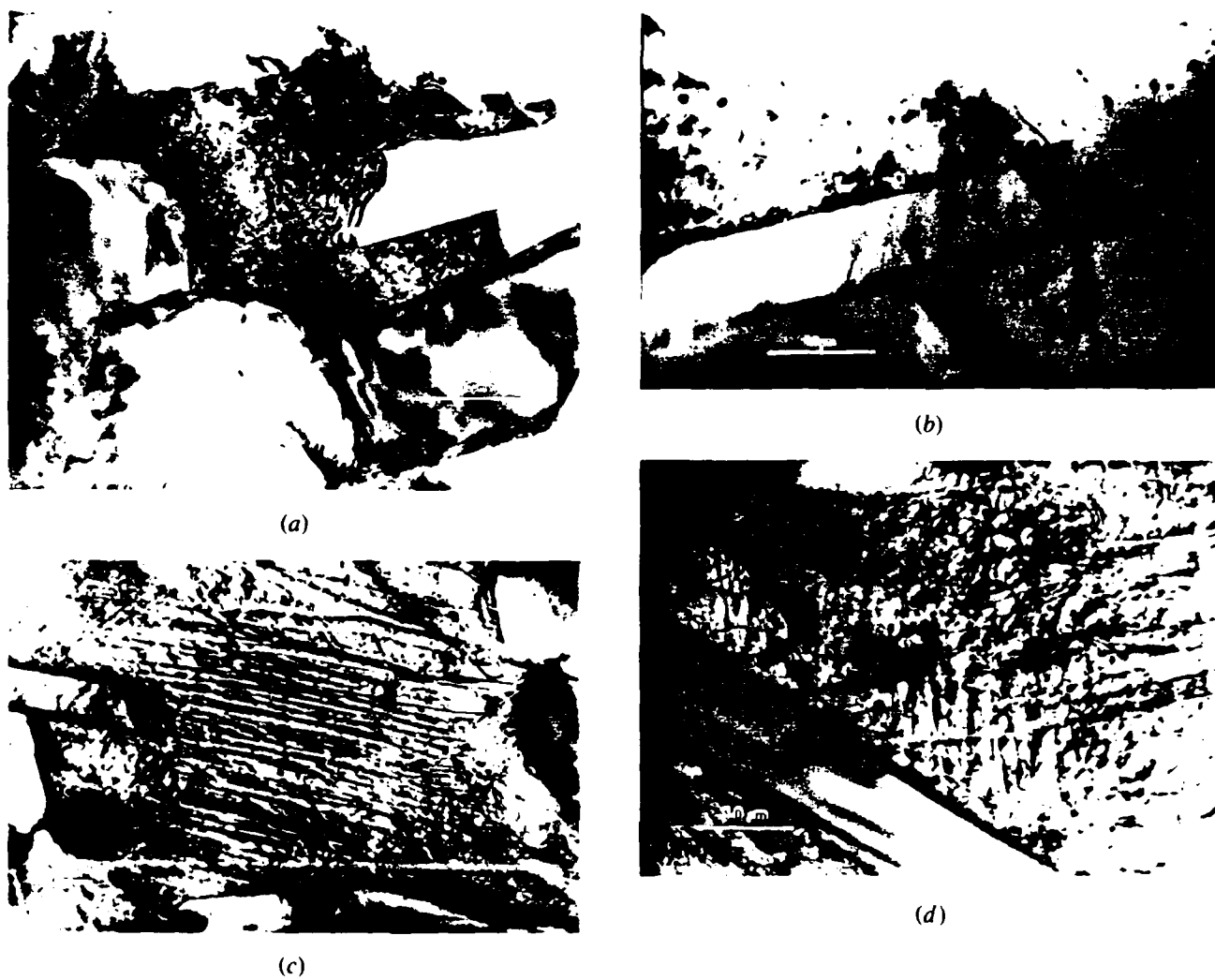


Fig. 7—(a) The diffraction contrast of the high dislocation density in the central subgrain darkens the subgrain in this 20 vol pct SiC platelet composite. The subgrain is surrounded by at least three irregularly shaped SiC platelets which are approximately the same size as the subgrain. (b) During heating to 650 K most of the dislocations disappeared from the sample. The pebble-like second phase precipitates can be clearly distinguished here. The same area is shown in (d) filled with slip traces. (c) On cooling to 340 K, dislocations reappeared, resulting in the formation of dense slip traces showing the paths of the dislocations as they moved across or out of the sample. (d) This is the same area as shown in (b) after cooling to 340 K. The area was free of almost all dislocations at high temperature. The subgrain is now filled with slip traces and dislocations. The slip traces are clearly associated with the SiC platelets indicating that the origin of the dislocations seen in the sample at low temperature is the Al/SiC interface.

Table I. Dislocation Density before and after Thermal Cycling of Samples; Dislocation Density ( $\text{m}^{-2}$ )

Sample	Before Thermal Cycle	After Thermal Cycle
(1) 20 vol pct whisker*	$2.0 \times 10^{11}$	$1.0 \times 10^{11}$
(2) 20 vol pct platelet*	$2.0 \times 10^{11}$	$4.0 \times 10^{12}$
(3) 5 vol pct whisker*	$4.0 \times 10^{11}$	$2.0 \times 10^{11}$
(4) 0 vol pct whisker*	$8.0 \times 10^{12}$	$6.4 \times 10^{12}$
(5) 1100 Al sample*	$4.0 \times 10^{12}$	$5.3 \times 10^{11}$

\*Bulk annealed 12 hours at 800 K.

\*As-received 1100 grade wrought Al alloy.

these mechanisms are operating, which results in a high dislocation density due to the SiC in the matrix. In the vicinity of precipitates, transformation strains can also produce dislocations.

The exception to the generally observed disappearance of dislocations on heating was the 5 vol pct transverse sample for which no satisfactory explanation has been

found. A stable polygonized substructure appeared to prevent the disappearance of the dislocations at high temperatures. Backstresses from these dislocations on cooling could have prevented further generation of dislocations in the small subgrains on cooling.

The intensity of dislocation generation at the SiC-Al interface is related to size and shape of SiC particle. The intensity

of generation is lowest for small, nearly spherical particle. As the particle size increases, *i.e.*, from 1  $\mu\text{m}$  to 5  $\mu\text{m}$ , the intensity of generation increases significantly. Also the intensity is much greater at the corner of a particle than along the sides as is evidenced in the longitudinal whisker and platelet composite samples. The relationship between the size of the particle and the plastic zone has been qualitatively described by Lee *et al.*,<sup>15</sup> and they predicted that as the particle size increases the plastic zone size increases. Also, Lee<sup>26</sup> has shown that the plastic strain about the corner of a particle is greater than along the side (which should be intuitively obvious).

Experimental conditions which may influence the results must be recognized and considered in an HVEM experiment, because the sample is exposed to high energy electrons, and thin foil samples are used to approximate bulk behavior. Surface effects are among the most important effects to be considered, since it is easy for dislocations generated at the Al/SiC interface to move out of the sample through the surfaces of a TEM foil. Thick sections of the foil were examined in the HVEM in order to reduce surface effects; nevertheless, dislocation relaxation out the surface occurred, and resulted in a reduction of the observed dislocation density. This effect is most apparent in the 20 vol pct platelet sample where the slip traces, indicating that dislocations have moved out of the sample, nearly cover the entire surface of the sample. In bulk specimens, dislocations would accumulate in the subgrains until the ensuing backstresses due to the pile-up exceeded the local yield stress surrounding the particle. Also, the geometry of a thin foil specimen allows elastic relaxation of stresses on cooling by buckling, also giving an artificially low value of the dislocation density.

The effects of irradiation of the samples by the high energy electrons of the beam must also be considered. Electron irradiation of the sample can result in the formation of vacancy clusters and small dislocation loops which appear as black spots and then grow to form dislocation tangles.<sup>11</sup> The observation of black spots on some of the samples (Figures 1(d) and 6(d)) indicated that electron irradiation damage most probably occurred.

The control samples were invaluable in determining that the dislocations generated on cooling were not artifacts due to the effects of electron irradiation. In the 6061 0 vol pct SiC control sample a few dislocations were generated at a few large precipitates.

The 1100 control samples were also exposed to the high energy electron beam and substantial formation of dislocations did not occur (Figures 3(a) and 3(b)). Also the intensity of dislocation generation can be correlated with the size, volume fraction, and shape of the SiC or second phase precipitate particles present, indicating that the particles and not the electrons of the beam were the cause of the dislocations being generated. A more likely explanation of the appearance of the black spots is beam contamination. The decontaminator was not always operating, and beam contamination usually condenses on samples at temperatures less than 473 K which coincides with our observations.<sup>27,28</sup> Some of the black spots could also be due to second phase precipitation in the samples on cooling, since the spots were sometimes preferentially associated with interfaces and grain boundaries (Figures 1(d) and 7(d)).

Beam heating is another factor to be considered. For our operating conditions, beam heating of the sample is approximately 10 to 15 K, and this could have had an effect on dislocation generation in the sample due to the thermal gradient which is induced.<sup>27,29</sup> But examination of the same composite samples without thermal cycling did not result in dislocation generation at the Al/SiC interface, and these samples were exposed to the same beam conditions.

Due to the difficulty associated with tilting a very fine subgrained material to the various diffracting conditions required to image all of the dislocations in the subgrain, the reported densities could be  $\frac{1}{3}$  to  $\frac{1}{2}$  below the actual number. Although more rigorous tilting would give more precise values, a good idea of the relative densities in the samples can be obtained by imaging dislocations in many subgrains for each material and assuming that the value will be systematically low for all the samples.

The net result of considering all of the experimental factors which may influence the experimentally determined dislocation densities after a thermal cycle, is: (1) the dislocation generation observed during cooling can be readily attributed to differential thermal contraction of the Al and SiC, (2) the observed densities are lower than the densities which would be observed if bulk samples could be examined and if diffracting conditions were controlled to image all dislocations.

It should also be pointed out that slip line generation about a SiC cylinder in an Al disk due to thermal cycling has been demonstrated by Flom and Arsenault.<sup>30</sup>

## VI. CONCLUSIONS

From a consideration of the experimental results, the following conclusions can be drawn:

1. The high dislocation density ( $10^{14} \text{ m}^{-2}$ ) previously observed in bulk annealed composites is due to differential thermal contraction of Al and SiC on cooling from the elevated temperatures of annealing.
2. The density of dislocations observed in this experiment as a result of thermal cycling is lower than the actual density generated during thermal cycling because dislocations are lost through the surfaces of the thin foil samples during cooling.
3. The densities of dislocations observed ( $10^{13} \text{ m}^{-2}$ ) would be equal to the high densities previously observed in bulk annealed composites if it were not for dislocation loss through the surfaces, and the observed densities would be closer to densities predicted by calculations  $4 \times 10^{13} \text{ m}^{-2}$ , if it were not for dislocation loss through the surfaces.
4. Thermal cycling causes the disappearance of dislocations at high temperatures and the generation of dislocations at Al/SiC interfaces and precipitates on cooling. Subgrain growth is hindered by the presence of SiC particles. Transformation strains also cause dislocation generation at precipitates, and polygonized configurations prevent the disappearance of dislocations at high temperatures.

## ACKNOWLEDGMENTS

The authors wish to acknowledge A. Szirmai and J. W. Conroy of the U.S. Steel Research Laboratory, and C. R. Feng

and Y. Flom of the University of Maryland for assistance with the experiments. Effective liaison with Drs. Bruce McDonald and Steve Fishman of the Office of Naval Research in Arlington, VA has been very helpful to the project.

## REFERENCES

1. M. R. Piggott: *Loading Bearing Fibre Composites*, Pergamon Press, Oxford, 1980.
2. R. J. Arsenault: *Mat. Sci. and Eng.*, 1984, vol. 64, p. 171.
3. R. J. Arsenault and R. M. Fisher: *Scr. Metall.*, 1983, vol. 17, p. 67.
4. A. Taylor and R. M. Jones: *Silicon Carbide*, J. R. O'Connor and J. Smiltens, eds., Pergamon Press, Oxford, 1960, pp. 147-54.
5. K. K. Chawla and M. Metzger: *J. of Mat. Sci.*, 1972, vol. 7, p. 34.
6. K. F. Hale, M. Henderson-Brown, and Y. Ishida: *Proc. 5th European Congress on Electron Microscopy*, 1972, p. 350.
7. D. Caillard and S. L. Martin: *Acta Metall.*, 1983, vol. 31, p. 813.
8. J. K. Kivilahti, V. K. Lindroos, and B. Lehtinen: *Proc. 3rd Int. Conf. on HVEM*, P. R. Swann, C. J. Humphreys, and M. J. Goringe, eds., Academic Press, London, 1974, p. 19.
9. M. Shimotomori and R. R. Hasiguti: *J. Japan Inst. Met.*, 1979, vol. 43, p. 4.
10. A. Wolfenden: *Radiat. Eff.*, 1972, vol. 14, p. 225.
11. J. O. Stiegler and K. Farrell: *Proc. 3rd Int. Conf. on HVEM*, P. R. Swann, C. J. Humphreys, and M. J. Goringe, eds., Academic Press, London, 1974, p. 341.
12. G. C. Weatherly: *Met. Sci. J.*, 1968, vol. 2, p. 237.
13. M. F. Ashby, S. H. Gelles, and L. E. Tanner: *Phil. Mag.*, 1969, vol. 19, p. 757.
14. J. C. Williams and G. Garmong: *Metall. Trans. A*, 1975, vol. 6A, p. 1699.
15. J. K. Lee, Y. Y. Earmme, H. I. Aaronson, and K. C. Russell: *Metall. Trans. A*, 1980, vol. 11A, p. 1837.
16. M. F. Ashby: *Phil. Mag.*, 1970, vol. 21, p. 399.
17. A. Szirmai and R. M. Fisher: "Techniques of Electron Microscopy, Diffraction, and Microprobe Analysis", Special Technical Publ. #372, ASTM, 1965.
18. L. E. Samuels: *Metallographic Polishing Methods*, Sir Issac Pitman & Sons, Ltd., Melbourne, 1971, p. 79.
19. D. G. Howitt: *Analytical Electron Microscopy*, Roy H. Geis, ed., San Francisco Press, San Francisco, CA, 1981, p. 252.
20. P. D. Townsend, J. C. Kelly, N. E. W. Hartley: *Ion Implantation, Sputtering, and Their Applications*, Academic Press, London, 1976, p. 311.
21. G. Dupuoy: "Megavolt Electron Microscopy", *Proc. 3rd Int. Conf. on HVEM*, P. R. Swann, C. J. Humphreys, and M. J. Goringe, eds., Academic Press, London, 1974, p. 447.
22. H. Fujita, T. Tabata, N. Sumida, and K. Yoshida: *Proc. 3rd Int. Conf. on HVEM*, P. R. Swann, C. J. Humphreys, and M. J. Goringe, eds., Academic Press, London, 1974, p. 427.
23. K. F. Hale and M. Henderson-Brown: *Micron*, 1973, vol. 4, p. 69.
24. J. Feng: Master's Thesis, Univ. of Maryland, College Park, MD, 1981.
25. P. B. Hirsch, R. B. Nicholson, A. Howie, D. W. Pashley, and M. J. Whelan: *Electron Microscopy of Thin Crystals*, Butterworth & Co., London, 1965, p. 423.
26. J. Lee: private communications, Michigan Technological University, Houghton, MI, 1984.
27. E. P. Butler and K. F. Hale: "Dynamic Experiments in the Electron Microscope", in *Practical Methods in Electron Microscopy*, Audrey M. Glauert, ed., Elsevier-North Holland Biomedical Press, Amsterdam, 1981, vol. 9.
28. G. M. Scamans and E. P. Butler: *Metall. Trans. A*, 1975, vol. 6A, p. 2055.
29. S. B. Fisher: *Radiat. Eff.*, 1970, vol. 5, p. 239.
30. Y. Flom and R. J. Arsenault: *Mater. Sci. and Eng.*, in press.

Thermal Residual Stress in Metal Matrix Composite\*

Richard J. Arsenault  
Engineering Materials Group  
University of Maryland  
College Park, MD 20742 USA

Minoru Taya  
Department of Mechanical and Aerospace Engineering  
University of Delaware  
Newark, DE 19716 USA

\* This research was supported in part under a contract from the Office of Naval Research, Contract No. N00014-85K-0007.

## Abstract

When a metal matrix composite is cooled down to room temperature from the fabrication or annealing temperature, residual stresses are induced in the composite due to the mismatch of the thermal expansion coefficients between the matrix and fiber.

An investigation was undertaken of the magnitude of the thermal residual stresses by determining the difference of the yield stresses ( $\Delta\sigma_y$ ) between tension and compression resulting from the thermal residual stresses. A theoretical model based on the Eshelby's method was then constructed for the prediction of the thermal residual stresses and  $\Delta\sigma_y$ . The agreement obtained was very good between the experimental results and the theoretical predictions.

## 1. Introduction

Metal matrix composites (MMCs), including eutectic composites, are becoming important in their application to structural components which are to be used at intermediate and high temperatures. When MMCs are fabricated at high temperature or annealed at a certain high temperature and cooled down to room temperature, it results in undesirable properties, such as low tensile yield and ultimate strengths. These results are mainly due to residual stresses that are caused by the mismatch of the thermal expansion coefficients between the matrix and fiber. This subject has been studied by a number of researchers (for examples see references 1-13). The residual stresses so induced have been observed in tungsten fiber/copper composites<sup>(7)</sup> and in SiC whisker/6061 Al composites<sup>(8,9)</sup>. Most of the models purposed to estimate the residual stress were based on one-dimensional analysis<sup>(1-3)</sup>, continuous fiber system<sup>(4,5)</sup>, or spherical particle system<sup>(10)</sup>.

The model is based on Eshelby's equivalent inclusion method<sup>(7)</sup>, which has been used to solve the problem of thermal residual stress<sup>(12-14)</sup>. The advantages of the Eshelby's model are that it can solve a three-dimensional composite system such as short whisker composite and also can take into account the effect of the volume fraction of fiber ( $V_f$ ) easily.

Eshelby's method has been also used for predicting the yield stress and work-hardening rate of metal matrix composites<sup>(15-19)</sup>. The effect of the thermally induced residual stress on the yield stresses has been discussed by Wakashima et al.<sup>(18)</sup> who predicted that the yield stress in compression ( $\sigma_y^c$ ) exceeds that in tension ( $\sigma_y^t$ ) for continuous B fiber/Al composites which were cooled down, although no comparison with the experimental data was made.

In this paper we focus on the residual stresses induced in a short whisker MMC due to the temperature drop and its effect on the yield stresses. The target MMC is aligned fiber MMC with a special emphasis on SiC whisker/6061 Al composite.

## 2. Experimental Procedure

### A. Materials

The target short fiber MMC was SiC whisker/6061 Al composite and was purchased from ARCO/SILAG. As a control MMC a SiC spherical 1100 Al composite was also purchased from ARCO/SILAG. The composite was in the form of an extruded rod 15.5 mm in diameter. Three different volume fractions of fiber (or whisker)  $V_f$  composites were used:  $V_f = 0, 0.05$  and  $0.2$ , and a composite with spherical SiC particles ( $0.5 \mu\text{m}$ ) in diameter having a volume fraction,  $V_s$ , equal to  $0.2$  was also used. All of the material was supplied as-fabricated (no heat treatment) condition, they then were machined into samples (Fig. 1a and 1b), annealed for 12 hours at 810 K, and then furnace cooled.

### B. Testing Methods

The tension and compression tests were performed in an Instron testing machine using a liquid metal container as the lower gripping device. This method of gripping was employed to ensure very good alignment of the sample. This test procedure is described in greater detail elsewhere<sup>(20)</sup>. Samples of two different gauge lengths were used to determine if there was a gauge length effect (there was none). The effective gauge length of the samples was determined by

glueing strain gauges on the center portion of the sample and comparing the results obtained from a clip on extensometer which was mounted into the "V" grooves. If the extensometer is mounted directly to the uniform gauge section, there is a high probability that the sample will fracture where the "knife" edge of the extensometer makes contact with the sample. Several tests in the low stress range were conducted using both the extensometer and the strain gauge; from these tests the effective gauge length was determined. Subsequent tests were conducted using only the extensometer. The samples, which were tested in the range from  $8 \times 10^{-5} \text{ sec}^{-1}$  to  $2 \times 10^{-3} \text{ sec}^{-1}$ , showed no effect on strain rate.

The conventional X-ray technique<sup>(21)</sup> was used first, but it was determined that there were problems when this technique was applied to discontinuous composites. The residual stress was determined by measuring the change in lattice parameters. There is an implicit assumption made, i.e., the matrix remains cubic.

### 3. Experimental Results

The stress-strain curves of the  $V_f = 0$ , 0.05 and 0.2 composites are plotted in Fig. 2a, 2b, and 2c, respectively. The solid and dashed curves denote the tensile and compressive test results, respectively. The yield stress was measured as 0.2% off set strain and is indicated in the figures by arrows.

The shapes of the stress-strain curves of the  $V_s = 0.2$  composites are very similar to those of whisker composites, except that the tension stress-strain curve is below that of the compression stress-strain curve. However, as in the case of  $V_f = 0$ , there was no difference in the stress-strain curves for tension and compression of  $V_s = 0$ .

The data obtained from the X-ray analysis is given in Table I, and it was observed that there is a small residual tensile stress in the matrix.

#### 4. Theoretical Procedure

The theoretical model used here is based on Eshelby's equivalent inclusion model. Mori and his co-workers<sup>(15-17)</sup> extended Eshelby's method to predict the yield stress ( $\sigma_y$ ) and work-hardening rate of aligned short whisker composites. Wakashima et al.<sup>(18)</sup> extended the above approach to predict  $\sigma_y$  by considering the mismatch of the thermal expansion coefficients of the matrix and fiber. Following the above models, Takao and Taya<sup>(14)</sup> have recently computed the stress field in and around a short fiber in a short fiber composite where the fiber is anisotropic both in stiffness and thermal expansion.

In this paper we focus on the average thermal residual stress induced in the matrix by the cool-down process and also the yield stresses in tension ( $\sigma_y^t$ ) and compression ( $\sigma_y^c$ ) when the composite is tested at the room temperature. The former case is essentially based on the model by Takao and Taya<sup>(14)</sup>, and as the latter case, we extend the model by Wakashima et al.<sup>(18)</sup> to account for the bi-linear stress-strain curve of the matrix.

##### A. Formulation

Consider an infinite body (D) which contains ellipsoidal whiskers ( $\Omega$ ) aligned along the  $x_3$ -axis (Fig. 3). This composite body D is subjected to the applied stress field  $\sigma_{ij}^0$ .

The stiffness tensors of the matrix ( $D-\Omega$ ) and fiber ( $\Omega$ ) are denoted by  $C_{ijkl}$  and  $C_{ijkl}^f$ , respectively. Following Eshelby, the transformation strain<sup>(11)</sup> or eigenstrain<sup>(22)</sup> is given in the fiber domain  $\Omega$  as  $\alpha_{ij}^*$ , where  $\alpha_{ij}^*$  is the strain due to the mismatch of the thermal expansion coefficients and the uniform plastic strain  $e_{ij}^p$  is prescribed in the matrix<sup>(15)</sup>. As far as the stress field is concerned, the model of Fig. 4 is equivalent to that of Fig. 3. Thus, the present problem is reduced to "inhomogeneous inclusions problem" (Fig. 4)<sup>(22)</sup>. The model of Fig. 4 will be used not only to predict the yield stresses and work-hardening rates, but also to compute the thermal residual stresses. For the latter case, we will set  $\sigma_{ij}^o = e_{ij}^p = 0$ .

Following the Eshelby's equivalent inclusion method modified for a finite volume fraction of fibers<sup>(22,23)</sup>, the total stress field in the fibers  $\sigma_{ij}^o + \sigma_{ij}$  is given by

$$\begin{aligned}\sigma_{ij}^o + \sigma_{ij} &= C_{ijkl}^f \{ e_{kl}^o + \tilde{e}_{kl} + e_{kl} - (\alpha_{kl} - e_{kl}^p) \} \\ &= C_{ijkl} \{ e_{kl}^o + \tilde{e}_{kl} + e_{kl} - (\alpha_{kl}^* - e_{kl}^p) - e_{kl}^* \} \quad (1)\end{aligned}$$

where

$$\sigma_{ij}^o = C_{ijkl} e_{kl}^o \quad \text{in } D \quad (2)$$

$$\langle \sigma_{ij} \rangle_m = C_{ijkl} \tilde{e}_{kl} \quad \text{in } D-\Omega \quad (3)$$

In Eq. (1),  $e_{kl}^*$  is the fictitious eigenstrain<sup>(23)</sup> which was introduced to connect the present problem to "inclusion problem" and  $\tilde{e}_{ij}$  is the average strain disturbance in the matrix and related to the average stress disturbance in the matrix  $\langle \sigma_{ij} \rangle_m$  by Eq. (3).  $\langle \sigma_{ij} \rangle_m$  is defined by

$$\langle \sigma_{ij} \rangle_m = \frac{1}{V_{D-\Omega}} \int_{D-\Omega} \sigma_{ij} dv \quad (4)$$

where  $V_{D-\Omega}$  is the total volume of the matrix and  $\sigma_{ij}$ , and  $e_{ij}$  in Eqs. (1) and (4) is the stress and strain disturbance, respectively, by a single fiber  $\Omega$  when it is embedded in an infinite matrix. Since the stress disturbance when it is integrated in the entire domain  $D$  vanishes,

$$\int_D \sigma_{ij} dv = 0 \quad (5)$$

The stress disturbance  $\sigma_{ij}$  is obtained from Eqs. (1) and (2)

$$\sigma_{ij} = C_{ijkl} (\tilde{e}_{kl} + e_{kl}^* - e_{kl}^{**}) \quad (6)$$

where

$$e_{kl}^{**} = e_{kl}^* + e_{kl}^p - e_{kl}^p \quad (7)$$

From Eqs. (3), (5) and (6), we obtain

$$\tilde{e}_{ij} = - V_f (e_{ij} - e_{ij}^{**}) \quad (8)$$

According to Eshelby,  $e_{ij}$  is related to the total eigenstrain  $e_{kl}^{**}$  as

$$e_{ij} = S_{ijkl} e_{kl}^{**} \quad (9)$$

where  $S_{ijkl}$  is the Eshelby's tensor and a function of  $C_{ijkl}$ ,  $C_{ijkl}^f$  and the geometry of the ellipsoidal fiber<sup>(23)</sup>. The fiber is assumed as a prolate spheroid, hence the fiber aspect ratio  $\ell/d$  is a single geometrical parameter. For simplicity, we assume that the matrix and fiber are isotropic both in stiffness and thermal expansion coefficient. Thus,  $C_{ijkl}$ ,  $C_{ijkl}^f$  and  $\alpha_{ij}^*$  are given by

$$C_{ijkl} = \lambda \delta_{ij} \delta_{kl} + \mu (\delta_{ik} \delta_{jl} + \delta_{il} \delta_{kj}) \quad (10)$$

$$C_{ijkl}^f = \lambda^f \delta_{ij} \delta_{kl} + \mu^f (\delta_{ik} \delta_{jl} + \delta_{il} \delta_{kj}) \quad (11)$$

$$\alpha_{ij}^* = - (\alpha_f - \alpha) \delta_{ij} \Delta T \quad (12)$$

In the above equations,  $\delta_{ij}$  is the Kronecker's delta,  $\lambda$  ( $\lambda^f$ ) and  $\mu$  ( $\mu^f$ ) are Lame's constants of the matrix (fiber),  $\alpha$  ( $\alpha_f$ ) is the thermal expansion coefficient of the matrix (fiber) and  $\Delta T$  is the change in temperature ( $\Delta T > 0$  corresponds to the temperature drop).

The stress field in the fiber is obtained from Eqs. (6), (8), (9) and (10)

$$\sigma_{ij} = (1 - v_f) \{ (S_{kkmn} e_{mn}^{**} - e_{kk}^{**}) \lambda \delta_{ij} + 2\mu (S_{1jmn} e_{mn}^{**} - e_{1j}^{**}) \} \quad (13)$$

where the repeated index is to be summed over 1, 2, and 3. After solving for  $e_{1j}^{**}$  in Eq. (1) by use of Eqs. (8) and (9), we can compute the stress disturbance  $\sigma_{ij}$  in the fiber from Eq. (13).

#### B. Yield stresses $\sigma_y^t$ , $\sigma_y^c$ and work-hardening rate

The method of computing the yield stresses  $\sigma_y^t$  and  $\sigma_y^c$  and the work-hardening rate of the composite is described briefly. The total potential energy of Fig. 3,  $U$ , is given by

$$U = \frac{1}{2} \int_D (\sigma_{ij}^0 + \sigma_{ij}) (u_{ij}^0 + \tilde{u}_{ij} + u_{ij} - e_{ij}^p - \alpha_{ij}^*) dV - \int_{\partial D} \sigma_{ij}^0 n_j (u_1^0 + \tilde{u}_1 + u_1) dS \quad (14)$$

where  $u_1^0$ ,  $\tilde{u}_1$  and  $u_1$  are the displacement components corresponding to  $e_{ij}^0$ ,  $\tilde{e}_{ij}$  and  $e_{ij}$ , respectively; the index  $j$  preceded by a comma denotes a partial differentiation with respect to  $x_j$ ;  $\partial D$  is the boundary of  $D$ ; and  $n_j$  is the  $j$ -th component of an unit vector outer normal to  $\partial D$ . Then, the change in  $u$  due to the change in the plastic strain  $\delta e_{ij}^p$  is given by

$$\delta U = - \int_D (\sigma_{ij}^0 + \sigma_i) \delta e_{ij}^p dV \quad (15)$$

In the above derivation, the Gauss' divergence theory and the following equation were used

$$\int_D \sigma_{ij} (\delta \tilde{u}_{i,j} + \delta u_{i,j}) dV = 0$$

Noting that the plastic strain exists only in the matrix ( $D-\Omega$ ), Eq. (15) is reduced to

$$\delta U = - \delta e_{ij}^p \{ (1-v_f) \sigma_{ij}^0 - v_f \sigma_{ij} \} \quad (16)$$

Under the uniaxial stress along the  $x_3$ -axis ( $\sigma_0$ ),  $\sigma_{ij}^0$  and  $e_{ij}^p$  are given by

$$\sigma_{ij}^0 = \begin{Bmatrix} 0 \\ 0 \\ \sigma_0 \\ 0 \\ 0 \\ 0 \end{Bmatrix} \quad e_{ij}^p = \begin{Bmatrix} -1/2 e_p \\ -1/2 e_p \\ e_p \\ 0 \\ 0 \\ 0 \end{Bmatrix} \quad (17)$$

where the six components of  $\sigma_{ij}^0$  and  $e_{ij}^p$  are expressed in the order of  $(ij) = 11, 22, 33, 23, 31, \text{ and } 12$ , and  $e_p$  is the plastic strain along the  $x_3$ -axis. On the other hand, the energy dissipation due to the plastic work in the matrix,  $\delta Q$ , is given by

$$\delta Q = (1-v_f) \sigma_y^0 \delta e_p \quad (18)$$

where  $\sigma_y^0$  is the flow stress of the matrix for the bilinear model

$$\sigma_y = \sigma_y^0 + E_T (e - e_p) \quad (19)$$

where  $\sigma_y^0$  and  $E_T$  are the initial yield stress and tangent modulus of the matrix, respectively, and  $e$  is the total strain. Since  $\delta U + \delta Q = 0$ , we obtain

$$\sigma_o = \sigma_y^0 + \frac{V_f}{(1-V_f)} (\sigma_{33} - \sigma_{11}) \quad (20)$$

In the above derivation,  $\sigma_{11} = \sigma_{22}$ ,  $e_{11}^p = e_{22}^p = -\frac{1}{2} e_p$  were used. Combining the solutions of  $\sigma_{1j}$  in Eq. (13) and Eq. (20), we can obtain the yield stress of the composite in tension ( $\sigma_y^t = \sigma_o$ ) and that in compression ( $\sigma_y^c = \sigma_o$ ) as

$$\frac{\sigma_y^t}{\sigma_y^0} = C_0 + C_1 \alpha_m \Delta T \quad (21)$$

$$\frac{\sigma_y^c}{\sigma_y^0} = C_0 - C_1 \alpha_m \Delta T$$

Similarly, the work-hardening rate of the composite,  $\bar{E}_T$  is obtained as

$$\frac{\bar{E}_T}{E_T} = C_2 + C_3 \left( \frac{E_T}{E} \right) \quad (22)$$

In the above equations,  $C_0$ ,  $C_1$ ,  $C_2$ , and  $C_3$  are functions of

the mechanical properties of the matrix and fiber and the fiber aspect ratio  $\ell/d$ ,  $E$  is the Young's modulus of the matrix.

### C. Thermal Residual Stress

When the composite is cooled down by  $\Delta T$ , the thermal residual stress is induced in the composite. The theoretical model for this problem is the same as that shown in Fig. 4 except that  $\sigma_{ij}^0 = e_{ij}^p = 0$  in the present case. Hence, the formulation up to Eq. (13) is valid and will be used to compute the thermal residual stress. Once the stress within the fiber  $\sigma_{ij}^{(in)}$  is computed, the stresses just outside the fiber  $\sigma_{ij}^{(out)}$  can be obtained by the following relation<sup>(13)</sup>

$$\sigma_{pq}^{(out)} = \sigma_{pq}^{(in)} + C_{pqmn} \left\{ -C_{klij} e_{ij}^{**} n_l n_m \frac{(\lambda+2\mu)\delta_{km} - (\lambda+\mu)n_k n_m}{\mu(\lambda+2\mu)} \right. \\ \left. + e_{mn}^{**} \right\} \quad (23)$$

where  $\sigma_{pq}^{(in)}$  is given by Eq. (13),  $e_{ij}^{**}$  is solved by Eq. (1),  $\lambda$  and  $\mu$  are previously defined and  $n_i$  is the  $i$ -th component of the unit vector perpendicular to the surface of the fiber. If one wants to compute the stresses just outside the equator of the ellipsoidal fiber where  $n = (1, 0, 0)$ , we can obtain the stresses in polar coordinates,  $\sigma_r$ ,  $\sigma_\theta$  and  $\sigma_z$  there as

$$\sigma_r^{(out)} = \sigma_r^{(in)}$$

$$\sigma_\theta^{(out)} = \sigma_\theta^{(in)} + 2\mu \left\{ \frac{1}{1-\nu} e_{11}^{**} + \frac{\nu}{1-\nu} e_{33}^{**} \right\} \quad (24)$$

$$\sigma_z^{(out)} = \sigma_z^{(in)} + 2\mu \left\{ \frac{\nu}{1-\nu} e_{11}^{**} + \frac{1}{1-\nu} e_{33}^{**} \right\}$$

where  $\nu$  is the Poisson's ratio of the matrix.

Next the average stress field in the matrix,  $\langle \sigma_{ij} \rangle_m$ , can be also obtained from Eqs. (3), (8) and (9) as

$$\langle \sigma_{ij} \rangle_m = - V_f C_{ijkl} (S_{klmn} e_{mn}^{**} - e_{kl}^{**}) \quad (25)$$

The average stress in the matrix,  $\langle \sigma_r \rangle_m$ ,  $\langle \sigma_\theta \rangle_m$  and  $\langle \sigma_z \rangle_m$ , will be computed by setting  $ij = 11, 22$ , and  $33$  in Eq. (25). It should be noted here that  $\langle \sigma_r \rangle_m = \langle \sigma_\theta \rangle_m$  due to the assumptions of an aligned short fiber composite which results in the transverse isotropy of the volume average quantity.

## 5. Theoretical Results

We will apply the present theoretical model to two types of MMCs, short fiber MMC (SiC whisker/6061 Al) and continuous fiber MMC ( $\text{Al}_2\text{O}_3-\gamma$ /5056 Al).

### A. Short Fiber MMC

The thermo-mechanical data of the matrix and whisker for the theoretical calculations are obtained from the stress-strain curve of the matrix (Fig. 2a) and the material properties handbook.

Annealed 6061 Al matrix (bilinear model):

$$\begin{aligned}
 E &= 47.5 \text{ GPa} \\
 E_T &= 2.3 \text{ GPa} \\
 \sigma_y^0 &= 47.5 \text{ MPa} \\
 v &= 0.33 \\
 \alpha &= 23.6 \times 10^{-6}/\text{K}
 \end{aligned} \tag{26}$$

SiC Whisker:

$$\begin{aligned}
 E_w &= 427 \text{ GPa} \\
 v_w &= 0.17 \\
 \alpha_w &= 4.3 \times 10^{-6}/\text{K} \\
 l/d &= 1.8
 \end{aligned} \tag{27}$$

where the average value of the fiber aspect ratio ( $l/d$ ) was

used<sup>(24)</sup> and the bilinear stress strain curve of the matrix is indicated by a dash-dot line in Fig. 2a. The temperature drop  $\Delta T$  is defined as

$$\Delta T = T_1 - T_0 \quad (28)$$

where  $T_1$  is taken as the temperature below which dislocation generation is minimal during the cooling process<sup>(9)</sup> and  $T_0$  is the room temperature. Thus, for the present composite system  $\Delta T$  is set equal to 200 K.

The theoretically predicted  $\sigma_y^c$  and  $\sigma_y^t$  can be obtained from Eq. (21). The differences between  $\sigma_y^c$  and  $\sigma_y^t$  ( $\sigma_y^c - \sigma_y^t$ ) for various  $V_f$  are shown as the solid line in Fig. 5. The differences between  $\sigma_y^c$  and  $\sigma_y^t$  increase with increasing  $V_f$ . The experimentally determined differences between  $\sigma_y^c$  and  $\sigma_y^t$  are represented by the open circles in Fig. 5. The experimental values of the yield stresses are taken as the stresses 0.2% off-set strain. It follows (Fig. 5) that good agreement is obtained between the experimental and theoretical results of the difference in the compressive tensile yield stresses. However, the experimental values of  $\sigma_y^c$  are greater than the theoretical values of  $\sigma_y^c$ , and similarly the experimental values of  $\sigma_y^t$  are greater than the theoretical values of  $\sigma_y^t$ .

From the data given by Eqs. (26) - (27) and the use of Eq. (25), we have computed the stresses, and its average value in the matrix and plotted schematically the  $\sigma_L$  (solid curve) and  $\langle \sigma_L \rangle_m$  (dashed curve) along the  $x_2$  and  $x_3$  axes in

Fig. 6.

Next, the thermal residual stresses averaged in the matrix of the SiC whisker/6061 Al are predicted by Eq. (25) and the results on  $\langle \sigma_T \rangle_m$  and  $\langle \sigma_L \rangle_m$  are plotted in Fig. 7 as a function of the volume fraction of whisker ( $V_f$ ), where the subscripts, T and L denote the component along the transverse direction (r and  $\theta$ ) and longitudinal direction (z). The average theoretical thermal-residual stress is predicted to be tensile in nature. This theoretical prediction is in general agreement with the experimental results (Table I). Also, the residual stress is experimentally observed to be larger in the transverse direction and a larger transverse stress is shown in Fig. 7.

For the case of spherical SiC composites the procedure for obtaining the difference in  $\sigma_y^c$  and  $\sigma_y^t$  is identical to the whisker case, with one exception, i.e.,  $\lambda/d = 1$  in the spherical case. The theoretically predicted difference between  $\sigma_y^c$  and  $\sigma_y^t$  for  $V_s = 0.2$  is zero, but experimentally it was observed that  $\sigma_y^c$  was slightly greater than  $\sigma_y^t$  by  $\sim 13$  MPa.

#### B. Continuous Fiber MMC

The present model is also applied to continuous fiber ( $\text{Al}_2\text{O}_3-\gamma$ ) reinforced 5056 Al composite with  $V_f = 0.5$  ( $\text{Al}_2\text{O}_3-\gamma/5056$  Al in short abbreviation) to predict the yield stress in tension and compression, and also the work-hardening rate.

The material properties of the matrix metal and fiber are:

Annealed 5056 Al matrix (bilinear model):

$$E = 72.4 \text{ GPa}$$

$$E_T = 6.25 \text{ GPa}$$

$$\sigma_y^0 = 152 \text{ MPa} \quad (29)$$

$$\nu = 0.33$$

$$\alpha = 23.6 \times 10^{-6}/\text{K}$$

$\text{Al}_2\text{O}_3-\gamma$  Fiber<sup>(26)</sup>

$$E_f = 210 \text{ GPa}$$

$$\nu_f = 0.2$$

$$\alpha_f = 8.8 \times 10^{-6}/\text{K}$$

In this computation  $\Delta T = 200 \text{ K}$  was used.

Figure 8 shows a comparison between the experimental results<sup>(25)</sup> (solid curve and filled circle) and the theoretical ones (dashed curve and open circle) where both filled and open circles denote the yield stresses. It follows from Fig. 8 that the yield stress and the work-hardening rate of the compressive stress-strain curve are well predicted by the present model, while for the tensile yield stress, the present model underestimates the experimental results.

AD-A164 838

COMPOSITE STRENGTHENING(U) MARYLAND UNIV COLLEGE PARK  
ENGINEERING MATERIALS GROUP R J ARSENault 1985  
N00014-85-K-0007

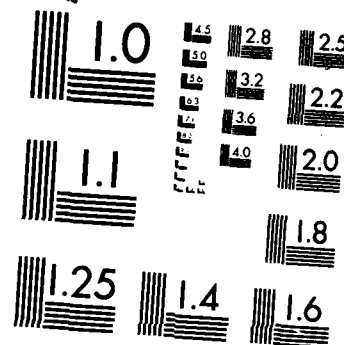
2/2

UNCLASSIFIED

F/G 11/4

ML

11C  
11M01  
11M02  
11M03



MICROCOPY RESOLUTION TEST CHART  
NATIONAL BUREAU OF STANDARDS-1963-A

## 6. Discussion

The theoretical predictions and experimental results are in very good agreement in most cases.

The theoretical model is based on an extension of previous work by Eshelby<sup>(11)</sup>, Mura and Taya<sup>(13)</sup>, Tanaka and Mori<sup>(15)</sup>, and Wkashima, et al.<sup>(18)</sup> and it can predict the yield stress in tension and compression and the thermal residual stress. The predicted values of the yield stress of the whisker composite in tension and compression are less than the experimentally determined values of the yield stress in tension and compression. This difference between the theoretical and experimental stresses is due to the fact that the  $V_w = 0$  curves of stress vs. strain were used for the matrix in the composite cases. It has been demonstrated by Arsenault and Fisher<sup>(8)</sup> and Vogelsang, et al.<sup>(9)</sup> that there is a much higher dislocation density in the annealed composite matrix than in the  $V_f = 0$  material. Therefore, the matrix is stronger than the annealed  $V_f = 0$  matrix alloy. However, this increase in matrix strength due to a higher dislocation density does not influence the difference in yield stress in the compression vs. tension. The theoretical prediction is that the yield stress of the whisker composite in compression should be higher than the yield stress in tension, and this is exactly what is observed experimentally, due to an average residual tension stress in the sample. This residual stress reduces the yield stress in tension and

increases the yield stress in compression.

The theoretical prediction that the compressive yield stress is higher than the tensile yield stress suggests that a tensile residual stress exists in the matrix of composite. An average tensile residual stress is predicted in the matrix as shown in Figs. 6 and 7.

Though the present model is based on the assumption that all fibers are aligned along a specified direction (the  $x_3$ -axis in Fig. 3), SiC whiskers in SiC whisker/6061 Al composites are misoriented. The misorientation of these whiskers is observed to be enhanced as  $V_f$  decreases. Thus the values of  $\sigma_y^t$  and  $\sigma_y^c$  predicted by the present model tends to overestimate the actual values. The fiber aspect ratio ( $l/d$ ) of SiC whiskers has been observed to be variable<sup>(24)</sup>, i.e.,  $0.5 < l/d < 25$  with most of  $l/d$  being around 1. In the present model we have used the average value of  $l/d$ , 1.8 to predict the yield stress and work-hardening rate of the composite. Takao and Taya<sup>(26)</sup> have recently examined the effect of variable fiber aspect ratio on the stiffness and thermal expansion coefficients of a short fiber composite and concluded that the results predicted by using the average value of  $l/d$  are not much different from those of using actual variable aspect ratio unless the distribution of  $l/d$  is extraordinarily scattered. Thus, the use of the average value of  $l/d$  in the present model can be justified.

The present model is strongly dependent on  $\Delta T$  ( $= T_1 - T_0$ ) as it appears in Eqs. 12, 21 and 22. A choice of  $T_1$  was made by noting the movement of dislocation generation being minimal<sup>(9)</sup> as discussed before. If temperature  $T_1$  can be continued to correspond to the temperature  $T_r$  above which the relaxation of internal stress is highly promoted and below which the deformation of the matrix metal is basically controlled by elastic and time-independent plastic behavior, then the present model which is based on an elastic/time-independent plasticity becomes valid. If  $T_1$  is not approximately equal to  $T_r$ , a more refined model to account for elastic/time-independent plastic/creep behavior of the matrix metal during a temperature excursion from  $T_1$  to  $T_0$  must be employed. Such a model for one-dimensional stress analysis has been proposed by Garmong<sup>(27)</sup>.

## 7. Conclusions

It is possible to arrive at the following conclusions from the theoretical model of the thermal residual stresses and the experimental results.

1. The theoretical model predicts a higher compression yield stress than tensile yield stress for the whisker composite, which is in agreement with the experimental results. The higher compressive yield stress is due to a tensile residual stress. This residual stress is due to the difference in coefficient of thermal expansion between fiber and matrix.
2. The absolute magnitude of the predicted yield stress (tensile and compressive) is less than the experimental yield stress due to an increase in matrix strengthening. The increased matrix strength is due to a higher dislocation density in the matrix; the higher dislocation density is a consequence of the difference in coefficient of thermal expansion between the Al alloy matrix and the SiC.
3. The residual stress, in the region between SiC whiskers, is tensile and this is the likely region where plastic deformation would begin. For in this region the matrix contains a lower dislocation density than adjacent to the SiC whisker, i.e., in this region the matrix is weaker.

4. The theoretical model predicts that the compressive yield stress should equal the tensile yield stress for composites containing spherical SiC. Experimentally it is observed that the tensile yield stress is slightly larger than the compressive yield stress.
5. The present model can predict the yield stress and work-hardening rate of continuous  $\text{Al}_2\text{O}_3$ - $\gamma$  fiber/5056 Al composite reasonably well except for  $\sigma_y^t$ .
6. In the short fiber case, the theoretical model predicts that the matrix should be in tension and experimental X-ray data confirms this prediction.

References

1. E. R. Thompson, D. A. Koss, and J. C. Chestnutt, Metall. Trans. 1, 2807 (1970).
2. D. A. Koss and S. M. Copley, Metall. Trans. 2, 1557 (1971).
3. J. K. Lees, Polymer Eng. Sci. 8, 195 (1968).
4. S. S. Hecker, C. H. Hamilton and L. J. Ebert, J. Mater. Sci. 5, 868 (1970).
5. J. Gayda and L. J. Ebert, Metall. Trans. 10A, 349 (1979).
6. S. D. Tsai, D. Mahulikar, H. L. Marcus, I. C. Noyan and J. B. Cohen, Mater. Sci. & Eng. 47, 145 (1981).
7. K. K. Chawla and M. Metzger, J. Mater. Sci. 7, 34 (1972).
8. R. J. Arsenault and R. M. Fisher, Scripta Metall. 17, 67 (1983).
9. M. Vogelsang, R. J. Arsenault, and R. M. Fisher, submitted for publication.
10. J. K. Lee, Y. Y. Earmme, H. I. Aaronson and K. C. Russell, Metall. Trans. 11A, 1837 (1980).
11. J. D. Eshelby, Proc. Roy. Soc. London A241, 376 (1957).
12. K. Wakashima, M. Otsuka and S. Umekawa, J. Comp. Mater. 8, 391 (1976).
13. T. Mura and M. Taya, Proc. of the 2nd U.S.-Japan Conf. on Comp. Mater. ASTM, under review.
14. Y. Takao and M. Taya, J. Appl. Mech., under review.
15. K. Tanaka and T. Mori, Acta Metall. 18, 931 (1970).
16. K. Tanaka, K. Wakashima and T. Mori, J. Mech. Phys. Solids 21, 207 (1973).
17. S. C. Lin, T. Mura, M. Shibata and T. Mori, Acta Metall. 21, 505 (1973).
18. K. Wakashima, S. Kurihara and S. Umekawa, Japan Soc. Comp. Mater. 2, 1 (1976).

19. A. Daimaru and M. Taya, Proc. of the 4th Intl. Conf. on Comp. Materials, Edited by Hayashi et al., Japan Soc. Comp. Materials, Tokyo (1982), p. 199.
20. R. Hsu and R. J. Arsenault, Mat. Sci. & Eng. 66, 35 (1984).
21. J. B. Cohen, Diffraction Methods in Materials Science, MacMaillan Series in Materials Science, 1966.
22. T. Mura, Micromechanics of Defects in Solids, Martinus Nijhoff Publishers, 1982.
23. T. Mori and K. Tanaka, Acta Metall. 21, 571 (1973).
24. R. J. Arsenault, Mater. Sci. & Eng. 64, 171 (1984).
25. Private communication with Y. Abe, Sumito Chemical Co., Japan.
26. Y. Takao and M. Taya, submitted for publication.
27. G. Garmong, Metall. Trans. 15, 2183 (1974).

Table I  
Thermal Residual Stress (Tensile)  
X-Ray Measurements

Material	Transverse MPA	Longitudinal MPA
0 V% Whisker SiC 6061 Matrix	0.0	0.0
5 V% Whisker SiC 6061 Matrix	408	35
20 V% Whisker SiC 6061 Matrix	231	58
Wrought 1100 Al	0.0	0.0

### Figure Captions

Figure 1 A schematic diagram of the sample configuration which was used in the tension and compression testing. The dimensions are in millimeters.

Figure 2a The absolute stress vs. strain curves for tension and compression test of 0 volume % whisker material in the annealed condition.

Figure 2b The absolute value of stress vs. strain for 5 volume % whisker composite in the annealed condition.

Figure 2c The absolute value of the stress as a function of strain for 20 volume % whisker material in the annealed condition.

Figure 3 Theoretical model; actual case.

Figure 4 The equivalent inclusion model converted from Figure 3.

Figure 5 The difference in yield stress between compression and tensin as a function of volume % silicon carbide whisker.

Figure 6 A schematic of the stress distribution in the matrix and in the reinforcement due to the difference in thermal coefficient of expansion between the silicon-carbide and aluminum.

Figure 7 Predicted residual stress in the matrix for the transverse and longitudinal directions.

Figure 8 Tension and compression stress-strain curves of continuous  $\text{Al}_2\text{O}_3$ - $\gamma$  fiber/5056 Al composite with  $V_f = 0.5$ <sup>(26)</sup>. The experimental and theoretical results are denoted by solid dashed curves, respectively. The filled and open circles denote the yield stress of the experimental and theoretical results, respectively.

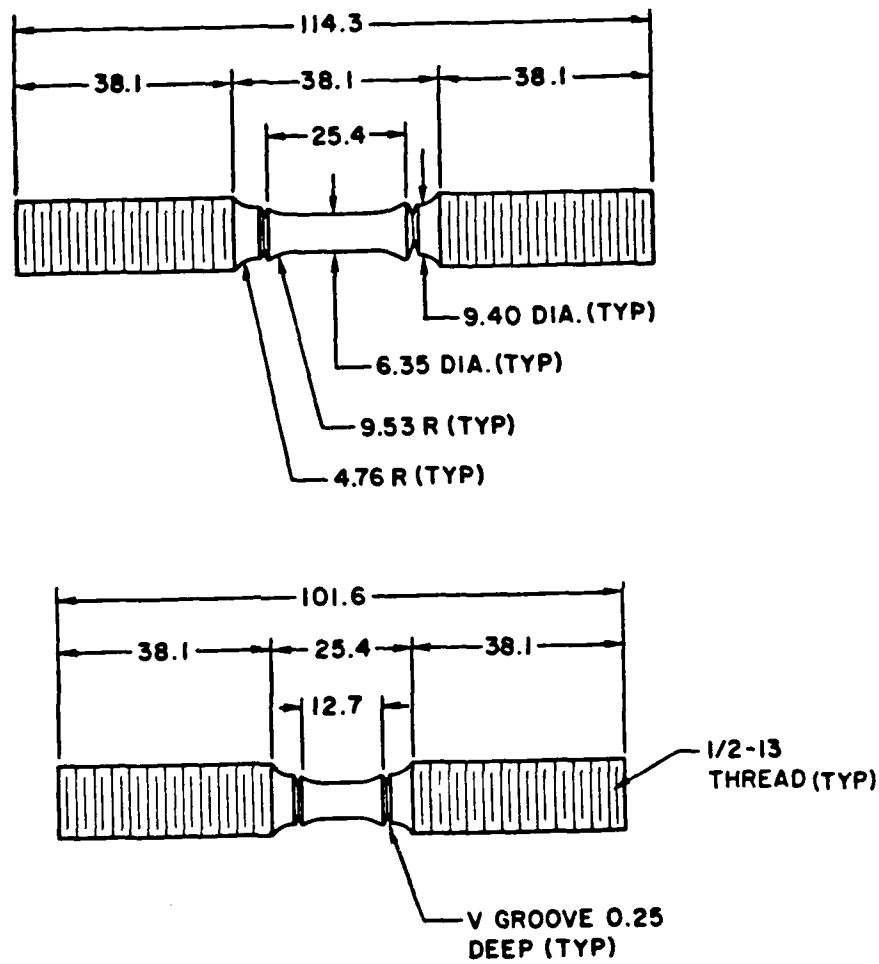


Figure 1 A schematic diagram of the sample configuration which was used in the tension and compression testing. The dimensions are in millimeters.

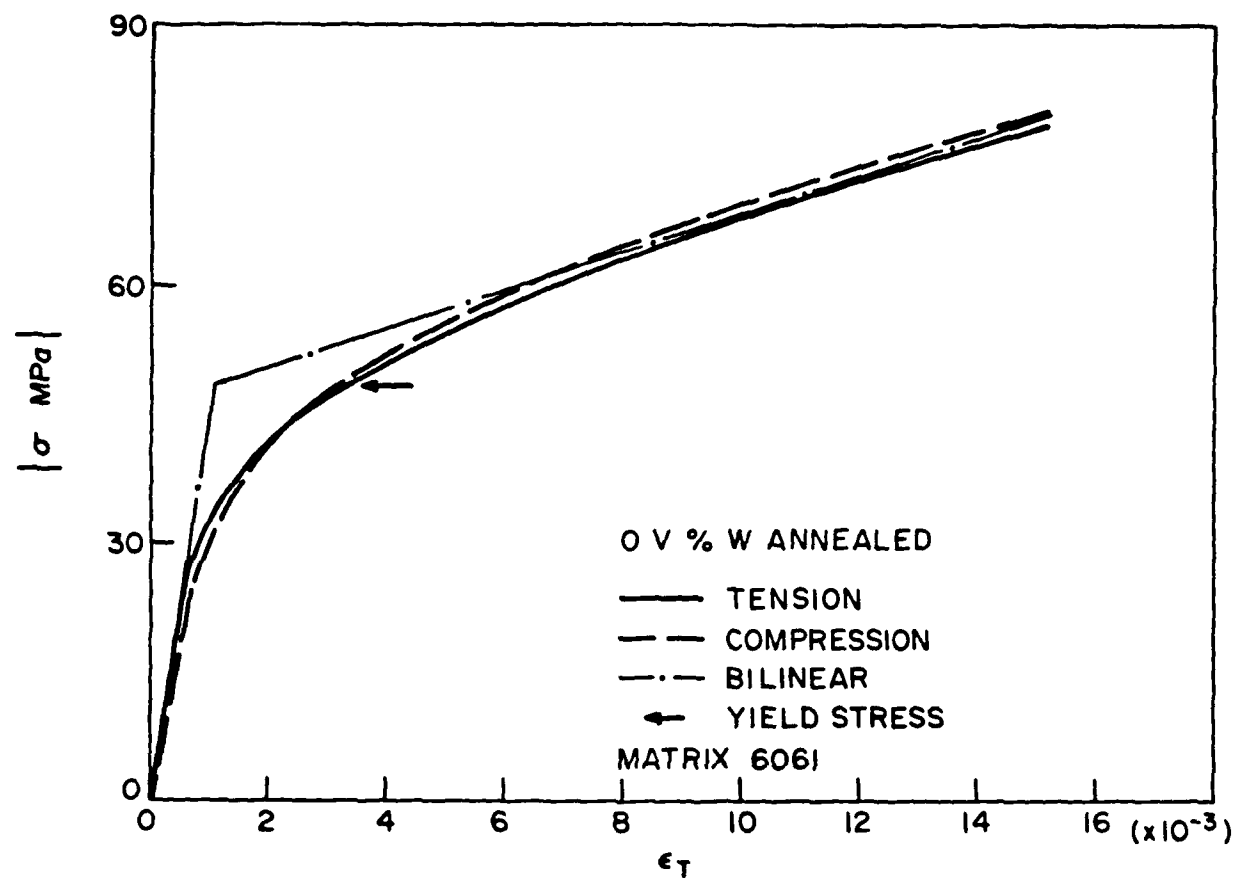


Figure 2a The absolute stress vs. strain curves for tension and compression test of 0 volume % whisker material in the annealed condition.

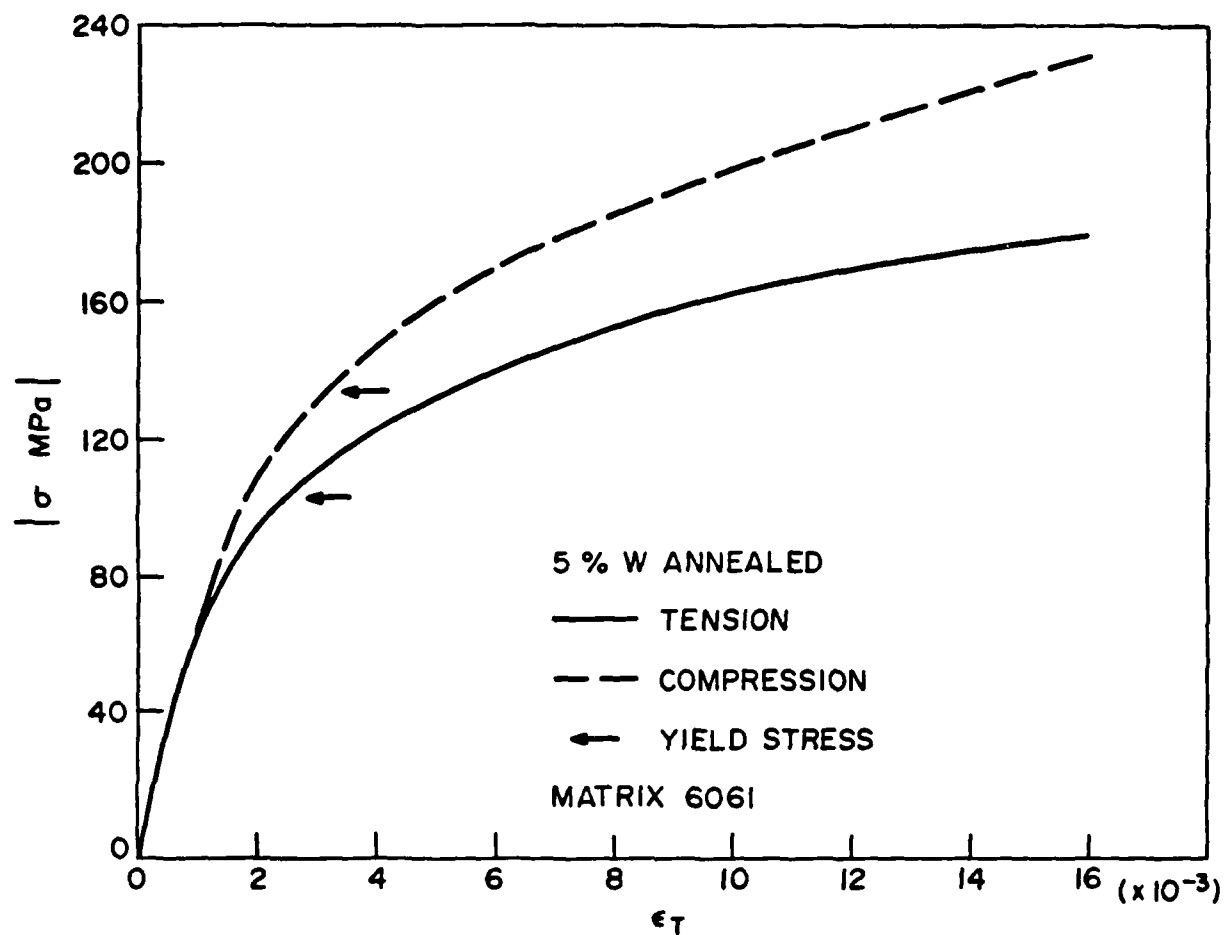


Figure 2b The absolute value of stress vs. strain for 5 volume % whisker composite in the annealed condition.

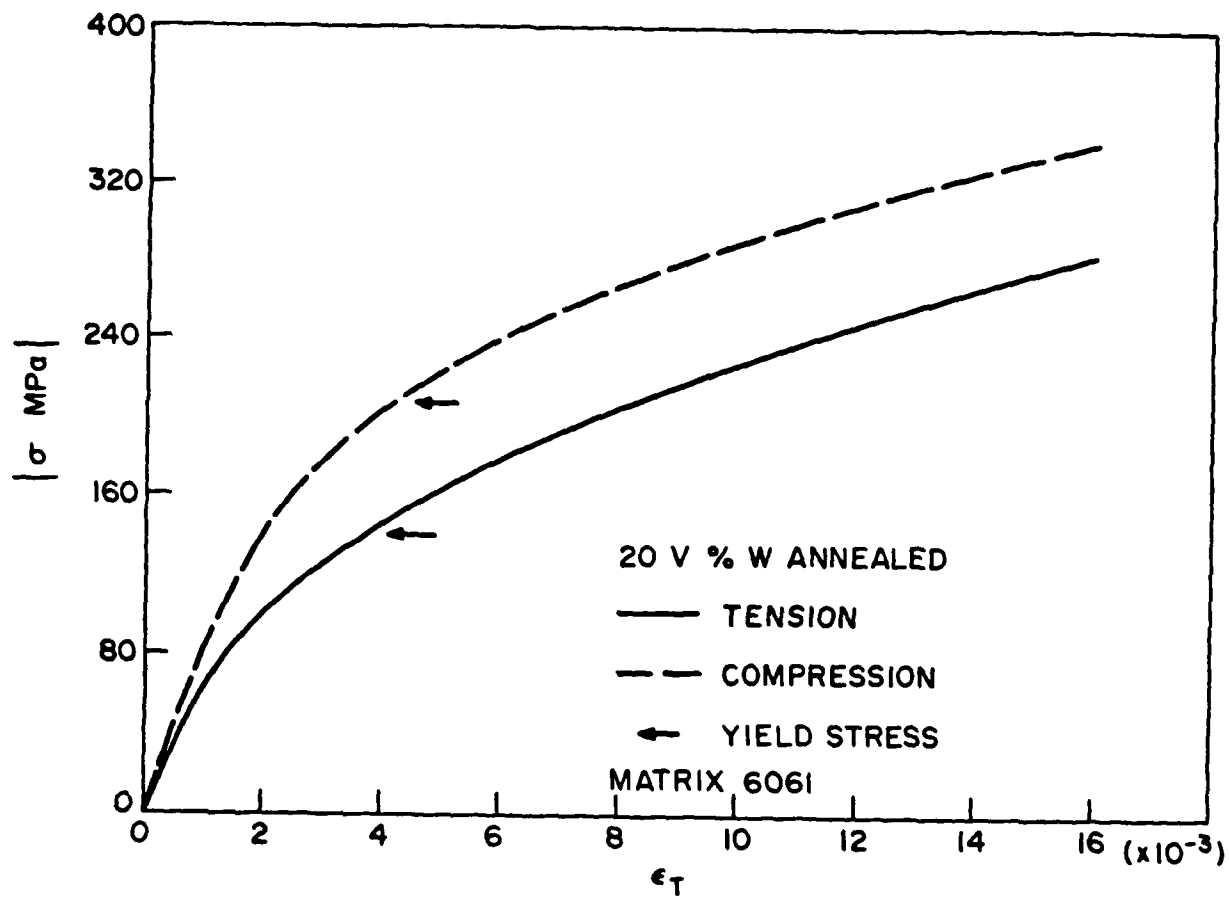


Figure 2c The absolute value of the stress as a function of strain for 20 volume % whisker material in the annealed condition.

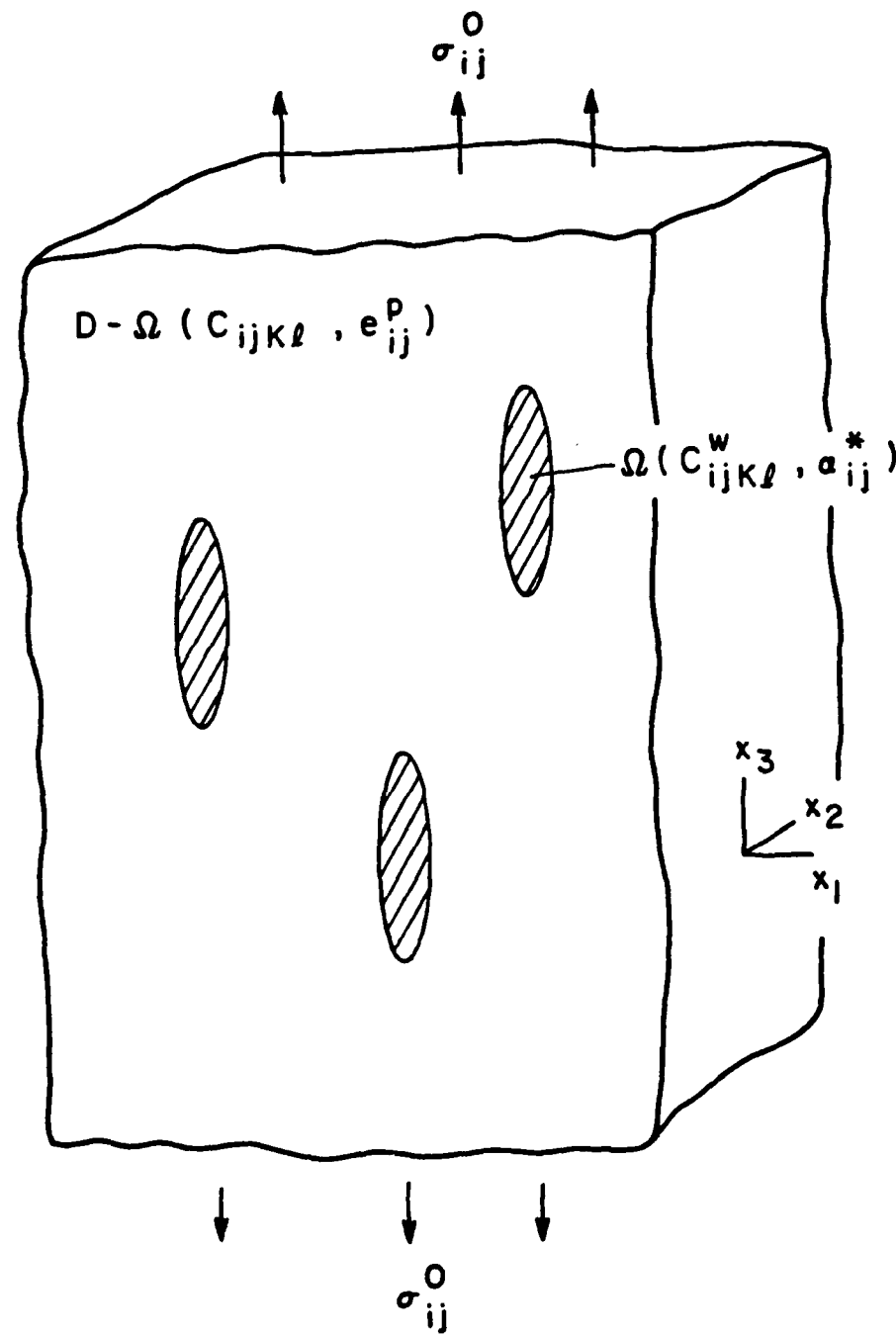


Figure 3 Theoretical model; actual case.

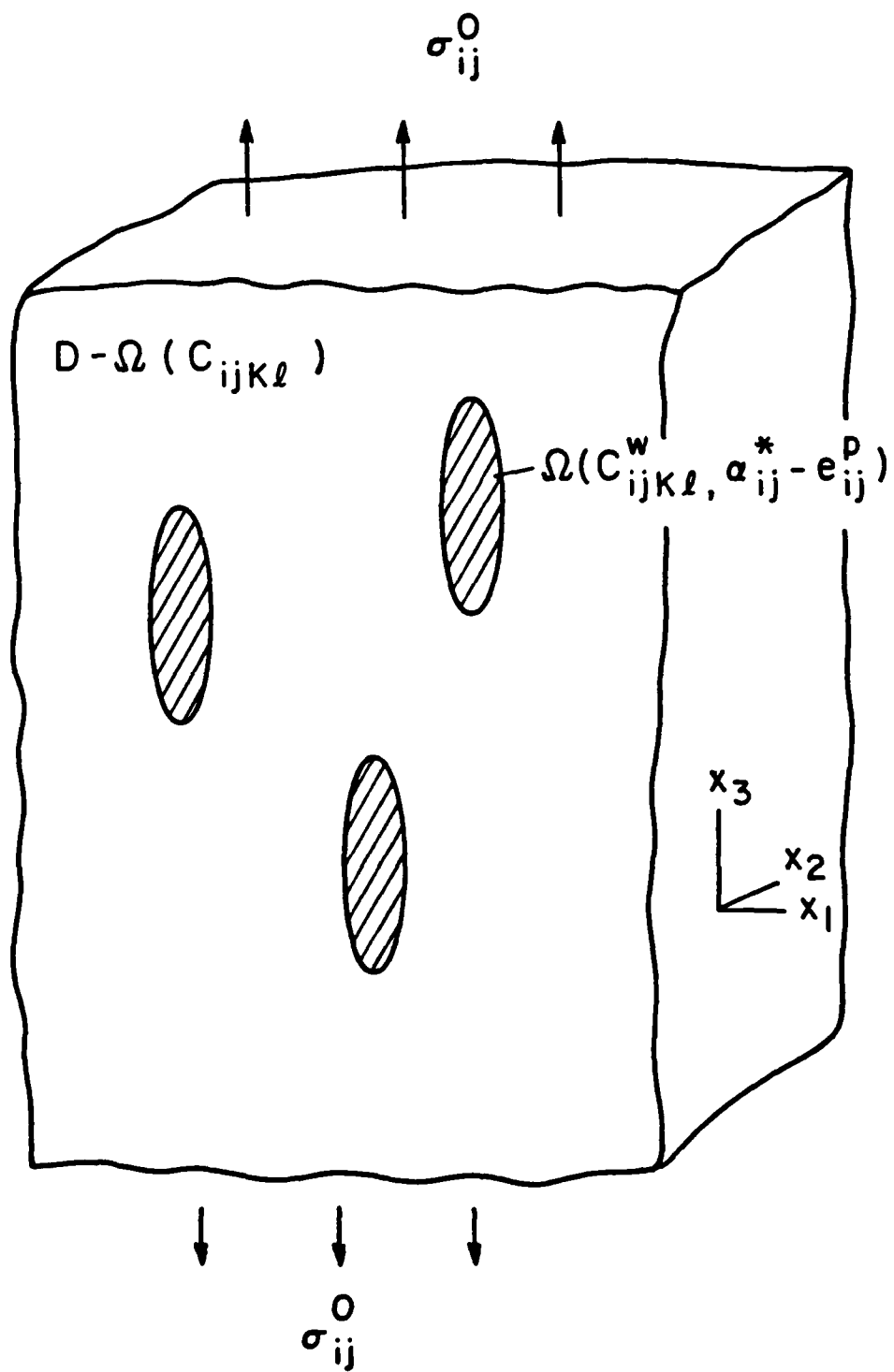


Figure 4 The equivalent inclusion model converted from Figure 3.

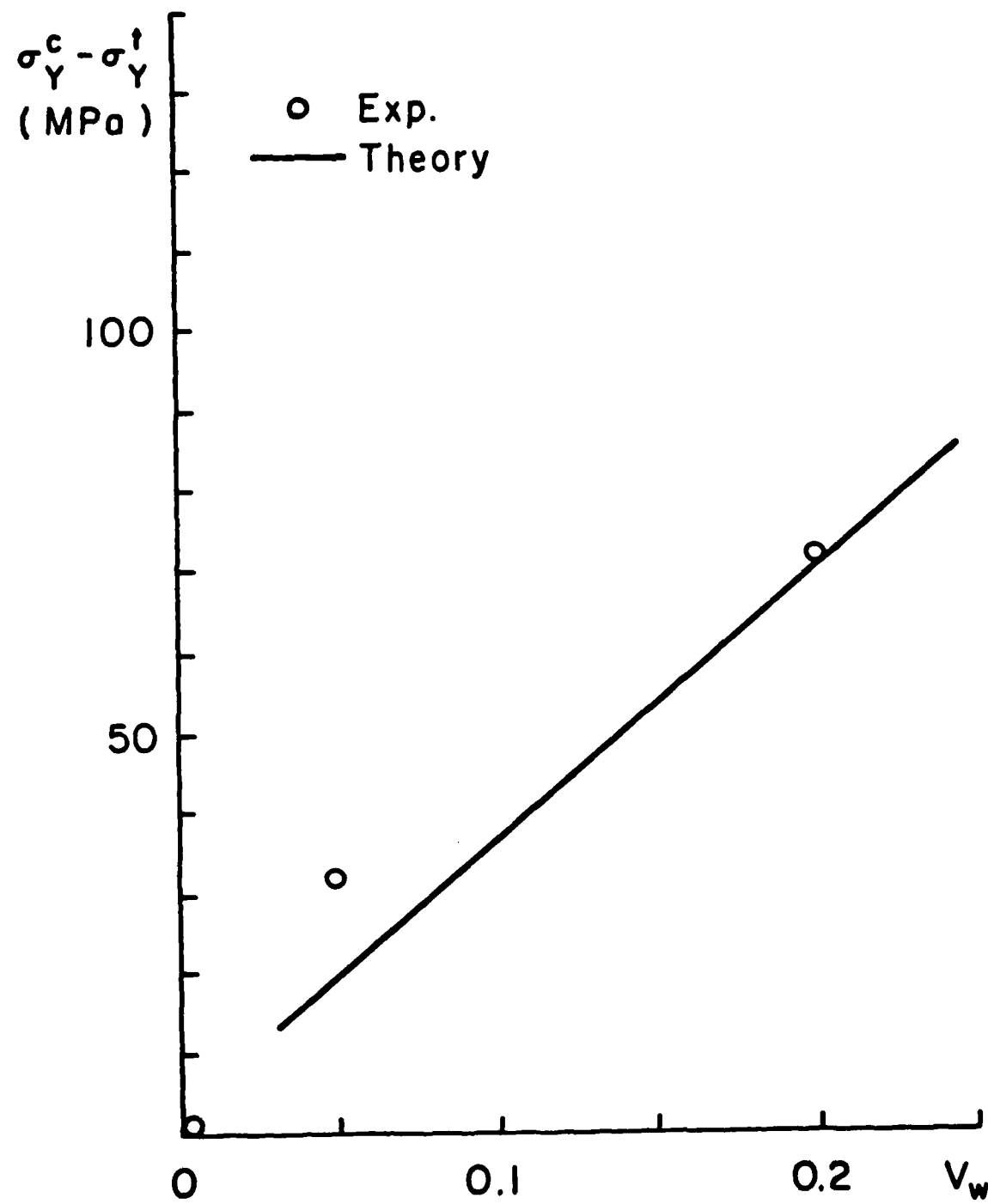


Figure 5 The difference in yield stress between compression and tension as a function of volume % silicon carbide whisker.

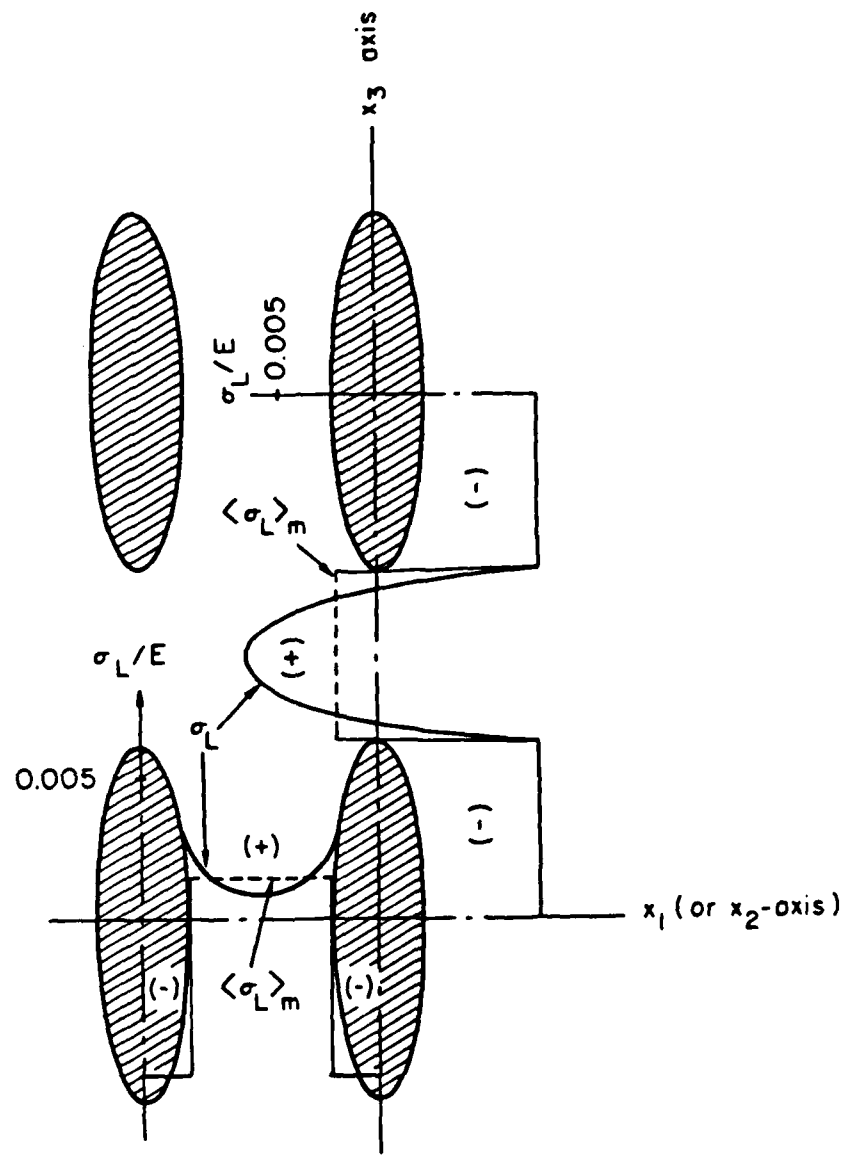


Figure 6 A schematic of the stress distribution in the matrix and in the reinforcement due to the difference in thermal coefficient of expansion between the silicon-carbide and aluminum.

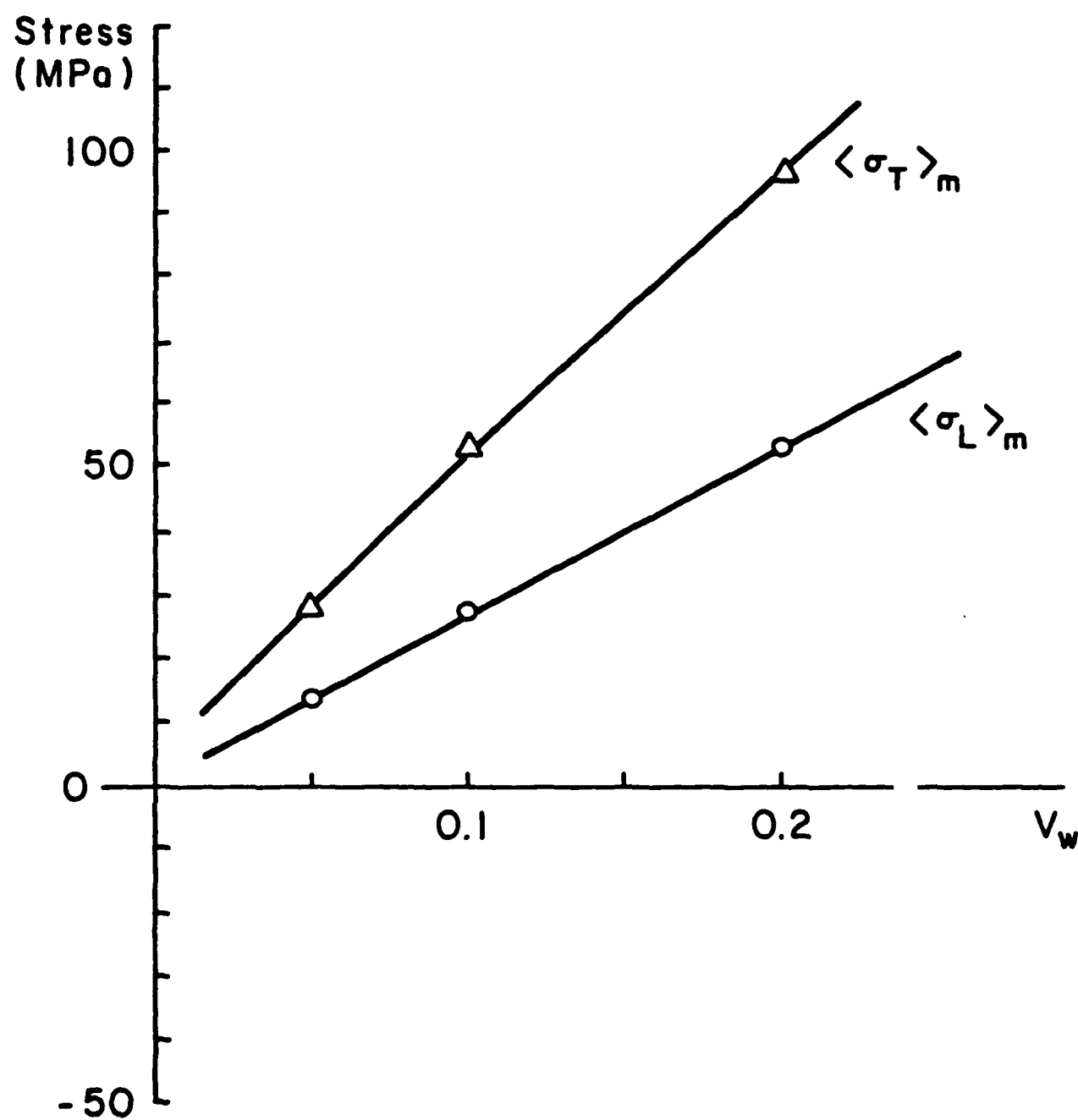


Figure 7 Predicted residual stress in the matrix for the transverse and longitudinal directions.

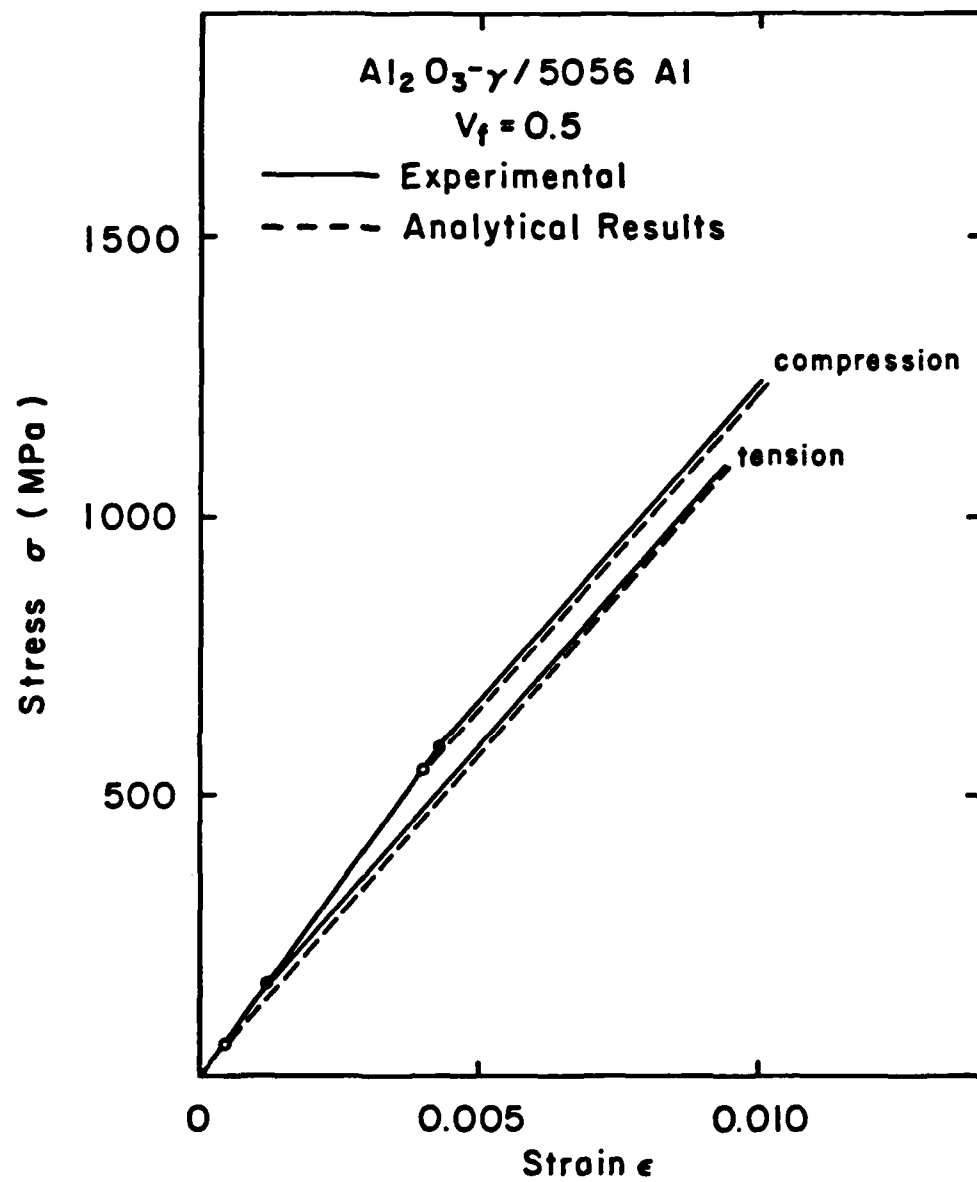


Figure 8 Tension and compression stress-strain curves of continuous Al<sub>2</sub>O<sub>3</sub>- $\gamma$  fiber/5056 Al composite with  $V_f = 0.5$ <sup>(26)</sup>. The experimental and theoretical results are denoted by solid dashed curves, respectively. The filled and open circles denote the yield stress of the experimental and theoretical results, respectively.

DTIC  
FILMED

4-86

END